Master's thesis

NTNU
Norwegian University of Science and Technology
Faculty of Engineering
Department of Mechanical and Industrial Engineering

Ingeborg Helen Langli

Flexure Patterns For the End User

Facilitating the understanding and use of flexure patterns

Master's thesis in Master of Science in Mechanical Engineering and ICT

Supervisor: Nils Petter Vedvik

June 2019

NTNU
Norwegian University of Science and Technology

Ingeborg Helen Langli

Flexure Patterns For the End User

Facilitating the understanding and use of flexure patterns

Master's thesis in Mechanical Engineering and ICT
Supervisor: Nils Petter Vedvik
June 2019

Norwegian University of Science and Technology
Faculty of Engineering
Department of Mechanical and Industrial Engineering

NTNU
Norwegian University of
Science and Technology

Abstract

Giving a plate new properties simply by cutting a pattern into it can have many uses which can be discovered by creative minds, professionals and laymen alike. To this end, flexure patterns must be made more accessible. This work contributes to this by performing experiments on patterned plates, recording deformation under different load cases, and comparing experimental results with simulated results. The visualization of these results contributes to better understanding of the theory behind flexure patterns. In addition, a web application is created to facilitate the creation of flexure patterns with user-defined parameters.

Sammendrag

Å gi en plate nye egenskaper kun ved å kutte et mønster inn i den kan ha mange bruksområder som kan oppdages av kreative sinn, både hos fagfolk og lekmenn. Til dette formålet må bøyningsmønstre gjøres mer tilgjengelige. Denne oppgaven bidrar til dette ved å utføre eksperimenter på mønstrede plater, måle deformasjon under forskjellige lasttilfeller, og sammenligne eksperimentelle resultater med simulerte resultater. Visualiseringen av disse resultatene bidrar til bedre forståelse av teorien bak bøyningsmønstre. I tillegg er det laget en webapplikasjon for å forenkle generering av bøyningsmønstre med brukerdefinerte parametere.

Table of Contents

Abstract i

Sammendrag ii

Table of Contents v

List of Tables vii

List of Figures xi

1 Introduction 1

2 Background 3
2.1 Flexure Patterns . . . 3
2.1.1 Patterns . . . 3
2.1.2 Flexure pattern creation . . . 7
2.1.3 Mechanical behavior . . . 7
2.1.4 Achieving target properties . . . 8
2.2 Mechanics . . . 8
2.2.1 Stress . . . 8
2.2.2 Strain . . . 9
2.2.3 Stress-strain relationship . . . 11
2.3 Plate theory . . . 14
2.3.1 Deflection and curvature . . . 14
2.3.2 Stresses and strains . . . 16
2.3.3 Forces and moments . . . 17
2.3.4 Large deflections of plates . . . 19
2.3.5 The stiffness matrix . . . 20
2.3.6 Coupling terms . . . 22
2.4 Regression analysis . . . 22
2.4.1 Linear regression . . . 22

2.4.2 Polynomial regression . . . 23
2.4.3 Local regression . . . 23
2.4.4 Interpolant analysis . . . 24
2.5 Materials . . . 24
2.5.1 Elastic and plastic deformation . . . 24
2.5.2 Heat-affected zone . . . 25
2.6 Laser cutting . . . 25
2.6.1 Advantages and disadvantages . . . 25
2.6.2 Hazards . . . 26

3 Method **27**
3.1 Web application . . . 27
3.1.1 Original code . . . 27
3.1.2 Adding functionality . . . 27
3.1.3 Creating a web application . . . 27
3.2 Simulation . . . 28
3.2.1 Part creation . . . 28
3.2.2 Finding the stiffness matrix . . . 28
3.2.3 Shell simulation . . . 29
3.2.4 Result gahering . . . 30
3.2.5 Visualization . . . 30
3.3 Experiment . . . 31
3.3.1 Equipment . . . 31
3.3.2 Specimens . . . 33
3.3.3 Specimen preparation . . . 36
3.3.4 Method . . . 41

4 Results and Discussion **43**
4.1 Material testing . . . 43
4.1.1 Discussion . . . 47
4.2 Measurements from experiments . . . 49
4.2.1 Interpolation of data . . . 49
4.2.2 Load case 1 . . . 49
4.2.3 Load case 2 . . . 49
4.2.4 Load case 3 . . . 51
4.2.5 Surface fitting . . . 51
4.2.6 Discussion . . . 51
4.3 Simulation . . . 53
4.3.1 Load case 1 . . . 53
4.3.2 Load case 2 . . . 53
4.3.3 Load case 3 . . . 53
4.3.4 The effect of NLGEOM . . . 53
4.3.5 Discussion . . . 56
4.4 Comparison of patterns . . . 56
4.4.1 Solid . . . 56
4.4.2 LET cmm . . . 59

4.4.3 LET p4m . . . 60
4.4.4 Coil cmm . . . 63
4.4.5 Coil p4 . . . 65
4.4.6 Switchback cmm . . . 68
4.4.7 Switchback p4g . . . 71
4.4.8 Discussion . . . 73
4.5 Impact of material properties . . . 73
4.5.1 Discussion . . . 75
4.6 Web application . . . 76
4.6.1 Front-end . . . 76
4.6.2 Back-end . . . 78
4.6.3 Discussion . . . 79

5 Conclusion **81**

Bibliography **83**

Appendix **85**
A Surface fitting . . . 85
A.1 Polynomial models . . . 85
A.2 Interpolant models . . . 86
A.3 Loess models . . . 88

List of Tables

2.1 Recognition chart for relevant plane periodic patterns. 4
2.2 Stiffness equations of a single flexure strip. 8
2.3 Form of bivariate polynomials. 23

3.1 Measurements for YdX cmm unit. 36

4.1 Properties of PETG sheets. 47
4.2 Difference in stiffness coefficients with different Poisson's ratio ν. 49
4.3 Matlab models for surface fitting. 51
4.4 Measurements for LET cmm unit. 59
4.5 Measurements for LET p4m unit. 60
4.6 Measurements for coil cmm unit. 63
4.7 Measurements for coil p4 unit. 65
4.8 Measurements for switchback cmm unit. 68
4.9 Measurements for switchback p4g unit. 71
4.10 Change in stiffness coefficient with change in Poisson's ratio. 74

List of Figures

2.1 The different parts of a flexure pattern. 5
2.2 Lattices for periodic plane patterns. For the rhombic lattice, the centered cell is represented by a dashed line. 5
2.3 Wallpaper groups with symmetry elements. 6
2.4 Normal and shear stress. 9
2.5 Normal and shear strain. 10
2.6 Deflection of a plate section. 14
2.7 Examples of shapes with different Gauss curvatures. 16
2.8 An element cut out of a plate. 16
2.9 An element cut out of a plate, with forces and moments on the middle plane. 18
2.10 Moments and shear forces on the middle plane of the plate. 18
2.11 In-plane forces acting in the middle plane of the plate. 19
2.12 Stress-strain diagram. 24

3.1 Abaqus screen showing node sets. 30
3.2 The laser cutter's dialog screen. 32
3.3 Test rig. 33
3.4 Constituent molecules of PET-G. 35
3.5 YdX cmm unit. 36
3.6 Pattern in black; suspension points in blue; middle load point in green; side load points in red. 37
3.7 Zoomed-in sample showing angled kerf. 38
3.8 Laser cutter tests. 39
3.9 Two plates fresh out of the laser cutter. 40
3.10 Plate before and after scraping off dross. 40
3.11 Load suspended from plate. 41
3.12 Load cases. 42

4.1 Tension test specimen dimensions (in mm). 43
4.2 Specimens after tension testing. 44

4.3 Stress-strain diagrams from tensile testing. 45
4.4 Lateral-axial strain diagrams from tensile testing. 46
4.5 Stiffness coefficients with variable Poisson's ratio ν. 48
4.6 Load case 1 on plate 1. 50
4.7 Load case 1 on plate 2. 50
4.8 Load case 2 on plate 1. 50
4.9 Load case 2 on plate 1. 50
4.10 Load case 1 on plate 1 fitted with the loess model. 52
4.11 Load case 1 on plate 2 fitted with the loess model. 52
4.12 Load case 2 on plate 1 fitted with the loess model. 52
4.13 Load case 3 on plate 2 fitted with the loess model. 52
4.14 Load case 1 simulated. 54
4.15 Load case 1 comparison between measured data points and simulation. . . 54
4.16 Load case 2 simulated. 54
4.17 Load case 2 comparison between measured data points and simulation. . . 54
4.18 Load case 3 simulated. 55
4.19 Load case 3 comparison between measured data points and simulation. . . 55
4.20 Comparison between simulations with and without NLGEOM. 55
4.21 Load case 1 on a solid plate. 57
4.22 Load case 1 comparison between a solid plate and a YdX cmm plate. . . . 57
4.23 Load case 2 on a solid plate. 58
4.24 Load case 2 comparison between a solid plate and a YdX cmm plate. . . . 58
4.25 Load case 3 on a solid plate. 58
4.26 Load case 3 comparison between a solid plate and a YdX cmm plate. . . . 59
4.27 LET cmm unit. 59
4.28 LET p4m unit. 60
4.29 Load case 1 on a LET p4m plate. 61
4.30 Load case 1 comparison between a LET p4m plate and a YdX cmm plate. 61
4.31 Load case 2 on a LET p4m plate. 61
4.32 Load case 2 comparison between a LET p4m plate and a YdX cmm plate. 62
4.33 Load case 3 on a LET p4m plate. 62
4.34 Load case 3 comparison between a LET p4m plate and a YdX cmm plate. 62
4.35 Coil cmm unit. 63
4.36 Load case 1 on a coil cmm plate. 63
4.37 Load case 1 comparison between a coil cmm plate and a YdX cmm plate. 64
4.38 Load case 2 on a coil cmm plate. 64
4.39 Load case 2 comparison between a coil cmm plate and a YdX cmm plate. 64
4.40 Load case 3 on a coil cmm plate. 65
4.41 Load case 3 comparison between a LET p4m plate and a YdX cmm plate. 65
4.42 Coil p4 unit. 65
4.43 Load case 1 on a coil p4 plate. 66
4.44 Load case 1 comparison between a coil p4 plate and a YdX cmm plate. . . 66
4.45 Load case 2 on a coil p4 plate. 67
4.46 Load case 2 comparison between a coil p4 plate and a YdX cmm plate. . . 67
4.47 Load case 3 on a coil p4 plate. 67

4.48 Load case 3 comparison between a coil p4 plate and a YdX cmm plate. . . 68
4.49 Switchback cmm unit. 68
4.50 Load case 1 on a switchback cmm plate. 69
4.51 Load case 1 comparison between a switchback cmm plate and a YdX cmm plate. 69
4.52 Load case 2 on a switchback cmm plate. 69
4.53 Load case 2 comparison between a switchback cmm plate and a YdX cmm plate. 70
4.54 Load case 3 on a switchback cmm plate. 70
4.55 Load case 3 comparison between a switchback cmm plate and a YdX cmm plate. 70
4.56 Switchback p4g unit. 71
4.57 Load case 1 on a switchback p4g plate. 71
4.58 Load case 1 comparison between a switchback p4g plate and a YdX cmm plate. 72
4.59 Load case 2 on a switchback p4g plate. 72
4.60 Load case 2 comparison between a switchback p4g plate and a YdX cmm plate. 72
4.61 Load case 3 on a switchback p4g plate. 73
4.62 Load case 3 comparison between a switchback p4g plate and a YdX cmm plate. 73
4.63 The pages of the web application. 77

A.1 Load case 3 on plate 2 fitted with the 2nd degree polynomial model. . . . 85
A.2 Load case 3 on plate 2 fitted with the 3rd degree polynomial model. . . . 85
A.3 Load case 3 on plate 2 fitted with the 4th degree polynomial model. . . . 86
A.4 Load case 3 on plate 2 fitted with the 5th degree polynomial model. . . . 86
A.5 Load case 3 on plate 2 fitted with the linear interpolation model. 86
A.6 Load case 3 on plate 2 fitted with the nearest neighbor interpolation model. 87
A.7 Load case 3 on plate 2 fitted with the cubic spline interpolation model. . . 87
A.8 Load case 3 on plate 2 fitted with the biharmonic interpolation model. . . 87
A.9 Load case 3 on plate 2 fitted with the thin-plate spline interpolation model. 88
A.10 Load case 3 on plate 2 fitted with the local linear regression model. 88
A.11 Load case 3 on plate 2 fitted with the local quadratic regression model. . . 88

Chapter 1

Introduction

The study of flexure patterns is a relatively new field, with the term having been coined as recently as 2017. Similar concepts already existed, such as living hinge and compliant array, but the flexure pattern term describes it in a broader sense. The definition, introduced by Oddvin Agnalt Østmo in his master's thesis on the subject[17], goes as follows:

> A flexure pattern is characterized as a 2D mechanical metamaterial that consists of flexures configured in a pattern that increases the compliance compared to the bulk material of which it has been made. The flexures are patterned onto the plane according to a set of rules.

A metamaterial is a material that is constructed to achieve properties that are not found naturally. It is made from multiple elements of certain shapes and sizes assembled in specific arrangements, which is what the material derives its properties from, rather than the properties of its base materials. A *mechanical* metamaterial is specified to distinguish it from other types, such as electromagnetic or optical metamaterials, the difference being what types of properties one desires to achieve. In a flexure pattern, the elements are flexures – flexible elements engineered to be compliant in specific degrees of freedom – and the desired property is increased compliance. To put it simply, a flexure pattern is a pattern cut into a plate to allow it to bend more easily than its material would normally allow.

Giving a plate new properties simply by cutting a pattern into it can have many uses which can be discovered by creative minds, professionals and laymen alike. To this end, flexure patterns must be made more accessible. This thesis attempts to do so by:

1. Creating a web application for flexure pattern generation.
2. Simulating the behavior of patterned plates.
3. Testing flexure pattern behavior in real life.

Chapter 1 introduces the topic. Chapter 2 contains background, discussing relevant theory for the topic. Chapter 3 contains methodology, describing the creation of the web

application and the tools used; the method of gathering results from simulations and the visualizations thereof; and the execution of the experiment. Chapter 4 presents the results and discussion thereof. Finally, chapter 5 concludes the thesis.

Chapter 2

Background

2.1 Flexure Patterns

2.1.1 Patterns

Although theoretically, the amount of patterns it is possible to create is limited only by the imagination, in order to reliably replicate properties introduced by flexure patterns it is necessary to define a set of definitions and rules.

Parts

A flexure pattern consists of the parts shown in figure 2.1.

Wallpaper groups

A wallpaper group, or plane symmetry group, is a classification of a two dimensional repetitive pattern based on its symmetries. The classification has its basis in crystallography. There are 17 distinct plane symmetry groups, see table 2.1. Much of the information in this section is derived from Schattschneider's article on the subject[16].

Each letter in the crystallographic name for the wallpaper group has a significance. The first symbol is either *p* for *primitive cell* or *c* for *centered cell*. The primitive cell is simply the lattice unit, as seen in figure 2.2 with solid lines[1]. The corners are at the centers of highest order of rotation. On the other hand, the centered cell, shown in figure 2.2c with dashed lines, has its sides normal to the reflection axes. The second symbol denotes the highest order of rotation. As you rotate the wallpaper group $360°$, this is the amount of times it will look exactly the same as its original, un-rotated version. The third symbol denotes a symmetry axis normal to the x-axis and is either an *m* for *mirror* or *reflection*; a *g* for *glide-reflection*; or a *1* for no symmetry. The fourth symbol denotes a symmetry axis at

[1] There are also two more lattices, parallelogram and hexagonal, that are not shown here.

an angle dependent on the highest order of rotation, with the symbol otherwise interpreted as the third symbol.

Type	Lattice	Highest order of rotation	Reflections	Non-trivial glide reflections	Generating region
p1	parallelogram	1	no	no	unit
p2	parallelogram	2	no	no	1/2 unit
pm	rectangular	1	yes	no	1/2 unit
pg	rectangular	1	no	yes	1/2 unit
cm	rhombic	1	yes	yes	1/2 unit
pmm	rectangular	2	yes	no	1/4 unit
pmg[2]	rectangular	2	yes	yes	1/4 unit
pgg	rectangular	2	no	yes	1/4 unit
cmm[3]	rhombic	2	yes	yes	1/4 unit
p4	square	4	no	no	1/4 unit
p4m[4]	square	4	yes	yes	1/8 unit
p4g[5]	square	4	yes	yes	1/8 unit
p3	hexagonal	3	no	no	1/3 unit
p3m1[6]	hexagonal	3	yes	yes	1/6 unit
p31m[7]	hexagonal	3	yes	yes	1/6 unit
p6	hexagonal	6	no	no	1/6 unit
p6m	hexagonal	6	yes	yes	1/12 unit

Table 2.1: Recognition chart for relevant plane periodic patterns.

Diagrams of the wallpaper groups can be found in figure 2.3. These do not necessarily correspond to the unit of the flexure pattern, but may be built up from generating regions of several adjacent units.

[2] Parallel reflection axes.
[3] Perpendicular reflection axes.
[4] 4-fold centers on reflection axes.
[5] 4-fold centers not on reflection axes.
[6] All 3-fold centers on reflection axes.
[7] Not all 3-fold centers on reflection axes.

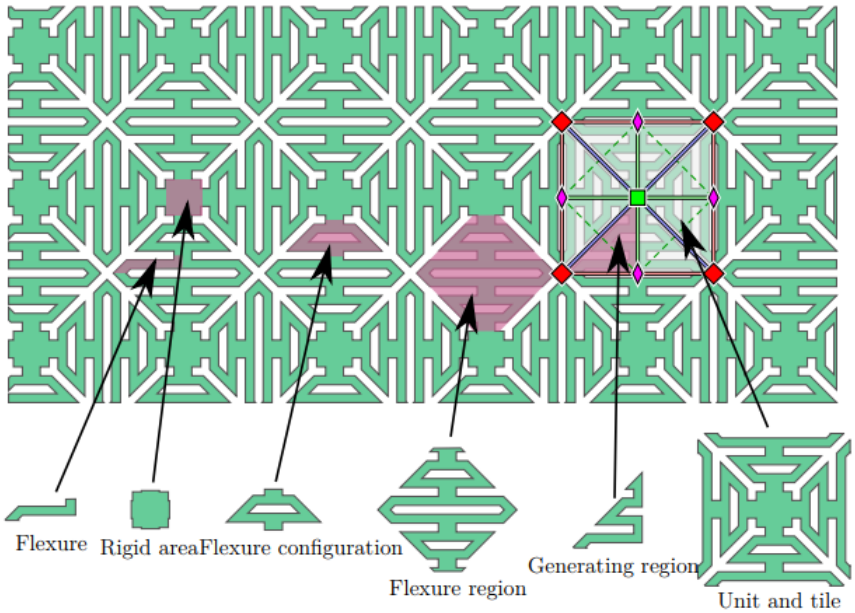

Figure 2.1: The different parts of a flexure pattern, here shown on a LET p4m pattern. Figure adapted from Østmo[17].

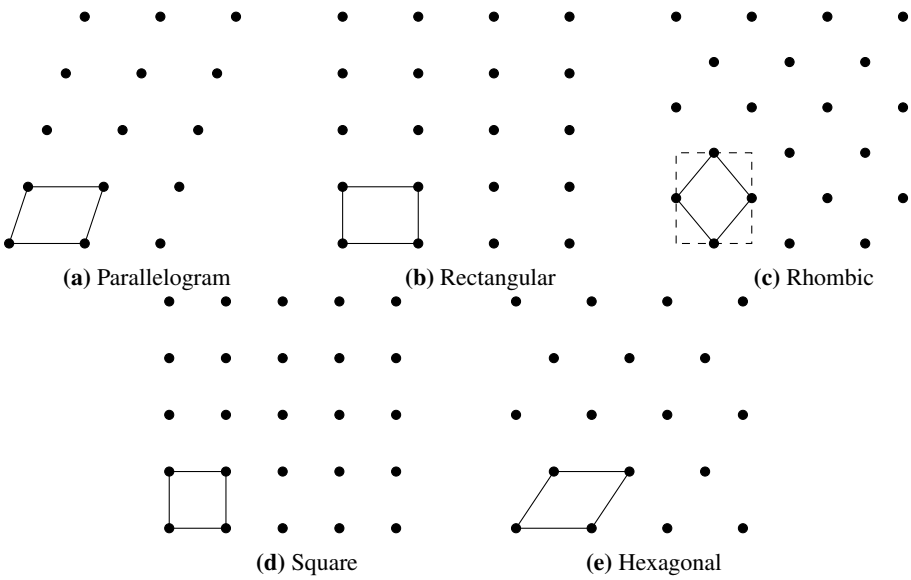

Figure 2.2: Lattices for periodic plane patterns. For the rhombic lattice, the centered cell is represented by a dashed line.

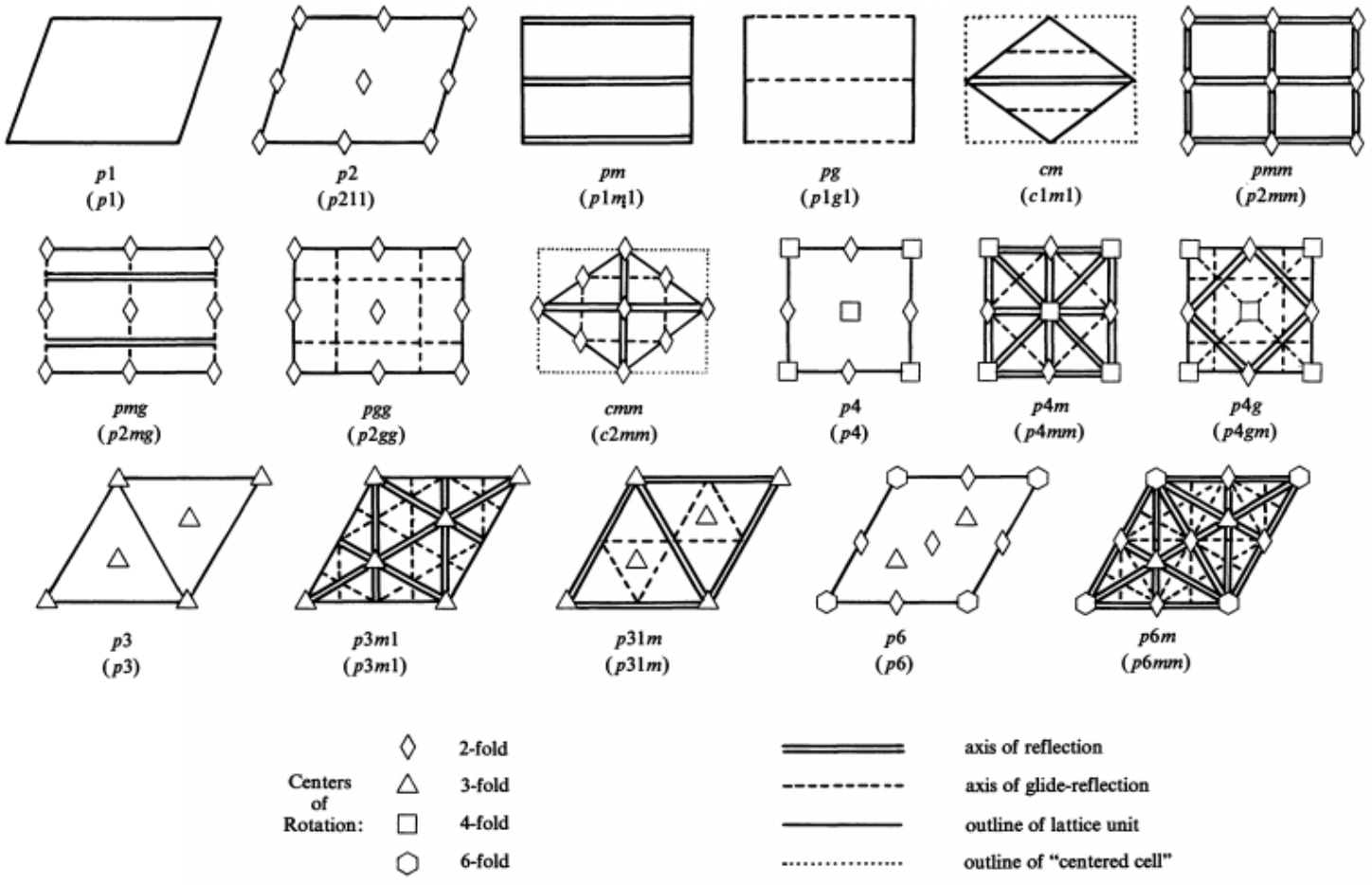

Figure 2.3: Wallpaper groups with symmetry elements. Adapted from Schattschneider[16].

2.1.2 Flexure pattern creation

In his master's thesis, Østmo proposed the following basic method for creating new flexure patterns[17]:

1. Choose a flexure mechanism.
2. Choose a basic tile.
    - Use triangles to build polygons.
3. Choose a tiling.
    - The crystallographic wallpaper groups are a good basis for tiling.

In addition, one must take care to make the pattern continuous (no gaps or overlaps), connected (symmetrical connection points, or asymmetrical connection points with mirrored tiles) and compliant (flexible members, no inactive flexures or interlocking regions).

2.1.3 Mechanical behavior

The behavior of a flexure pattern depends on the flexure type and the wallpaper group, as well as the parameters describing geometry.

Single flexure strips

A single flexure strip is a basic building block. Although its compliant degrees of freedom (DOFs) are controlled by the complete flexure configuration, a single flexure is generally regarded as compliant in three DOFs (translative, bending and twist). It is often modelled as a spring.

The equations for the stiffnesses in different modes are given in table 2.2, where:

- E = Young's modulus
- G = Modulus of rigidity
- A = Cross section area
- I = Moment of inertia
- J = Polar moment of inertia
- L = Length of the flexure strip
- w = Width of the cross section
- t = Thickness (height) of the cross section
- c = Factor for bending mode given by boundary conditions

Regarding geometry, increasing the length of the flexure strip increases the compliance in bending and torsion. Increasing the height-to-width ratio of the cross-section increases the resistance to bending and torsion, having a greater effect on the former than the latter.

	Axial	Angular
Tension	$K_t^u = EA$	
Bending	$K_B^u = \frac{cEI}{L^3}$	$K_B^\Theta = \frac{cEI}{L}$
Torsion		$K_T^\Theta = \frac{JG}{L}$

Table 2.2: Stiffness equations of a single flexure strip.

Compound flexures

Flexure strips can be combined in series, increasing compliance, total deflection and angular deflection, and stored energy; or in parallel, decreasing compliance and increasing total force and stored energy. The compound flexures can be symmetric, antisymmetric or asymmetric. Symmetric structures are more stable as the response in the structure cancels out some forces internally, whereas the responses antisymmetric and asymmetric structures may trigger additional moments, creating higher stresses.

2.1.4 Achieving target properties

Certain design choices have been discovered to achieve target properties:

- To increase compliance, reduce flexure width and increase flexure length while reducing plate thickness.
- To increase out-of-plane compliance while keeping in-plane stiffness, proportionally scale the geometry while keeping the same plate thickness.
- P4 patterns with only rotations present will give different in-plane and out-of-plane axes of rotation.
- Patterns with at least one axis of reflection or glide reflection give orthogonal stiffness.
- Patterns with 3-fold symmetry or more give transverse isotropic stiffness.
- Flexure configurations with many degrees of freedom give a low degree of anisotropy, and vice versa.

2.2 Mechanics

The main sources of information in this section are Bell[5], Dowling[8] and Hibbeler[12].

2.2.1 Stress

Normal stress is the intensity of the force acting normal to an area, while shear stress is the intensity of the force acting tangent to an area. Figure 2.4 shows the stresses on faces

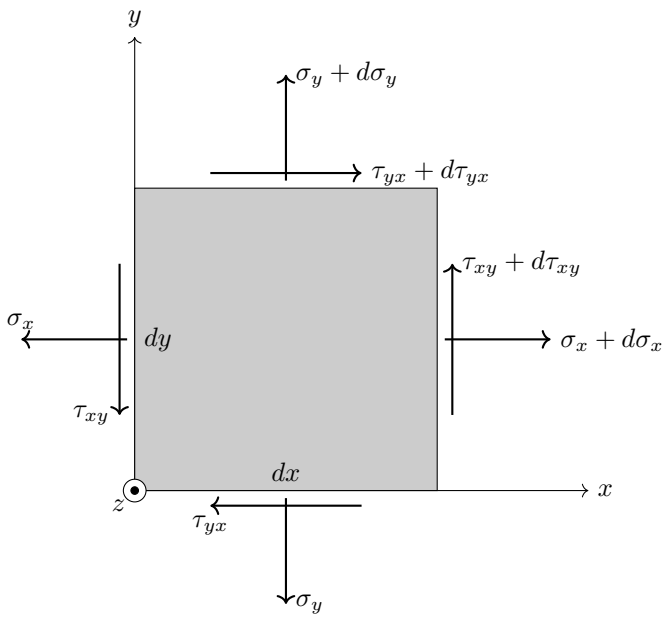

Figure 2.4: Normal and shear stress.

parallel to the $x - y$ plane, with σ_x and σ_y being normal stresses and τ_{xy} and τ_{yx} being shear stresses. The stress matrix is:

$$\boldsymbol{\sigma}_M = \begin{bmatrix} \sigma_x & \tau_{xy} & \tau_{xz} \\ \tau_{yx} & \sigma_y & \tau_{yz} \\ \tau_{zx} & \tau_{zy} & \sigma_z \end{bmatrix} \tag{2.1}$$

The complementary property of shear means that, due to moment equilibrium:

$$\tau_{xy} = \tau_{yx}, \tau_{yz} = \tau_{zy}, \tau_{zx} = \tau_{xz} \tag{2.2}$$

This means that the stress matrix is symmetric. It is then more convenient to express a stress *vector*:

$$\boldsymbol{\sigma} = \begin{bmatrix} \sigma_x \\ \sigma_y \\ \sigma_z \\ \tau_{xy} \\ \tau_{yz} \\ \tau_{zx} \end{bmatrix} \tag{2.3}$$

2.2.2 Strain

Figure 2.5 shows two lines OA and OB on an undeformed body in cyan, parallel to the x and y axes respectively and perpendicular to one another. After deformation, the points

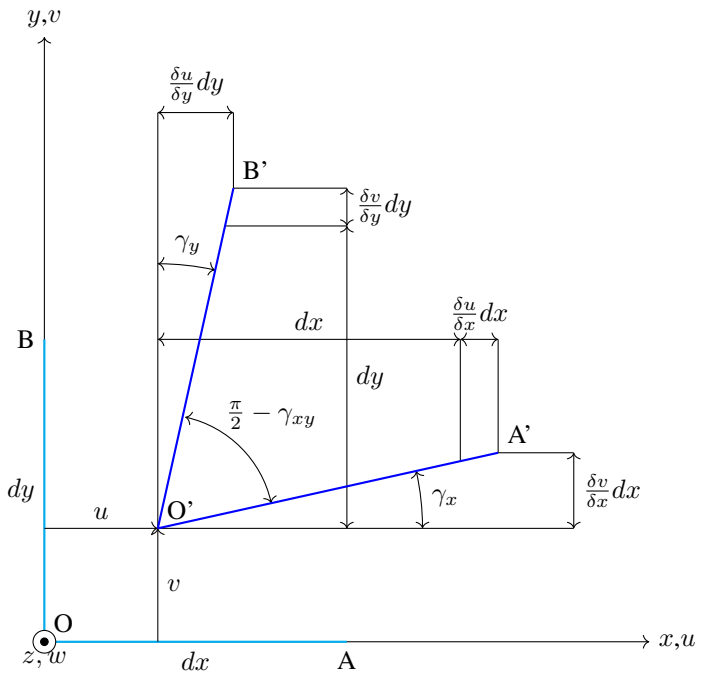

Figure 2.5: Normal and shear strain.

O, A and B have shifted to O', A' and 'B respectively, forming the lines (OA)' and (OB)' shown in blue.

Normal strain is the change in length of a line segment per unit length[12]. For line OA, the change in length is:

$$du = \frac{\delta u}{\delta x}dx$$

Since OA is along the x axis, dy and dz are both zero. The normal strain in the x direction at point O is then:

$$\epsilon_x = \frac{|\text{O} - \text{A}|}{|\text{O'} - \text{A'}|} = \frac{\delta u}{\delta x} \tag{2.4}$$

Similarly, for the y and z directions respectively:

$$\epsilon_y = \frac{\delta v}{\delta y} \tag{2.5}$$

$$\epsilon_z = \frac{\delta w}{\delta z} \tag{2.6}$$

Shear strain is the change in angle, measured in radians, between two line segments that are originally perpendicular to one another[12]. For small displacements:

$$\tan \gamma_x = \frac{\frac{\delta v}{\delta x} dx}{dx} = \frac{\delta v}{\delta x} \approx \gamma_x$$

and similarly for γ_y. The change in angle, and thus the shear strain, in the $x - y$ plane is then:

$$\gamma_{xy} = \gamma_y + \gamma_x = \frac{\delta u}{\delta y} + \frac{\delta v}{\delta x} \tag{2.7}$$

Similarly, for the $y - z$ and $z - x$ planes respectively:

$$\gamma_{yz} = \frac{\delta v}{\delta z} + \frac{\delta w}{\delta y} \tag{2.8}$$

$$\gamma_{zx} = \frac{\delta u}{\delta z} + \frac{\delta w}{\delta x} \tag{2.9}$$

Putting it all together, we can then express deformation in matrix notation:

$$\begin{bmatrix} \epsilon_x \\ \epsilon_y \\ \epsilon_z \\ \gamma_{xy} \\ \gamma_{yz} \\ \gamma_{zx} \end{bmatrix} = \begin{bmatrix} \frac{\delta}{\delta x} & 0 & 0 \\ 0 & \frac{\delta}{\delta y} & 0 \\ 0 & 0 & \frac{\delta}{\delta z} \\ \frac{\delta}{\delta y} & \frac{\delta}{\delta x} & 0 \\ 0 & \frac{\delta}{\delta z} & \frac{\delta}{\delta y} \\ \frac{\delta}{\delta z} & 0 & \frac{\delta}{\delta x} \end{bmatrix} \begin{bmatrix} u \\ v \\ w \end{bmatrix} \tag{2.10}$$

This is equivalent to:

$$\boldsymbol{\epsilon} = \boldsymbol{\Delta} \mathbf{u} \tag{2.11}$$

where $\boldsymbol{\epsilon}$ is the strain vector, $\boldsymbol{\Delta}$ is the operator matrix, and $\mathbf{u}$ is the displacement vector.

2.2.3 Stress-strain relationship

Imagine a two dimensional specimen in the $x - y$ plane being stretched in the x direction.

Hooke's law states that the strain on a body is proportional to the stress applied to it. In the x direction it is expressed by:

$$\epsilon_x = \frac{\sigma_x}{E_x} \tag{2.12}$$

where E_x is the modulus of elasticity or Young's modulus.

As the specimen stretches in the x or axial direction, it contracts in the y o lateral direction. This is known as the Poisson effect, and the ratio between the lateral and axial strain is called Poisson's ratio:

$$\nu_y = -\frac{\epsilon_y}{\epsilon_x} \tag{2.13}$$

Meaning that:

$$\epsilon_y = -\nu_y \epsilon_x = -\nu_y \frac{\sigma_x}{E_x} \tag{2.14}$$

Isotropic materials

An isotropic material is a material in which elastic properties are independent of direction. If a material is isotropic, then:

$$\nu_x = \nu_y = \nu_z = \nu \text{ and } E_x = E_y = E_z = E \tag{2.15}$$

We can use this to get the following expressions for normal strain:

$$\begin{aligned} \epsilon_x &= \frac{1}{E}(\sigma_x - \nu\sigma_y - \nu\sigma_z) \\ \epsilon_y &= \frac{1}{E}(-\nu\sigma_x + \sigma_y - \nu\sigma_z) \\ \epsilon_z &= \frac{1}{E}(-\nu\sigma_x - \nu\sigma_y + \sigma_z) \end{aligned} \tag{2.16}$$

and for shear strain:

$$\begin{aligned} \gamma_{xy} &= \frac{2(1+\nu)}{E}\tau_{xy} = \frac{1}{G}\tau_{xy} \\ \gamma_{yz} &= \frac{2(1+\nu)}{E}\tau_{yz} = \frac{1}{G}\tau_{yz} \\ \gamma_{zx} &= \frac{2(1+\nu)}{E}\tau_{zx} = \frac{1}{G}\tau_{xy} \end{aligned} \tag{2.17}$$

where:

$$G = \frac{E}{2(1+\nu)} \tag{2.18}$$

is the shear modulus. In matrix notation:

$$\begin{bmatrix} \epsilon_x \\ \epsilon_y \\ \epsilon_z \\ \gamma_{xy} \\ \gamma_{yz} \\ \gamma_{zx} \end{bmatrix} = \frac{1}{E} \begin{bmatrix} 1 & -\nu & -\nu & 0 & 0 & 0 \\ -\nu & 1 & -\nu & 0 & 0 & 0 \\ -\nu & -\nu & 1 & 0 & 0 & 0 \\ 0 & 0 & 0 & 2(1+\nu) & 0 & 0 \\ 0 & 0 & 0 & 0 & 2(1+\nu) & 0 \\ 0 & 0 & 0 & 0 & 0 & 2(1+\nu) \end{bmatrix} \begin{bmatrix} \sigma_x \\ \sigma_y \\ \sigma_z \\ \tau_{xy} \\ \tau_{yz} \\ \tau_{zx} \end{bmatrix} \tag{2.19}$$

which is equivalent to:

$$\boldsymbol{\epsilon} = \mathbf{C}^{-1}\boldsymbol{\sigma} \tag{2.20}$$

where $\mathbf{C}^{-1}$ is the compliance or flexibility matrix. Inversely:

$$\begin{bmatrix} \sigma_x \\ \sigma_y \\ \sigma_z \\ \tau_{xy} \\ \tau_{yz} \\ \tau_{zx} \end{bmatrix} = \begin{bmatrix} \lambda+2G & \lambda & \lambda & 0 & 0 & 0 \\ \lambda & \lambda+2G & \lambda & 0 & 0 & 0 \\ \lambda & \lambda & \lambda+2G & 0 & 0 & 0 \\ 0 & 0 & 0 & G & 0 & 0 \\ 0 & 0 & 0 & 0 & G & 0 \\ 0 & 0 & 0 & 0 & 0 & G \end{bmatrix} \begin{bmatrix} \epsilon_x \\ \epsilon_y \\ \epsilon_z \\ \gamma_{xy} \\ \gamma_{yz} \\ \gamma_{zx} \end{bmatrix} \tag{2.21}$$

which is equivalent to:

$$\boldsymbol{\sigma} = \mathbf{C}\boldsymbol{\epsilon} \tag{2.22}$$

where $\mathbf{C}$ is the elasticity matrix and:

$$\lambda = \frac{\nu E}{(1+\nu)(1-2\nu)} \tag{2.23}$$

is Lamé's constant.

Anisotropic materials

If the material is anisotropic:

$$\mathbf{C} = \begin{bmatrix} C_{11} & C_{12} & C_{13} & C_{14} & C_{15} & C_{16} \\ C_{21} & C_{22} & C_{23} & C_{24} & C_{25} & C_{26} \\ C_{31} & C_{32} & C_{33} & C_{34} & C_{35} & C_{36} \\ C_{41} & C_{42} & C_{43} & C_{44} & C_{45} & C_{46} \\ C_{51} & C_{52} & C_{53} & C_{54} & C_{55} & C_{56} \\ C_{61} & C_{62} & C_{63} & C_{64} & C_{65} & C_{66} \end{bmatrix} \tag{2.24}$$

The matrix is symmetrical, so $C_{ij} = C_{ji}$, giving 21 independent constants. Likewise:

$$\mathbf{C}^{-1} = \mathbf{S} = \begin{bmatrix} S_{11} & S_{12} & S_{13} & S_{14} & S_{15} & S_{16} \\ S_{21} & S_{22} & S_{23} & S_{24} & S_{25} & S_{26} \\ S_{31} & S_{32} & S_{33} & S_{34} & S_{35} & S_{36} \\ S_{41} & S_{42} & S_{43} & S_{44} & S_{45} & S_{46} \\ S_{51} & S_{52} & S_{53} & S_{54} & S_{55} & S_{56} \\ S_{61} & S_{62} & S_{63} & S_{64} & S_{65} & S_{66} \end{bmatrix} \tag{2.25}$$

Orthotropic materials

If the material is orthotropic, i.e. has three orthotropic planes of symmetry:

$$\mathbf{C} = \begin{bmatrix} C_{11} & C_{12} & C_{13} & 0 & 0 & 0 \\ C_{21} & C_{22} & C_{23} & 0 & 0 & 0 \\ C_{31} & C_{32} & C_{33} & 0 & 0 & 0 \\ 0 & 0 & 0 & C_{44} & 0 & 0 \\ 0 & 0 & 0 & 0 & C_{55} & 0 \\ 0 & 0 & 0 & 0 & 0 & C_{66} \end{bmatrix} \tag{2.26}$$

$$\mathbf{C}^{-1} = \mathbf{S} = \begin{bmatrix} \frac{1}{E_x} & -\frac{\nu_{yx}}{E_y} & -\frac{\nu_{zz}}{E_z} & 0 & 0 & 0 \\ -\frac{\nu_{xy}}{E_x} & \frac{1}{E_y} & -\frac{\nu_{zt}}{E_z} & 0 & 0 & 0 \\ -\frac{\nu_{xz}}{E_x} & -\frac{\nu_{yz}}{E_y} & \frac{1}{E_z} & 0 & 0 & 0 \\ 0 & 0 & 0 & \frac{1}{G_{yz}} & 0 & 0 \\ 0 & 0 & 0 & 0 & \frac{1}{G_{zx}} & 0 \\ 0 & 0 & 0 & 0 & 0 & \frac{1}{G_{xy}} \end{bmatrix} \tag{2.27}$$

2.3 Plate theory

The main sources of information in this section are Bell[5] and Timoshenko and Woinowsky-Krieger[18].

In Kirchhoff-Love plate theory, the following assumptions apply to thin plates affected by lateral loads with small deflections compared to their thickness:

1. There is no deformation in the middle plane of the plate.
2. Straight lines normal to the middle plane of the plate remain straight and normal to the middle plane of the plate after deformation.
3. Normal stresses in the direction transverse to the plate can be disregarded.

2.3.1 Deflection and curvature

Taking the middle plane of the unbent plate as the xy plane, during bending, the points in the xy plane undergo small displacements w perpendicular to said plane.

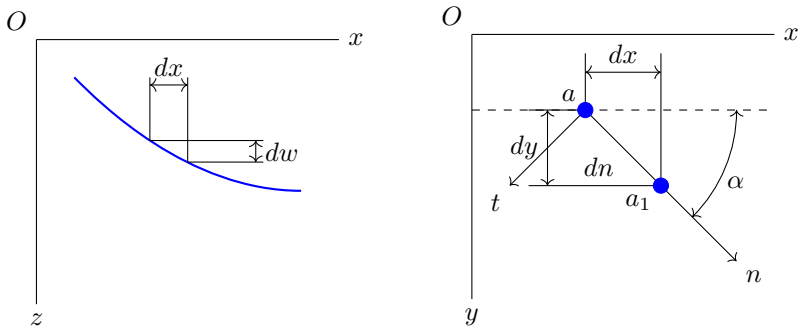

(a) Deflection in the zx plane. **(b)** Deflection in the xy plane.

Figure 2.6: Deflection of a plate section.

Figure 2.6 shows a bent plate in the zx plane and the xy plane. In figure 2.6a, the slope of the middle surface in the x direction is:

$$i_x = \frac{\delta w}{\delta x} \tag{2.28}$$

and likewise, in the y direction:

$$i_y = \frac{\delta w}{\delta y} \tag{2.29}$$

Figure 2.6b shows that, for any direction an in the xy plane at an angle α with the x axis, the difference in the deflections between point a and point a_1 on the an axis is:

$$dw = \frac{\delta w}{\delta x}dx + \frac{\delta w}{\delta y}dy \tag{2.30}$$

The corresponding slope is then:

$$\frac{\delta w}{\delta n} = \frac{\delta w}{\delta x}\cos\alpha + \frac{\delta w}{\delta y}\sin\alpha \tag{2.31}$$

Assuming the deflections are very small, the slope of the surface can be taken to be equal to the angle between the xy plane and the tangent of said surface. The curvature of the surface is then:

$$\kappa_x = \frac{1}{r_x} = -\frac{\delta}{\delta x}\left(\frac{\delta w}{\delta x}\right) = -\frac{\delta^2 w}{\delta x^2} \tag{2.32}$$

$$\kappa_y = \frac{1}{r_y} = -\frac{\delta}{\delta y}\left(\frac{\delta w}{\delta y}\right) = -\frac{\delta^2 w}{\delta y^2} \tag{2.33}$$

in a plane parallel to the zx plane and a plane parallel to the yz plane, respectively. A positive curvature is convex downward, while a negative curvature is convex upward. The curvature of the middle surface in any direction n is:

$$\kappa_n = \frac{1}{r_n} = -\frac{\delta}{\delta n}\left(\frac{\delta w}{\delta n}\right) \tag{2.34}$$

which becomes:

$$\kappa_n = \kappa_x \cos^2\alpha - \kappa_{xy}\sin 2\alpha + \kappa_y \sin^2\alpha \tag{2.35}$$

where:

$$\kappa_{xy} = \frac{1}{r_{xy}} = \frac{\delta^2 w}{\delta x \delta y} \tag{2.36}$$

is the twist of the surface with respect to the x and y axes. Likewise:

$$\kappa_t = \kappa_x \sin^2\alpha - \kappa_{xy}\sin 2\alpha + \kappa_y \cos^2\alpha \tag{2.37}$$

and:

$$\kappa_{nt} = \frac{d}{dt}\left(\frac{dw}{dn}\right) = \frac{1}{2}\left(\kappa_x - \kappa_y\right)\sin 2\alpha + \kappa_{xy}\cos 2\alpha \tag{2.38}$$

For simplification, one can assume that the zx and yz planes are taken parallel to the principal planes of curvature at point a – i.e. the planes of maximum and minimum curvature – which means that $\kappa_{xy} = 0$.

Gaussian curvature

The Gaussian curvature at a point is:

$$K = \kappa_x \kappa_y \tag{2.39}$$

Figure 2.7 shows shapes with negative, zero and positive Gauss curvatures. A negative Gauss curvature means that the curvature in each direction has opposite signs, and gives a saddle-like shape. A Gauss curvature of zero means that the curvature in at least one of the directions is zero, and gives a cylindrical shape – or, if the curvature in both directions is zero, a flat plane. A positive Gauss curvature means that the curvature in each direction has the same sign, and gives a dome-like shape.

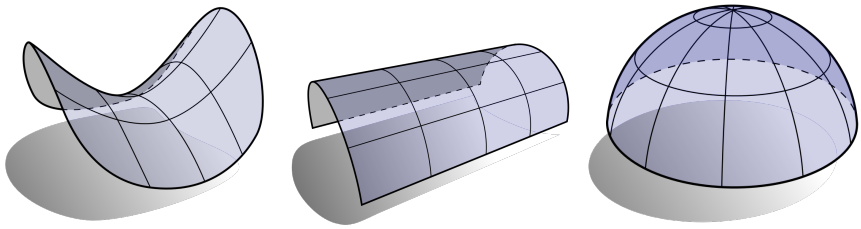

(a) $K < 0$ **(b)** $K = 0$ **(c)** $K > 0$

Figure 2.7: Examples of shapes with different Gauss curvatures. Images

2.3.2 Stresses and strains

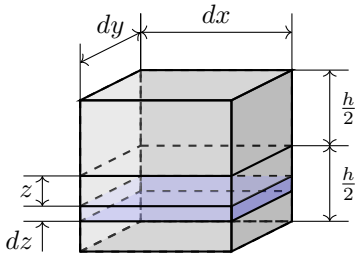

(a) The element

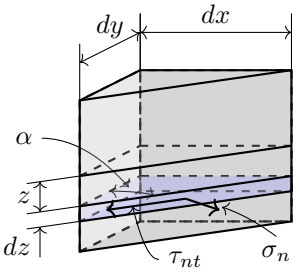

(b) Stresses acting on a section of the element inclined to the x and y axes.

Figure 2.8: An element cut out of a plate.

Figure 2.8a shows an element cut out of a plate. The strain at a distance z from the middle plane is:

$$\epsilon_x = \frac{\delta u}{\delta x} = \frac{\delta u^0}{\delta x} - z\frac{\delta^2 w}{\delta x^2} = \epsilon_x^0 + z\kappa_x \tag{2.40}$$

$$\epsilon_y = \frac{\delta v}{\delta y} = \frac{\delta v^0}{\delta y} - z\frac{\delta^2 w}{\delta y^2} = \epsilon_y^0 + z\kappa_y \tag{2.41}$$

$$\gamma_{xy} = \left(\frac{\delta u}{\delta y} + \frac{\delta v}{\delta x}\right) = \frac{\delta u^0}{\delta y} + \frac{\delta v^0}{\delta x} - 2z\frac{\delta^2 w}{\delta x \delta y} = \gamma_{xy}^0 + z\kappa_{xy} \tag{2.42}$$

or, in matrix form:

$$\begin{bmatrix} \epsilon_x \\ \epsilon_y \\ \gamma_{xy} \end{bmatrix} = \begin{bmatrix} \epsilon_x^0 \\ \epsilon_y^0 \\ \gamma_{xy}^0 \end{bmatrix} - z \begin{bmatrix} \frac{\delta^2 w}{\delta x^2} \\ \frac{\delta^2 w}{\delta y^2} \\ 2\frac{\delta^2 w}{\delta x \delta y} \end{bmatrix} = \begin{bmatrix} \epsilon_x^0 \\ \epsilon_y^0 \\ \gamma_{xy}^0 \end{bmatrix} + z \begin{bmatrix} \kappa_x \\ \kappa_y \\ \kappa_{xy} \end{bmatrix} \tag{2.43}$$

or simply:

$$\boldsymbol{\epsilon} = \boldsymbol{\epsilon^0} + z\boldsymbol{\kappa} \tag{2.44}$$

The stress is:

$$\begin{bmatrix} \sigma_x \\ \sigma_y \\ \tau_{xy} \end{bmatrix} = \begin{bmatrix} Q_{11} & Q_{12} & Q_{13} \\ Q_{21} & Q_{22} & Q_{23} \\ Q_{31} & Q_{32} & Q_{66} \end{bmatrix} \begin{bmatrix} \epsilon_x \\ \epsilon_y \\ \gamma_{xy} \end{bmatrix} \tag{2.45}$$

or simply:

$$\boldsymbol{\sigma} = \mathbf{Q}\boldsymbol{\epsilon} = \mathbf{Q}\boldsymbol{\epsilon^0} + \mathbf{Q}z\boldsymbol{\kappa} \tag{2.46}$$

where $\mathbf{Q}$ is the reduced stiffness matrix.
Figure 2.8b shows the stresses acting on the element in the nt plane, where:

$$\sigma_n = \sigma_x \cos^2\alpha + \sigma_y \sin^2\alpha \tag{2.47}$$

$$\tau_{nt} = \frac{1}{2}(\sigma_y - \sigma_x)\sin 2\alpha \tag{2.48}$$

where α is the angle between the n and x axes or, equivalently, the t and y axes.

2.3.3 Forces and moments

Figure 2.9 shows an element cut out of a plate, with the x and y axes on the middle plane of the plate and the z axis perpendicular to that plane. Any strain in the middle plane of the plate is assumed to be negligible. Shear forces are shown in yellow, bending moments in cyan and twisting moments in magenta.

Figure 2.10 shows the middle plane of the element and the forces and moments acting on it.

The equation of equilibrium for the forces is then:

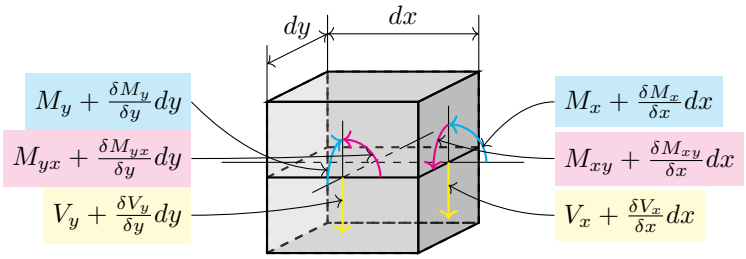

Figure 2.9: An element cut out of a plate, with forces and moments on the middle plane.

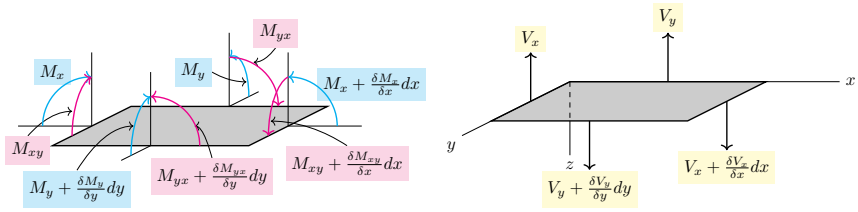

(a) Moments. **(b)** Shear forces.

Figure 2.10: Moments and shear forces on the middle plane of the plate.

$$\frac{\delta V_x}{\delta x} dxdy + \frac{\delta V_y}{\delta y} dydx + qdxdy = 0 \tag{2.49}$$

$$\frac{\delta V_x}{\delta x} + \frac{\delta V_y}{\delta y} + q = 0 \tag{2.50}$$

where q is the load distributed over the surface of the plate, which may include its weight. The equation of equilibrium for the moments with respect to the x axis:

$$\frac{\delta M_{xy}}{\delta x} dxdy + \frac{\delta M_y}{\delta y} dydx + V_y dxdy = 0 \tag{2.51}$$

$$\frac{\delta M_{xy}}{\delta x} + \frac{\delta M_y}{\delta y} + V_y = 0 \tag{2.52}$$

Likewise, about the y axis:

$$\frac{\delta M_{yx}}{\delta y} dydx + \frac{\delta M_x}{\delta x} dxdy + V_x dxdy = 0 \tag{2.53}$$

$$\frac{\delta M_{yx}}{\delta y} + \frac{\delta M_x}{\delta x} + V_x = 0 \tag{2.54}$$

Because $\tau_{xy} = \tau_{yx}$, we also have that $M_{yx} = -M_{xy}$. Using the above equations, the equation of equilibrium is:

$$\frac{\delta^2 M_x}{\delta x^2} - 2\frac{\delta^2 M_{xy}}{\delta x \delta y} + \frac{\delta^2 M_y}{\delta y^2} = -q \tag{2.55}$$

2.3.4 Large deflections of plates

Earlier in this section, the deflection of the plate has been assumed to be small compared to its thickness, which meant that strain in the middle plane of the plate could be neglected. However, with large deflections, one must take into account the in-plane forces brought on by strain due to bending, see figure 2.11.

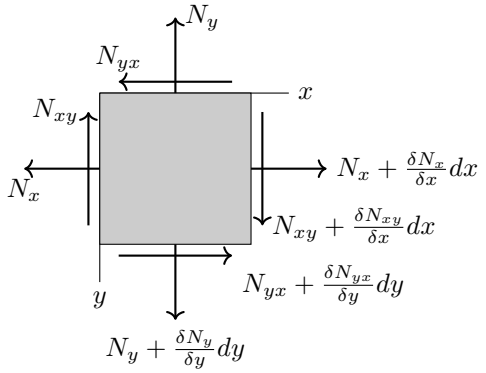

Figure 2.11: In-plane forces acting in the middle plane of the plate.

Assuming that there are no other in-place forces acting upon the plate, the following equations of equilibrium apply:

$$\begin{aligned} \frac{\delta N_x}{\delta x} + \frac{\delta N_{yx}}{\delta y} &= 0 \\ \frac{\delta N_y}{\delta y} + \frac{\delta N_{xy}}{\delta x} &= 0 \end{aligned} \tag{2.56}$$

where $N_{xy} = N_{yx}$. The corresponding strain components are:

$$\begin{aligned} \epsilon'_x &= \frac{\delta u}{\delta x} + \frac{1}{2}\left(\frac{\delta w}{\delta x}\right)^2 \\ \epsilon'_y &= \frac{\delta v}{\delta y} + \frac{1}{2}\left(\frac{\delta w}{\delta y}\right)^2 \\ \gamma'_{xy} &= \frac{\delta u}{\delta y} + \frac{\delta v}{\delta x} + \frac{\delta w}{\delta x}\frac{\delta w}{\delta y} \end{aligned} \tag{2.57}$$

2.3.5 The stiffness matrix

It can be shown that:

$$\mathbf{N} = \begin{bmatrix} N_x \\ N_y \\ N_{xy} \end{bmatrix} = \int_{-h/2}^{h/2} \boldsymbol{\sigma} dz \tag{2.58}$$

which becomes:

$$\mathbf{N} = \mathbf{A}\boldsymbol{\epsilon}^{\mathbf{0}} + \mathbf{B}\boldsymbol{\kappa} \tag{2.59}$$

where:

$$\mathbf{A} = \mathbf{Q}(z_{h/2} - z_{-h/2}) \tag{2.60}$$

$$\mathbf{B} = \frac{1}{2}\mathbf{Q}(z_{h/2}^2 - z_{-h/2}^2) \tag{2.61}$$

are the in-plane stiffness matrix and the bending-stretching coupling matrix, respectively. Likewise:

$$\mathbf{M} = \begin{bmatrix} M_x \\ M_y \\ M_{xy} \end{bmatrix} = \int_{-h/2}^{h/2} \boldsymbol{\sigma} z dz \tag{2.62}$$

which becomes:

$$\mathbf{M} = \mathbf{B}\boldsymbol{\epsilon}^{\mathbf{0}} + \mathbf{D}\boldsymbol{\kappa} \tag{2.63}$$

where:

$$\mathbf{D} = \frac{1}{3}\mathbf{Q}(z_{h/2}^3 - z_{-h/2}^3) \tag{2.64}$$

is the bending stiffness matrix. Combining these equations:

$$\begin{bmatrix} \mathbf{N} \\ \mathbf{M} \end{bmatrix} = \begin{bmatrix} \mathbf{A} & \mathbf{B} \\ \mathbf{B} & \mathbf{D} \end{bmatrix} \begin{bmatrix} \boldsymbol{\epsilon}^{\mathbf{0}} \\ \boldsymbol{\kappa} \end{bmatrix} \tag{2.65}$$

In its expanded form:

$$\begin{bmatrix} N_x \\ N_y \\ N_{xy} \\ M_x \\ M_y \\ M_{xy} \end{bmatrix} = \begin{bmatrix} A_{xx} & A_{xy} & A_{xs} & B_{xx} & B_{xy} & B_{xs} \\ A_{yx} & A_{yy} & A_{ys} & B_{yx} & B_{yy} & B_{ys} \\ A_{sx} & A_{sy} & A_{ss} & B_{sx} & B_{sy} & B_{ss} \\ B_{xx} & B_{xy} & B_{xs} & D_{xx} & D_{xy} & D_{xs} \\ B_{yx} & B_{yy} & B_{ys} & D_{yx} & D_{yy} & D_{ys} \\ B_{sx} & B_{sy} & B_{ss} & D_{sx} & D_{sy} & D_{ss} \end{bmatrix} \begin{bmatrix} \epsilon_x^0 \\ \epsilon_y^0 \\ \gamma_{xy}^0 \\ \kappa_x \\ \kappa_y \\ \kappa_{xy} \end{bmatrix} \tag{2.66}$$

Orthotropic plates

For an orthotropic plate:

$$\begin{bmatrix}\sigma_x\\ \sigma_y\\ \tau_{xy}\end{bmatrix} = \begin{bmatrix}E'_x & E'' & 0\\ E'' & E'_y & 0\\ 0 & 0 & G\end{bmatrix}\begin{bmatrix}\epsilon_x\\ \epsilon_y\\ \gamma_{xy}\end{bmatrix} \tag{2.67}$$

where:

$$E'_x = \frac{E_x}{1-\nu_x\nu_y} \tag{2.68}$$

$$E'_y = \frac{E_y}{1-\nu_x\nu_y} \tag{2.69}$$

$$E'' = \frac{\nu_x E_x}{1-\nu_x\nu_y} = \frac{\nu_y E_y}{1-\nu_x\nu_y} \tag{2.70}$$

which gives:

$$\begin{bmatrix}N_x\\ N_y\\ N_{xy}\\ M_x\\ M_y\\ M_{xy}\end{bmatrix} = \begin{bmatrix}E'_x h & E''h & 0 & 0 & 0 & 0\\ E''h & E'_y h & 0 & 0 & 0 & 0\\ 0 & 0 & Gh & 0 & 0 & 0\\ 0 & 0 & 0 & E'_x I & E''I & 0\\ 0 & 0 & 0 & E''I & E'_y I & 0\\ 0 & 0 & 0 & 0 & 0 & GI\end{bmatrix}\begin{bmatrix}\epsilon^0_x\\ \epsilon^0_y\\ \gamma^0_{xy}\\ \kappa_x\\ \kappa_y\\ \kappa_{xy}\end{bmatrix} \tag{2.71}$$

where $I = \frac{h^3}{12}$.

Isotropic plates

For an isotropic plate:

$$\begin{bmatrix}\sigma_x\\ \sigma_y\\ \tau_{xy}\end{bmatrix} = \frac{E}{1-\nu^2}\begin{bmatrix}1 & \nu & 0\\ \nu & 1 & 0\\ 0 & 0 & \frac{1-\nu}{2}\end{bmatrix}\begin{bmatrix}\epsilon_x\\ \epsilon_y\\ \gamma_{xy}\end{bmatrix} \tag{2.72}$$

which gives:

$$\begin{bmatrix}N_x\\ N_y\\ N_{xy}\\ M_x\\ M_y\\ M_{xy}\end{bmatrix} = \frac{E}{1-\nu^2}\begin{bmatrix}h & \nu h & 0 & 0 & 0 & 0\\ \nu h & h & 0 & 0 & 0 & 0\\ 0 & 0 & \frac{(1-\nu)h}{2} & 0 & 0 & 0\\ 0 & 0 & 0 & I & \nu I & 0\\ 0 & 0 & 0 & \nu I & I & 0\\ 0 & 0 & 0 & 0 & 0 & \frac{(1-\nu)I}{2}\end{bmatrix}\begin{bmatrix}\epsilon^0_x\\ \epsilon^0_y\\ \gamma^0_{xy}\\ \kappa_x\\ \kappa_y\\ \kappa_{xy}\end{bmatrix} \tag{2.73}$$

2.3.6 Coupling terms

A_{xy} and D_{xy} are referred to as the coupling terms of the in-plane and bending stiffness matrices, respectively. A_{xy} is related to transverse stress with unidirectional strain. A near-zero value translates to no lateral strain; a negative value translates to lateral expansion; and a positive value translates to lateral contraction. Correspondingly, D_{xy} is related to transverse bending moment with unidirectional curvature. A near-zero value translates to zero Gaussian curvature; a negative value translates to positive Gaussian curvature; and a positive value translates to negative Gaussian curvature.

2.4 Regression analysis

Regression analysis is the process of estimating the relationship between variables. The main sources of information in this section are Cleveland and Devlin[7] and Montgomery, Peck and Vining[15].

2.4.1 Linear regression

In linear regression, the assumption is that there is a linear relationship between the variables x_i and their observed values y_i:

$$y = \beta_0 + \beta_1 x + \varepsilon \tag{2.74}$$

where β_0 and β_1 are the regression coefficients, which are unknown and must be estimated using sample data, and ε is a random error component. The most common form of regression analysis is least squares analysis, which attempts to find the line that minimizes the sum of the squared errors:

$$S(\beta_0, \beta_1) = \sum_{i=1}^{n} (y_1 - \beta_0 - \beta_1 x_i)^2 \tag{2.75}$$

The linear regression model here is:

$$\hat{y} = \hat{\beta}_0 + \hat{\beta}_1 x \tag{2.76}$$

where the least-square estimators $\hat{\beta}_0$ and $\hat{\beta}_1$ are the estimations of β_0 and β_1 respectively such that the difference between the observations y_i and the regression line $\hat{y}$ is minimized. These are given by:

$$\hat{\beta}_0 = \bar{y} - \hat{\beta}_1 \bar{x} \tag{2.77}$$

where $\bar{x}$ and $\bar{y}$ are the averages of x_i and y_i, respectively, and:

$$\hat{\beta}_1 = \frac{\sum_{i=1}^{n} x_i y_i - \frac{\left(\sum_{i=1}^{n} x_i\right)\left(\sum_{i=1}^{n} y_i\right)}{n}}{\sum_{i=1}^{n} x_i^2 - \frac{\left(\sum_{i=1}^{n} x_i\right)^2}{n}} \tag{2.78}$$

The least squares method can be considered a special case of the weighted least squares method:

$$S(\beta_0, \beta_1) = \sum_{i=1}^{n} w_i (y_1 - \beta_0 - \beta_1 x_i)^2 \tag{2.79}$$

where w_i is a weight chosen inversely proportional to the variance of y_i.

2.4.2 Polynomial regression

Polynomial regression attempts to find an nth degree polynomial that fits the data as closely as possible. Table 2.3 shows the form of the regression function for bivariate polynomials up to the 5th degree.

Degree	Form
1	$\beta_0 + \beta_1 x + \beta_2 y$
2	$\beta_0 + \beta_1 x + \beta_2 y + \beta_{11} x^2 + \beta_{12} xy + \beta_{22} y^2$
3	$\beta_0 + \beta_1 x + \beta_2 y + \beta_{11} x^2 + \beta_{12} xy + \beta_{22} y^2$ $+\beta_{111} x^3 + \beta_{112} x^2 y + \beta_{122} xy^2 + \beta_{222} y^3$
4	$\beta_0 + \beta_1 x + \beta_2 y + \beta_{11} x^2 + \beta_{12} xy + \beta_{22} y^2$ $+\beta_{111} x^3 + \beta_{112} x^2 y + \beta_{122} xy^2 + \beta_{222} y^3$ $+\beta_{1111} x^4 + \beta_{1112} x^3 y + \beta_{1122} x^2 y^2 + \beta_{1222} xy^3 + \beta_{2222} y^4$
5	$\beta_0 + \beta_1 x + \beta_2 y + \beta_{11} x^2 + \beta_{12} xy + \beta_{22} y^2$ $+\beta_{111} x^3 + \beta_{112} x^2 y + \beta_{122} xy^2 + \beta_{222} y^3$ $+\beta_{1111} x^4 + \beta_{1112} x^3 y + \beta_{1122} x^2 y^2 + \beta_{1222} xy^3 + \beta_{2222} y^4$ $+\beta_{11111} x^5 + \beta_{11112} x^4 y + \beta_{11122} x^3 y^2 + \beta_{11222} x^2 y^3 + \beta_{12222} xy^4 + \beta_{22222} y^5$

Table 2.3: Form of bivariate polynomials.

2.4.3 Local regression

The loess[8] method (an acronym for locally estimated scatterplot smoothing), as the name suggests, is a method developed for scatterplot smoothing using local fitting. The method estimates a linear[9] or quadratic function at each point x in the data range based on the values of the nearest neighbors to x, using weighted least squares where each neighbor is weighted according to its distance to x. The weight for the neighbor (x_i, y_i) is:

$$w_i(x) = W\left(\frac{\varrho(x, x_i)}{d(x)}\right) \tag{2.80}$$

where ϱ is the distance function, $d(x)$ is the distance to the farthest neighbor to x, and W is the weight function, commonly the tricube function:

[8] Some sources write the acronym with capital letters (LOESS), but the original literature written by those who developed the method do not.[7]

[9] The method using linear functions is sometimes known as the lowess, or locally weighted scatterplot smoothing, method.

$$W(t) = \begin{cases} (1-t^3)^3, & 0 \leq t < 1 \\ 0, & otherwise \end{cases} \tag{2.81}$$

If the distances fall outside of the given range, they can be scaled appropriately.

The loess method with quadratic fitting is especially well suited for surfaces with substantial curvature.

2.4.4 Interpolant analysis

In interpolant analysis, new data points are constructed within the range of a given set of data points. All given data points must fit into the model. Interpolation differs from regression in that regression analysis attempts to create a model that can predict data points outside of the range of the given data points, and only needs to approach the given data points as closely as possible rather than match them exactly.

2.5 Materials

This section intends to briefly introduce some concepts in materials science. The main sources of information in this section are Callister and Rethwisch[6] and Dowling[8].

2.5.1 Elastic and plastic deformation

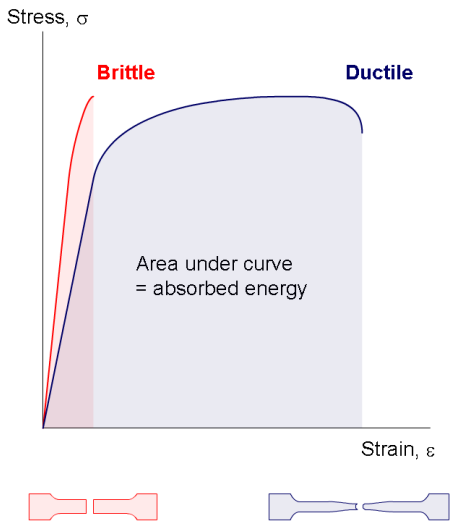

Figure 2.12: Stress-strain diagram. Image ©User:Amgreen / Wikimedia Commons / CC-BY-SA-3.0.

Deformation of a body being subjected to a load can be classified as either elastic or plastic. Elastic deformation is recovered immediately upon unloading, while plastic deformation is permanent. Where you have elastic deformation, stress and strain is generally proportional. On a stress-strain diagram (such as figure 2.12), the area of elastic deformation is then shown as a straight line. At a certain point, the material yields and transitions to plastic deformation, where a relatively small increase in stress will cause a large additional deformation. The stress at which deformation transitions from elastic to ductile is known as the yield strength σ_0. The stress-strain curve eventually reaches a maximum stress value – the ultimate tensile strength σ_u – before decreasing until finally reaching fracture. A material that can sustain large amounts of plastic deformation before fracture is considered ductile, whereas a brittle material will fracture after sustaining little to no plastic deformation.

2.5.2 Heat-affected zone

When a material undergoes welding or a heat-intensive cutting operation (such as laser cutting), a region around the weld or cut may be affected by the heat in such a way that the material experiences changes in microstucture and properties, such as residual stresses forming that weaken the area. This region is known as the heat-affected zone, or HAZ.

2.6 Laser cutting

Laser cutting is a technology for cutting materials using a high-power laser beam intensified by a lens and/or a mirror. In addition to cutting, laser cutters can also engrave materials.

2.6.1 Advantages and disadvantages

Advantages of laser cutting over traditional cutting are numerous:

- Versatility. Simple and complex designs may be cut or engraved into a wide variety of materials using the same laser cutting machine, where one may have needed to use multiple traditional machines.
- Precision. Cuts are very accurate with a small kerf, and the laser does not wear during cutting.
- Reduced risk of contamination. There is no cutting edge that may be contaminated by, or contaminate, the material.
- Less warping. Heat generated by traditional cutting may warp the material, whereas with laser cutting, the area subjected to heat is very small, reducing the chance of warping.

Laser cutting also has its disadvantages – for example, one must be very careful in choice of material, to avoid damage to the machinery or to the human body due to harmful combustion gases; as well as the machine settings, to avoid combustion. However, the

advantages outweigh the disadvantages to such a degree that laser cutting is ever increasing in popularity.

2.6.2 Hazards

Some of the hazards to keep in mind when selecting a material for laser cutting are[4, 10]:

Flammability. Some materials are more likely than others to combust due to various reasons. Polycarbonate easily overheats due to its ease of absorbing infrared light from the laser, while foamed plastics are a fire hazard due to having large amounts of surface area exposed to oxygen.

Explosion. Porous, hard materials that have the ability to absorb moisture may have pockets of liquid trapped inside, causing steam explosions when heated by the laser.

Damage to machinery. If a material releases hydrogen chloride gas, it may corrode parts of the laser cutter. Highly reflective materials should also be avoided as the laser may reflect back into the machinery, damaging it.

Damage to respiratory system. Materials containing halogens, such as PVC, release halogen gases that damage the lungs and respiratory system.

Damage to central nervous system. Materials containing styrene, such as ABS and polystyrene, release styrene gas which can cause styrene sickness with symptoms such as irritation of skin, eyes and upper respiratory tract, or, with chronic exposure, effects on the central nervous system.

Death. Materials containing a carbon-nitrogen bond, such as nylon and ABS plastic, create hydrogen cyanide gas when burned, which is lethal as it hinders the human body from using oxygen.

It must be noted, however, that some of the materials that release toxic gases can still be cut if the laser cutter has the proper ventilation equipment.

Chapter 3

Method

3.1 Web application

As part of his master's thesis on flexure patterns, Østmo created code for a flexure pattern generator[17] which generates vector graphic files of a pattern based on given parameters. However, this generator does not have a user interface for entering parameters. In order to facilitate use of this code, a web application was created.

3.1.1 Original code

The original code was written in Python with the help of the NumPy and Shapely libraries. As mentioned earlier, Numpy is a library for scientific computing with Python, including support for large, multi-dimensional arrays and matrices and high-level mathematical functions to operate on these. Shapely adds geometrical objects and operations on these. The code creates the flexure pattern and its parts as polygonal shapes and outputs these as vector graphics files.

3.1.2 Adding functionality

It was desirable to add some extra functionality to the flexure pattern generator. First, the option to render cuts in the pattern as slits rather than gaps. This was done by adding a boolean variable which indicates whether the cut should be a slit (false) or a gap (true). In the vector graphics files, the slits would then be rendered as lines. Second, the option to generate an Abaqus script that automatically creates parts in Abaqus. This was done by generating the text needed for the script and outputing it as a Python file.

3.1.3 Creating a web application

The web application was created using Flask, a web framework written in Python. The framework was mainly chosen due to the original code already being in Python, but also

because it is versatile and easy to use. The web application uses the WTForms library to handle forms, which is an important part of the application as this is how the user enters and submits parameters to the application.

3.2 Simulation

The program used for simulation was Abaqus, a unified finite element analysis (FEA) solution developed by Simulia. The program was used to simulate plates and load cases equivalent to those used in the experiment (see section 3.3) in order to check the correlation between real life and simulations. The general procedure was as follows:

1. Run simulation on single unit cell to find stiffness matrix.
2. Use stiffness matrix in shell simulation.
3. Gather nodal results from shell simulation.
4. Visualize results.

This section gives a brief overview of the procedure.

3.2.1 Part creation

The creation of the parts for simulating was done by running scripts generated by the flexure pattern generator, see section 3.1.

3.2.2 Finding the stiffness matrix

Using a script, simulations were run on the unit cell for load cases of pure strain in the x direction; pure strain in the y direction; pure shear; pure bending in the x direction; pure bending in the y direction; and pure twist. For the first load case:

$$\begin{bmatrix} N_x \\ N_y \\ N_{xy} \\ M_x \\ M_y \\ M_{xy} \end{bmatrix} = \begin{bmatrix} A_{xx} & 0 & 0 & 0 & 0 & 0 \\ A_{xy} & 0 & 0 & 0 & 0 & 0 \\ A_{xs} & 0 & 0 & 0 & 0 & 0 \\ B_{xx} & 0 & 0 & 0 & 0 & 0 \\ B_{xy} & 0 & 0 & 0 & 0 & 0 \\ B_{xs} & 0 & 0 & 0 & 0 & 0 \end{bmatrix} \begin{bmatrix} 1 \\ 0 \\ 0 \\ 0 \\ 0 \\ 0 \end{bmatrix} \tag{3.1}$$

and similarly for the other load cases. Then:

$$A_{xx} = \frac{\sum F_x^X}{\Delta_y} \tag{3.2}$$

$$A_{xy} = \frac{\sum F_y^Y}{\Delta_x} \tag{3.3}$$

$$A_{xs} = \frac{1}{2}\left(\frac{\sum F_y^Y}{\Delta_x} + \frac{\sum F_x^X}{\Delta_y}\right) \tag{3.4}$$

$$B_{xx} = \frac{\sum M_x^X}{\Delta_y} \tag{3.5}$$

$$B_{xy} = \frac{\sum M_y^Y}{\Delta_x} \tag{3.6}$$

$$B_{xs} = \frac{1}{2}\left(\frac{\sum M_{xy}^Y}{\Delta_x} + \frac{\sum M_{xy}^X}{\Delta_y}\right) \tag{3.7}$$

$$\tag{3.8}$$

where e.g. $\sum F_x^X$ denotes the sum of the forces in the x direction on the X side, which is the left side on figure 2.11, etc. For curvature:

$$B_{xx} = \frac{\sum F_x^X}{\Delta_y} \tag{3.9}$$

$$B_{xy} = \frac{\sum F_y^Y}{\Delta_x} \tag{3.10}$$

$$B_{xs} = \frac{1}{2}\left(\frac{\sum F_y^Y}{\Delta_x} + \frac{\sum F_x^X}{\Delta_y}\right) \tag{3.11}$$

$$D_{xx} = \frac{\sum M_x^X}{\Delta_y} \tag{3.12}$$

$$D_{xy} = \frac{\sum M_y^Y}{\Delta_x} \tag{3.13}$$

$$D_{xs} = \frac{1}{2}\left(\frac{\sum M_{xy}^Y}{\Delta_x} + \frac{\sum M_{xy}^X}{\Delta_y}\right) \tag{3.14}$$

$$\tag{3.15}$$

The process is repeated for each load case to find the full stiffness matrix.

3.2.3 Shell simulation

A shell element in the shape of the plate is assigned the stiffness matrix found by the method above. Boundary conditions and loads are added to the model before the simulation is run.

When assigning a step to the simulation, there is an option to turn NLGEOM on or off. NLGEOM stands for nonlinear geometry, and will take this into account during calculations when large deformation takes place in the simulation.

3.2.4 Result gahering

In order to facilitate the gathering of results, multiple node sets are defined on the mesh before simulation. The nodes are located in the same spots as the gathered data points from the experiment. Figure 3.1 shows the node sets as red dots on a simulated plate, where each row is a node set – this is to make the values easier to format as a matrix rather than as a list.

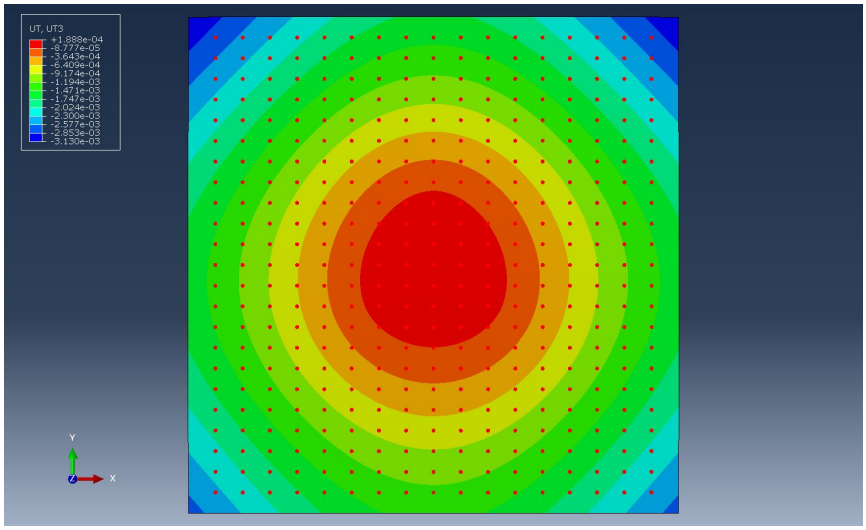

Figure 3.1: Abaqus screen showing node sets.

A script is then run to gather the displacement at each node and write them to a text file, which can then be imported into Excel.

3.2.5 Visualization

A program was written in Python to facilitate visualization. The program uses the following important libraries:

Numpy is a library for scientific computing with Python, including support for large, multi-dimensional arrays and matrices and high-level mathematical functions to operate on these.

Pandas provides data manipulation and analysis tools.

Matplotlib allows plotting of data in Python.

The program uses Pandas to import data from Excel sheets as dataframes. Then, Numpy is used to interpolate missing data, if any. Finally, the surface is plotted using Matplotlib, which also automatically saves the plots as image files.

3.3 Experiment

An experiment was performed to see how a patterned plate would react under different load cases, and to see how well simulations correspond to real life.

3.3.1 Equipment

Flexure pattern generator

The flexure pattern generator, originally coded by Østmo and expanded upon by the author of this text, was used to generate patterns that could be fed more or less directly into the laser cutter.

Laser cutter

In order to create a pattern in the specimen for testing, a laser cutter was used – specifically, an Epilog Laser Fusion M2. This is a small-format, $120\,\mathrm{W}$ laser cutter with a $1016 \times 711\,\mathrm{mm}$ workspace. Being less powerful than larger machines for industrial use, it might not be able to cut certain materials as well or at all, sometimes depending on the thickness of the material. For example, ABS cuts very well on a more powerful laser cutter, but might exhibit melting on a less powerful laser cutter. For this reason, most of the application-specific information on materials is gathered from maker space communities rather than commercial manufacturers.

Laser cutter jobs are sent to the machine from the computer via software. Figure 3.2 shows the dialog screen for adjusting the laser cutter's settings[10]. The following settings can be adjusted:

Resolution. Determines the amount of lasered dots per inch when raster engraving.

Default Settings. For dual-source machines, one can select whether to use a CO2 or fiber laser for the job – however, the machine used in this experiment only uses CO2. Auto focus, when toggled on, tells the machine to move the work table automatically to the correct position, where the focus of the laser is on top of the piece or at a given offset.

Options. Sets options related to the job.

Center-Engraving. Sets the reference point for engraving.

Rotary options. For using the optional 3-Jaw Chuck Rotary Attachment, which the machine used in this experiment does not have.

Job Type. Raster mode is used for engraving, while vector mode is used for cutting.

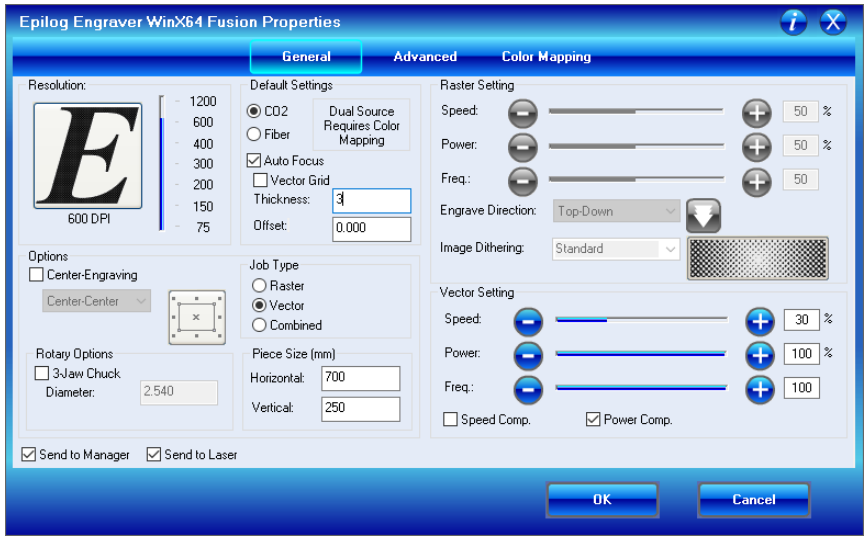

Figure 3.2: The laser cutter's dialog screen.

Piece Size. By entering the size of the piece, one can easily see whether the design exceeds it.

Raster Setting. Options for engraving, not relevant for this experiment.

Vector Setting. Sets options related to the output of the laser.

Speed is adjustable from $1 - 100\,\%$ and refers to the speed of the carriage.

Power is adjustable from $0 - 100\,\%$ and refers to the amount of laser energy.

Frequency is adjustable from $0 - 100$ and refers to the number of laser pulses per inch of travel.

Speed Comp. halves the speed.

Power Comp. reduces the laser output in curves where the carriage speeds slows.

Test rig

An aluminium frame was built from which the plates could be suspended. Figure 3.3 shows the test rig with the following items labeled:

1. Aluminium profiles used to build the frame.
2. Eye bolts connected to the alumiunium crossbeams.
3. Steel wires tied to the eye bolts on top and the hooks on the bottom. The wires are thin enough to be drawn taut by the weight of the patterned plate, and strong enough not to be elongated by said weight.

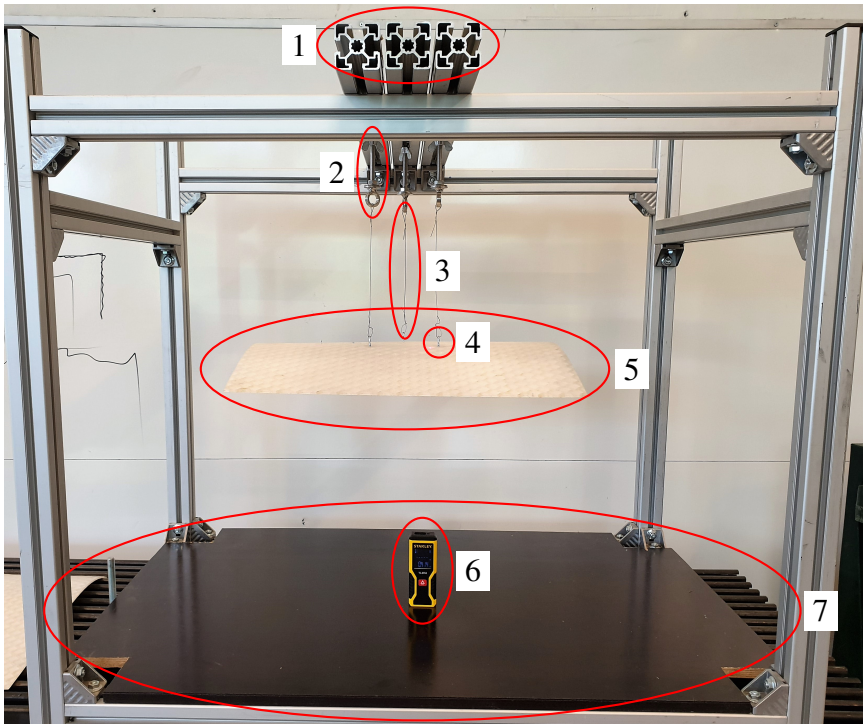

Figure 3.3: Test rig.

4. Hook screws screwed into the patterned plate in order to suspend the plate from the wires.
5. Plate with laser cut flexure pattern.
6. Laser distance measurer used to measure the distance from the bottom plate to the patterned plate.
7. Bottom plate which is level with the ground.

Measuring device

To measure the distance from the bottom plate to the patterned plate, a Stanley TLM50 laser distance measurer was used. The device measures distance with a resolution of $1\,\mathrm{mm}$ and an accuracy of $\pm 3\,\mathrm{mm}$.

3.3.2 Specimens

Material selection

In choosing a material for the experiment, certain aspects must be taken into account. First, the material must be appropriate for testing, leading to meaningful results. Second, since

the pattern is to be cut into the specimens using a laser cutter, the material must be suitable for laser cutting.

One of the purposes of the experiment is to measure deformation. Thus, the material should be ductile, as a brittle material will break before significant deformation has taken place. For easily measurable and replicable results, the material should also be homogeneous and isotropic. For these reasons, a metal or a polymer are the most suitable candidates.

The decision was made to use a polymer, mainly because many polymers are very well suited for laser cutting. In contrast, metals are very difficult to cut using lasers due to their high reflectivity – in fact, there is a danger of the laser reflecting back into the optics, damaging the machine – and in most cases can only be engraved.

An additional benefit of choosing a polymer is low density, making the specimens easier to handle.

Some polymers that were considered are ABS, PMMA, acetal, and PETG.

Acrylonitrile butadiene styrene (ABS) is resistant to heat and tends to melt instead of vaporize, which is a fire hazard as well as potentially damaging to the machine. It also releases cyanide gas as a combustion product.

Poly(methyl methacrylate) (PMMA) is a very popular material for laser cutting, leaving sharp, clean edges without releasing harmful combustion products, but is very brittle.

Acetal also cuts very well, but residual stresses in the material may lead to warping, especially in thin sheets. In addition, its combustion products include formaldehyde.

Glycol-modified polyethylene terephthalate (PETG) is a very popular material for filaments used in 3D printing, but less common in laser cutting. While it does exhibit some melt, there are no significant hazards in laser cutting PETG, and it is a durable and ductile material. For these reasons, PETG was the chosen material for this experiment.

Polyethylene terephthalate (PET, fig. 3.4d) is a semi-crystalline polymer synthesized from terephthalic acid (fig. 3.4a) and ethylene glycol (fig. 3.4b). Copolymerizing PET by replacing some (50% or less) of the ethylene glycol in the polymer chain with cyclohexane dimethanol (CHDM, fig. 3.4c) results in glycol-modified PET (PETG, fig. 3.4e)[19]. CHDM monomers are much larger than ethylene glycol and do not allow the polymer chains to be packed as tightly, which reduces the crystallinity and makes the material amorphous[11]. This in turn lowers the melting temperature. PETG retains the strength and durability of PET while also making it more ductile and easier to laser cut.

Flexure pattern

The flexure pattern chosen for the experiment was a YdX cmm pattern, as its negative Poisson's ratio might produce some interesting results. Figure 3.5 shows an illustration of the simulated LET cmm unit, and table 3.1 shows the measurements of each colored part. Rather than having cut-outs, the cuts are mere slits with a width equal to the kerf of the

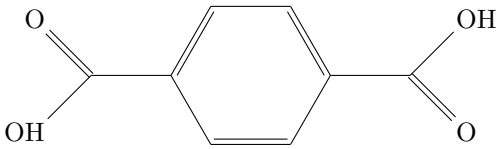

(a) Terephthalic acid

(b) Ethylene glycol (1,2-ethanediol)

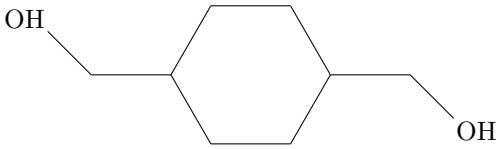

(c) Cyclohexane dimethanol (1,4-cyclohexanedimethanol)

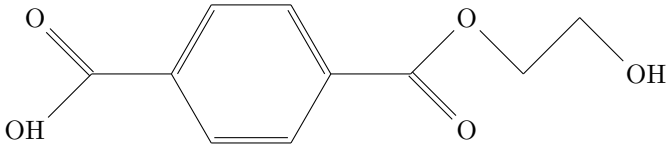

(d) Polyethylene terephthalate (PET)

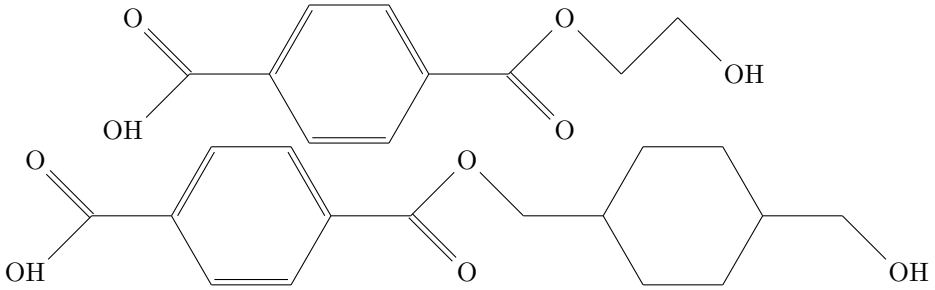

(e) Glycol-modified polyethylene terephthalate (PETG)

Figure 3.4: Constituent molecules of PET-G.

laser cutter. The units are repeated 18 times in the horizontal direction and 24 times in the vertical direction for the pattern seen in figure 3.6.

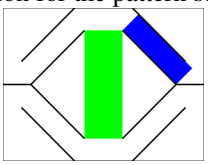

Figure 3.5: YdX cmm unit.

Color	Direction	Measurement
Blue	Long side	10 mm
Blue	Short side	3 mm
Green	Horizontal	5 mm

Table 3.1: Measurements for YdX cmm unit.

Load cases

Results were measured for three load cases:

1. No load; the plate is only affected by gravitational body forces. This was measured for two plates.
2. One concentrated load in the middle of the plate.
3. Two concentrated loads on the left and right side of the plate, symmetrical about the middle of the plate.

An illustration of the plates used for testing is shown in figure 3.6. The plates had three hook screws screwed into them from the top side, from which the plates could be suspended. The locations are shown as blue dots in the figure. On one plate, a hook screw was screwed in from the underside from which a load could be attached, the location of which is shown as a green dot in the figure, representing load case 2. On another plate, two hook screws were screwed in from the underside, the locations of which are shown as red dots in the figure, representing load case 3.

As mentioned in section 3.3.1, the wires from which the plates are supended are drawn taut and do not elongate. This gives a boundary condition where those points have zero translation in the z direction, where the z axis is positive in the upwards direction – i.e., $w = 0$.

Plate 1 has a mass of $789.8\,\mathrm{g}$ and plate 2 has a mass of $792.0\,\mathrm{g}$, for an average mass of $790.9\,\mathrm{g}$. In load case 2, the load has a mass of $1074.4\,\mathrm{g}$. In load case 3, one load has a mass of $545.4\,\mathrm{g}$ and the other a mass of $547.0\,\mathrm{g}$, for an average mass of $546.2\,\mathrm{g}$.

3.3.3 Specimen preparation

Laser cutting

Before laser cutting the patterns, several tests were made to find the optimal settings for the laser cutter. Even if the laser cuts through the top of the material, the cut might not go all the way through, as shown by the angle in the kerf in figure 3.7. In e-mail correspondence with Polulu, a company that offers laser cutting on PETG, their suggestion was to set the focus to the top surface of the material and to use maximum power and frequency while testing for the maximum speed at which the laser will cut through the material. Thus, in testing, the power was set to $100\,\%$ and the frequency to 100 pulses per inch, while speed

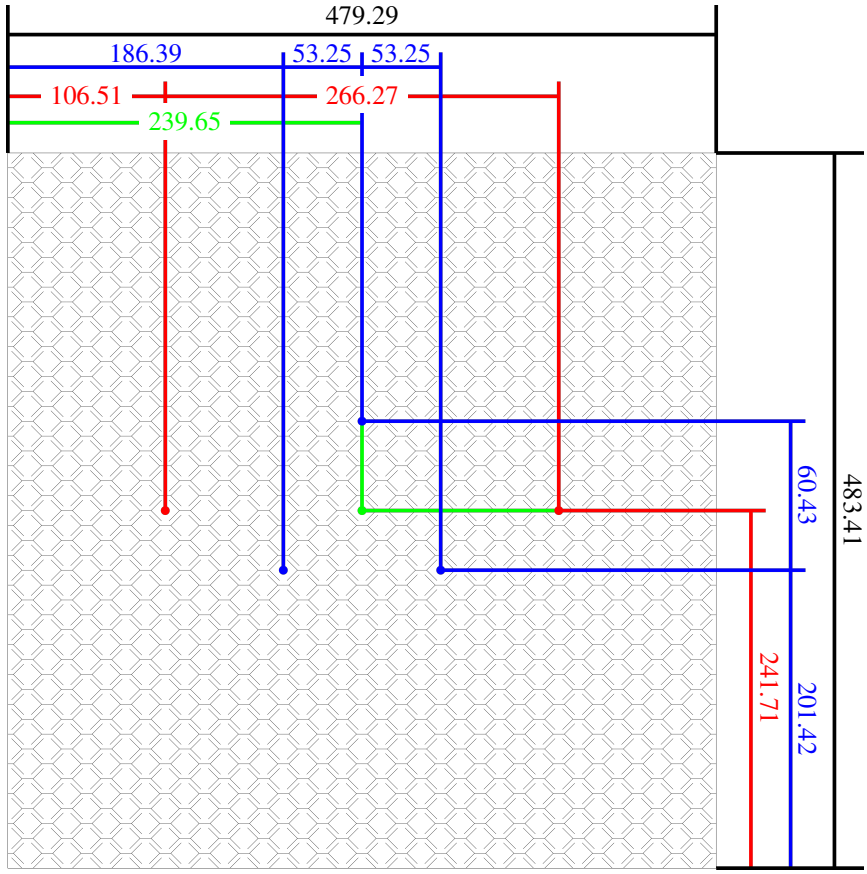

Figure 3.6: Pattern in black; suspension points in blue; middle load point in green; side load points in red.

was variable. Figure 3.8a shows, from left to right, $20 \times 20\,\mathrm{mm}$ samples cut at $100\,\%$, $80\,\%$, $60\,\%$, $40\,\%$ and $20\,\%$ speed, with the top samples being cut in one pass and the bottom samples being cut in two passes. Only the samples cut at $20\,\%$ speed, as well as the sample cut at $40\,\%$ speed in two passes, cut through the thickness of the plate.

Another test was made to check how the width of the cutouts affected the ability to cut through the material. Figure 3.8b shows, from left to right, samples with a height of $20\,\mathrm{mm}$ and a width of $20\,\mathrm{mm}$, $10\,\mathrm{mm}$, $5\,\mathrm{mm}$, $2.5\,\mathrm{mm}$ and $1\,\mathrm{mm}$, all cut at 20% speed and with two one pass at the top and two passes at the bottom. On narrower cuts, warping in the heat-affected zone caused the cut-out to fuse back into the material from which it is cut. All samples cut through except the ones with the smallest width of $1\,\mathrm{mm}$, which stuck to the material at both one and two passes.

To ensure that the laser would cut through for the whole pattern, the material was cut at $17\,\%$ speed in two passes. The narrowest part of the pattern – i.e. the flexure – is $3\,\mathrm{mm}$ in width, which is wide enough to avoid the warping effects seen above. Figure 3.9 shows

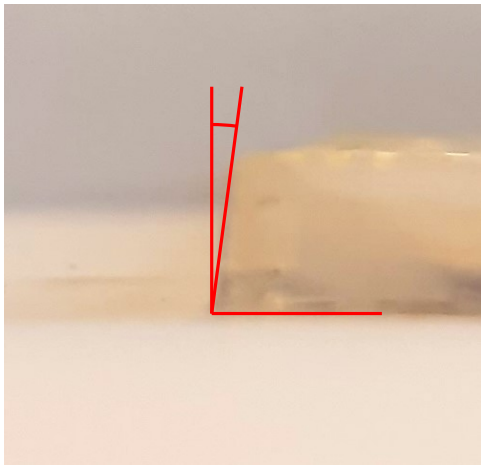

Figure 3.7: Zoomed-in sample showing angled kerf.

one of the plates used in the experiment to the left, with measurements as seen in figure 3.5, and a version with twice as large measurements to the right. It took around $45\,\mathrm{min}$ to cut one pattern.

In figure 3.9 one can also see a white residue on the plates. This is vaporized material settling as dust on the plates. Although having a rather unpleasant smell, the residue is not harmful, but one should still avoid inhaling the residue as it may settle in the lungs. In addition, one must take care to clean the machine, and especially the optics, after laser cutting to avoid damage to the machine.

Dross

In figure 3.8, one can clearly see, in addition to discoloration, increasing amounts of melted material on the surface with lower speed and more passes. The melted material, known as dross, comes from the cuts, and is blown across the surface by the machine's ventilation system. The dross was scraped off with a knife after laser cutting, see figure 3.10. After scraping, the plates were wiped with a damp cloth to clean off the scrapings as well as the white residue.

Preparing for measuring

Due to the transparent nature of the material, the laser distance measurer had trouble correctly measuring the distance from the bottom plate to the patterned plate (see figure 3.3), as the laser beam went through the plate rather bouncing back into the device. Therefore, two layers of matte white spray paint were applied to the plates to make them opaque.

(a) Speed tests.

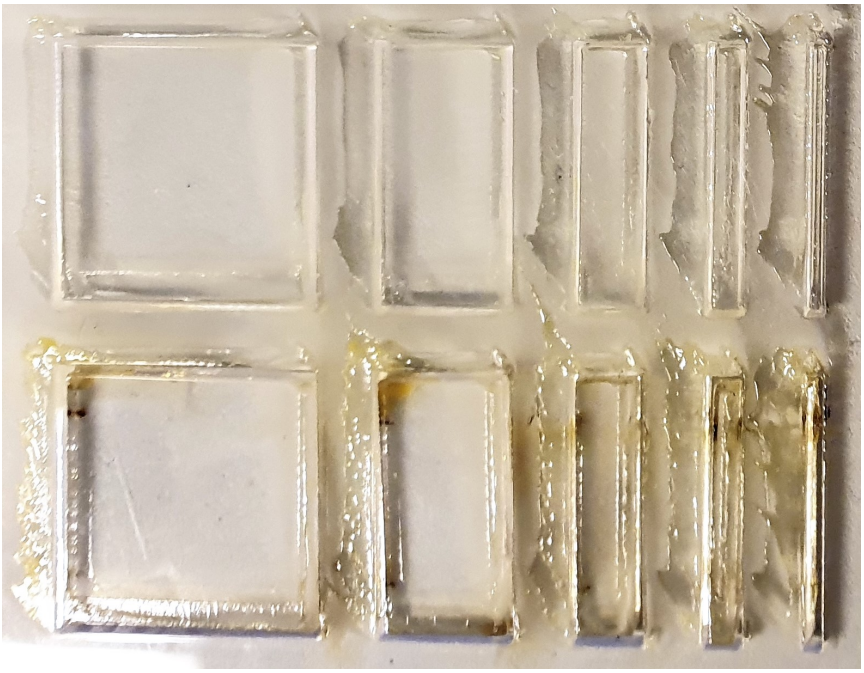

(b) Width tests.

Figure 3.8: Laser cutter tests.

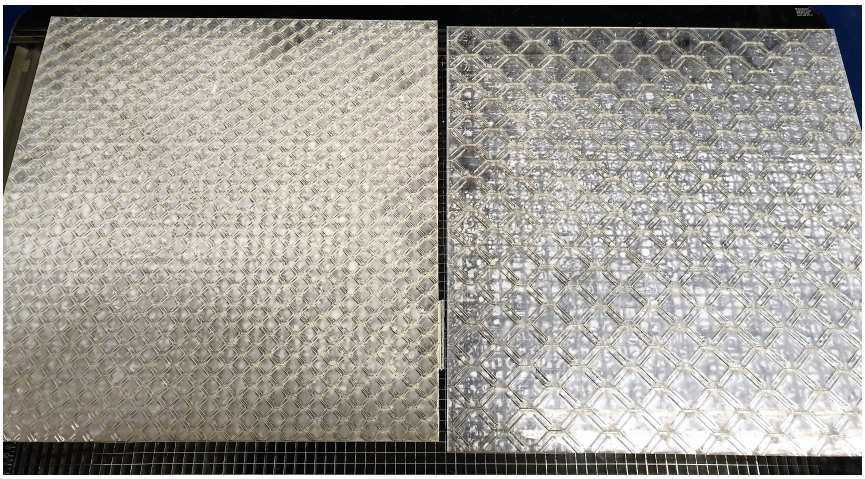

Figure 3.9: Two plates fresh out of the laser cutter.

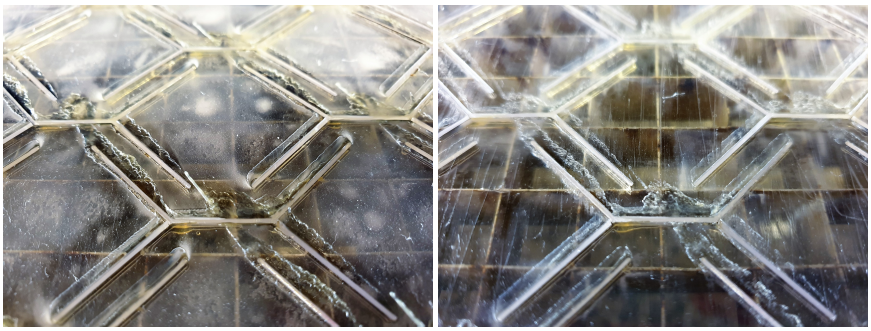

(a) Before scraping. **(b)** After scraping.

Figure 3.10: Plate before and after scraping off dross.

3.3.4 Method

Figure 3.11: Load suspended from plate.

The following steps were followed for each load case:

1. Suspend the plate from the wires.
2. Screw in or out the eye bolts to adjust the height of the three suspension points for the plates until the laser distance measurer measures the same distance at each suspension point.
3. For load case 2 and 3, add one or two loads respectively to the plate.
4. Use the laser distance measurer to measure the distance from the bottom plate to the center of each unit on the plate.
5. For each data point, subtract the distance to the suspension points to get relative displacement in the z direction.

Figure 3.11 shows how the loads, in the form of large bolts, are suspended from the plate by hook screws. The figure also shows how the plates are spray painted on the bottom side for opacity. Figure 3.12 shows all three load cases.

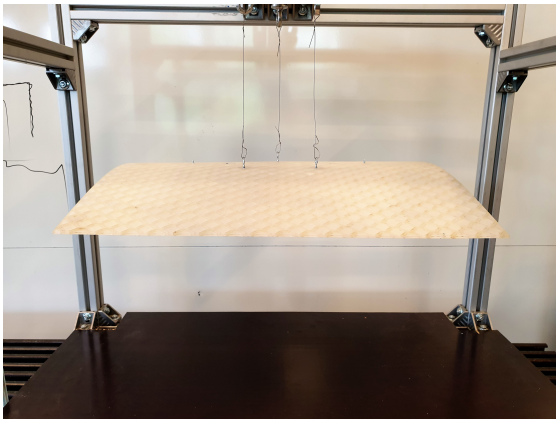

(a) Load case 1: No loads, only plate weight.

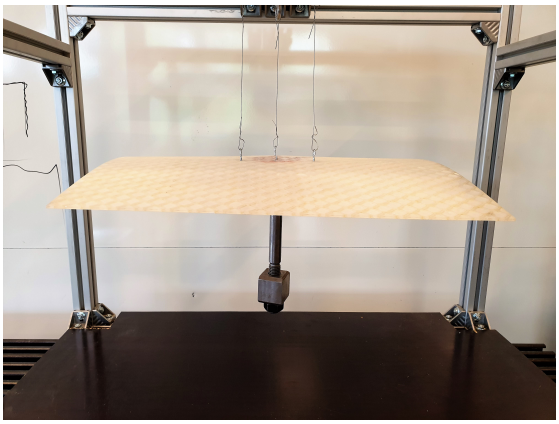

(b) Load case 2: One load in the center of the plate.

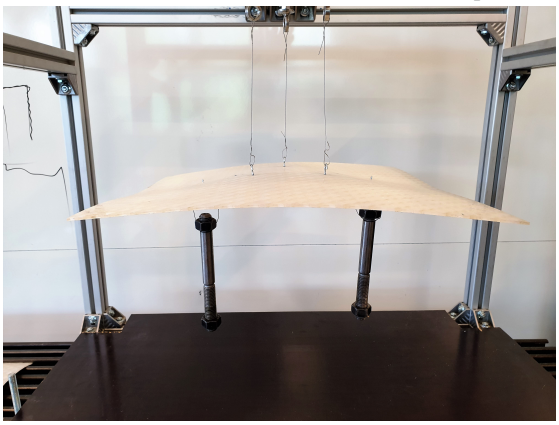

(c) Load case 3: Two loads on the left and right side of the plate.

Figure 3.12: Load cases.

Chapter 4

Results and Discussion

4.1 Material testing

Before performing experiments on sheets with the flexure pattern cut into them, it was desirable to find some of the elastic properties of the material. As PETG sheets are theoretically isotropic, this was done by performing uniaxial tensile tests on four identical specimens.

The specimens were cut from the same sheet of PETG material using a laser cutter. Figure 4.1 shows a sketch of the specimen geometry with dimensions in millimeters in accordance with ASTM D638-14[2]. In addition, the thickness of the plate, and thus the specimens, is $3.0\,\mathrm{mm}$.

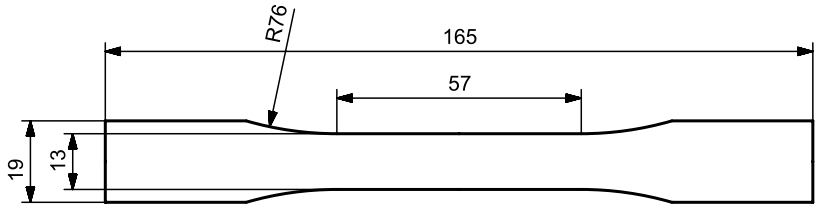

Figure 4.1: Tension test specimen dimensions (in mm).

As only the linear elastic portion of the stress-strain curve is of interest, the tests were stopped when significant necking was observed. As seen in figure 4.2, the specimens displayed necking at a 45 degree angle. This corresponds to the plane of maximum shear.

Strain data was gathered from two strain gauges glued to the specimen, one along the axial direction and one along the lateral direction. Load data was gathered from the test machine itself. The data was then processed using Pandas and visualized using Matplotlib. The stress values were obtained using the formula for average normal stress:

Figure 4.2: Specimens after tension testing.

$$\sigma = \frac{N}{A_0} \tag{4.1}$$

where σ is the average normal stress, N is the normal force and A_0 is the original cross-sectional area, in this case the thickness multiplied by the width of the narrow part of the specimen.

Figure 4.3 shows the stress-strain diagram for all specimens individually in figure 4.3a-d, and all on the same figure in figure 4.3e. Some tests were recorded for a longer time than others, which is why e.g. figure 4.3e has a longer-running curve than figure 4.3a. The diagrams show linear-elastic behavior for the material at the beginning of the test, before the slopes begin to decrease as deformation begins to transition from elastic to plastic.

Figure 4.4 shows the lateral-axial strain diagram for all specimens individually in figure 4.4a-d, and all on the same figure in figure 4.4e. The diagrams show a linear relationship between lateral and axial strain.

Numpy was then used to find linear regression lines for the linear portions of the graphs. On the stress-strain diagrams, this was measured at $\epsilon_{axial} = 1 - 6\,\mathrm{mm/m}$, and on the lateral-axial strain diagram, at $\epsilon_{axial} = 3 - 7\,\mathrm{mm/m}$. Since for an isotropic material:

$$E = \frac{\sigma}{\epsilon} \tag{4.2}$$

and:

$$\nu = -\frac{\epsilon_{lateral}}{\epsilon_{axial}} \tag{4.3}$$

Those regression lines could then be used to find approximate values for the Young's modulus E and Poisson's ratio ν for the PETG sheet, as seen in table 4.1, by using the average value over all tests.

Table 4.1 also shows the density ρ. This was found by cutting out $20 \times 20\,\mathrm{mm}$ samples from a $3\,\mathrm{mm}$ thick plate and weighing those. With a $0.2\,\mathrm{mm}$ kerf from the laser, the sides of the samples measured $19.8\,\mathrm{mm}$. The samples were weighed individually and

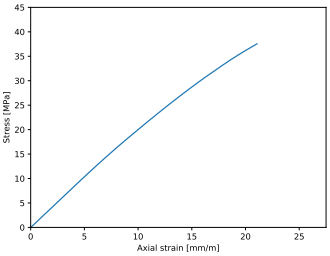

(a) Stress-strain diagram from test 1.

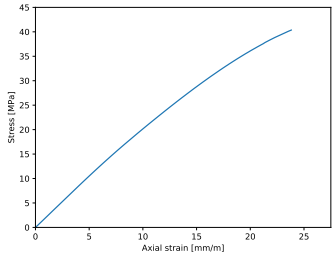

(b) Stress-strain diagram from test 2.

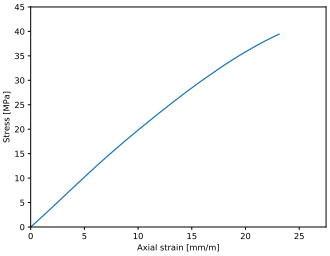

(c) Stress-strain diagram from test 3.

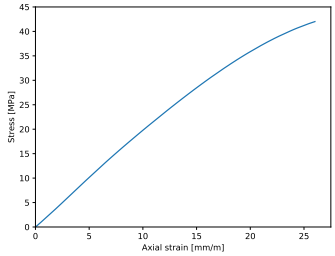

(d) Stress-strain diagram from test 4.

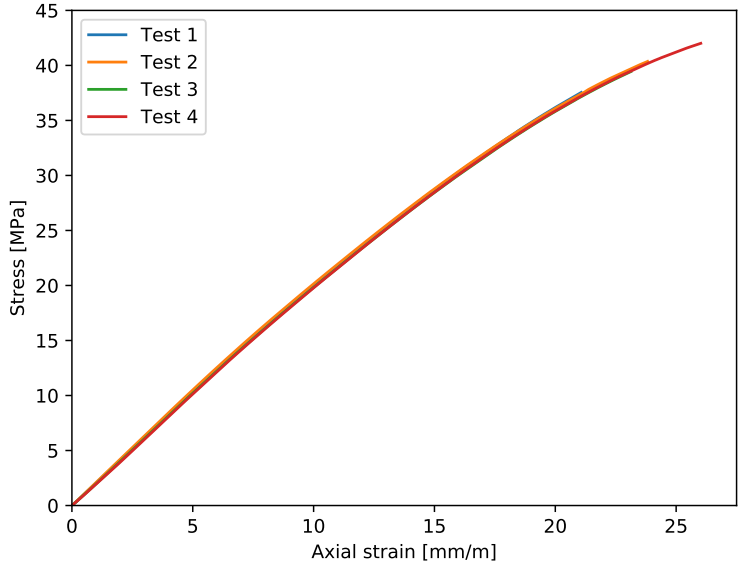

(e) Stress-strain diagram from all tests.

Figure 4.3: Stress-strain diagrams from tensile testing.

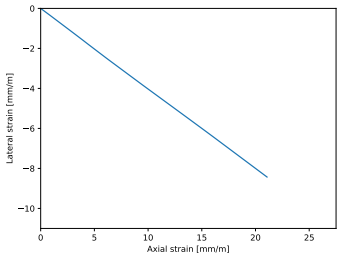

(a) Lateral-axial strain diagram from test 1.

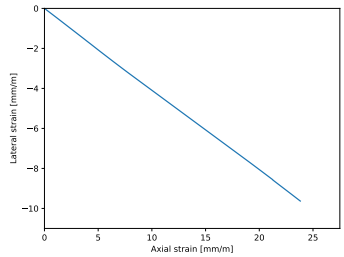

(b) Lateral-axial strain diagram from test 2.

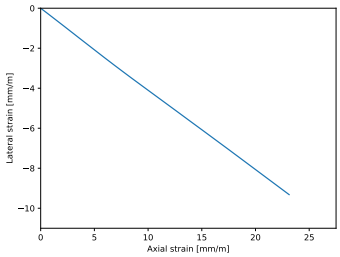

(c) Lateral-axial strain diagram from test 3.

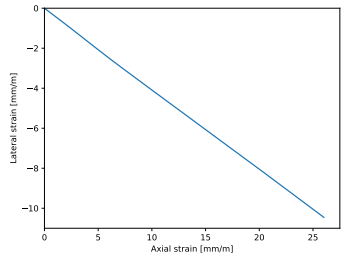

(d) Lateral-axial strain diagram from test 4.

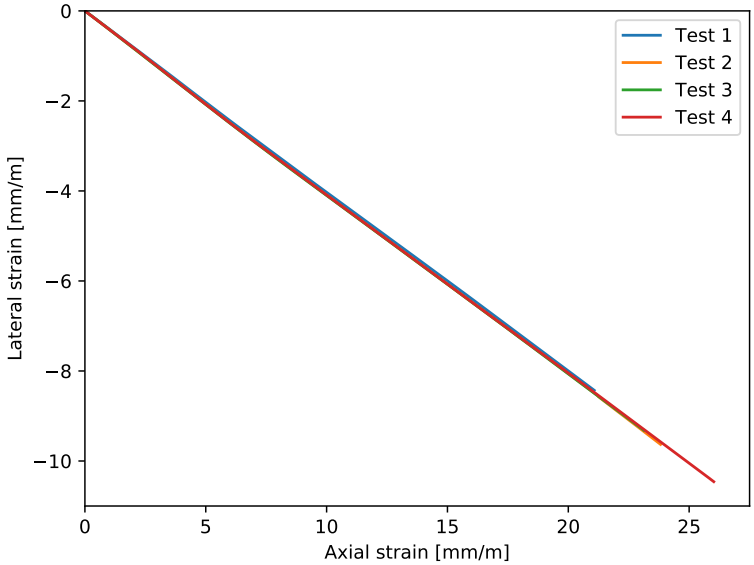

(e) Lateral-axial strain diagram from all tests.

Figure 4.4: Lateral-axial strain diagrams from tensile testing.

E	$2.08\,\mathrm{GPa}$
ν	0.42
ρ	$1.19\,\mathrm{g/cm^3}$

Table 4.1: Properties of PETG sheets.

all together (8 samples), giving an average mass of $1.4\,\mathrm{g}$. The density was found by putting this value into the following formula:

$$\rho = \frac{m}{V} \tag{4.4}$$

where m is the mass and V is the volume.

4.1.1 Discussion

The manufacturer lists a value for Young's modulus at $E = 2.2\,\mathrm{GPa}$[1], while other sources list average values between $1.8\,\mathrm{GPa}$ and $2.8\,\mathrm{GPa}$[13, 14]. The experimental value is thus 5.6% lower than the manufacturer's estimate, but falls within the average values. Values for Poisson's ratio for PETG are harder to find and is not listed by the manufacturer at all, but some sources list average values between 0.3 and 0.4[3, 9]. The manufacturer lists a value for the density at $\rho = 1.27\,\mathrm{g/cm^3}$[1], while other sources list average values between $1.23\,\mathrm{g/cm^3}$ and $1.29\,\mathrm{g/cm^3}$[13, 14]. The experimental value is thus 6.3% lower than the manufacturer's estimate and 3.3% lower than the lowest average value. It must be noted that the scale used for weighing the samples had a resolution of $0.1\,\mathrm{g}$, which is poor at such low weights.

Due to the linear relationship between E and the stiffness matrix, a 5.6% decrease in E amounts to a 5.6% decrease in the stiffness coefficients. The relationship between Poisson's ratio ν and the stiffness matrix, however, is not linear. Figure 4.5 shows the results of running simulations on a YdX unit cell with the same measurements as in the experiment, with properties as found in material testing, but with variable Poisson's ratio. The graphs show a gradually changing slope for each stiffness coefficient.

Although the manufacturer does not list Poisson's ratio for the material, online literature suggests that it is typically between 0.3 and 0.4, which is lower than the value found in testing, i.e. 0.42. Table 4.2 shows the values of the stiffness coefficients at a Poisson's ratio of 0.42, 0.4 and 0.3, as in figure 4.5, as well as the percent change in each stiffness coefficient. For example, a Poisson's ratio of 0.4 presents a $0.09\,\%$ increase in the value of A_{11} compared to a Poisson's ratio of 0.42. The table shows that a change in Poisson's ratio from 0.42 to 0.4 – a $4.76\,\%$ decrease – has a small effect on the stiffness matrix, the largest difference being a $1.21\,\%$ increase in D_{66}. A larger change in Poisson's ratio, from 0.42 to 0.4 – a $28.57\,\%$ decrease – has a greater effect. While the in-plane stiffness matrix $\mathbf{A}$ does not change much, the bending stiffness matrix $\mathbf{D}$ displays a minimum difference of a $3.10\,\%$ increase in D_{11} and a maximum difference of a $7.84\,\%$ increase in D_{66}.

Density does not have an impact on the stiffness matrix, but inaccuracies in the density have an impact on calculations of displacement and strain due to gravitational body forces.

In this case, due to the fact that all four tensile tests yielded almost identical stress-strain and lateral-axial strain graphs, it can be assumed that the Young's modulus and

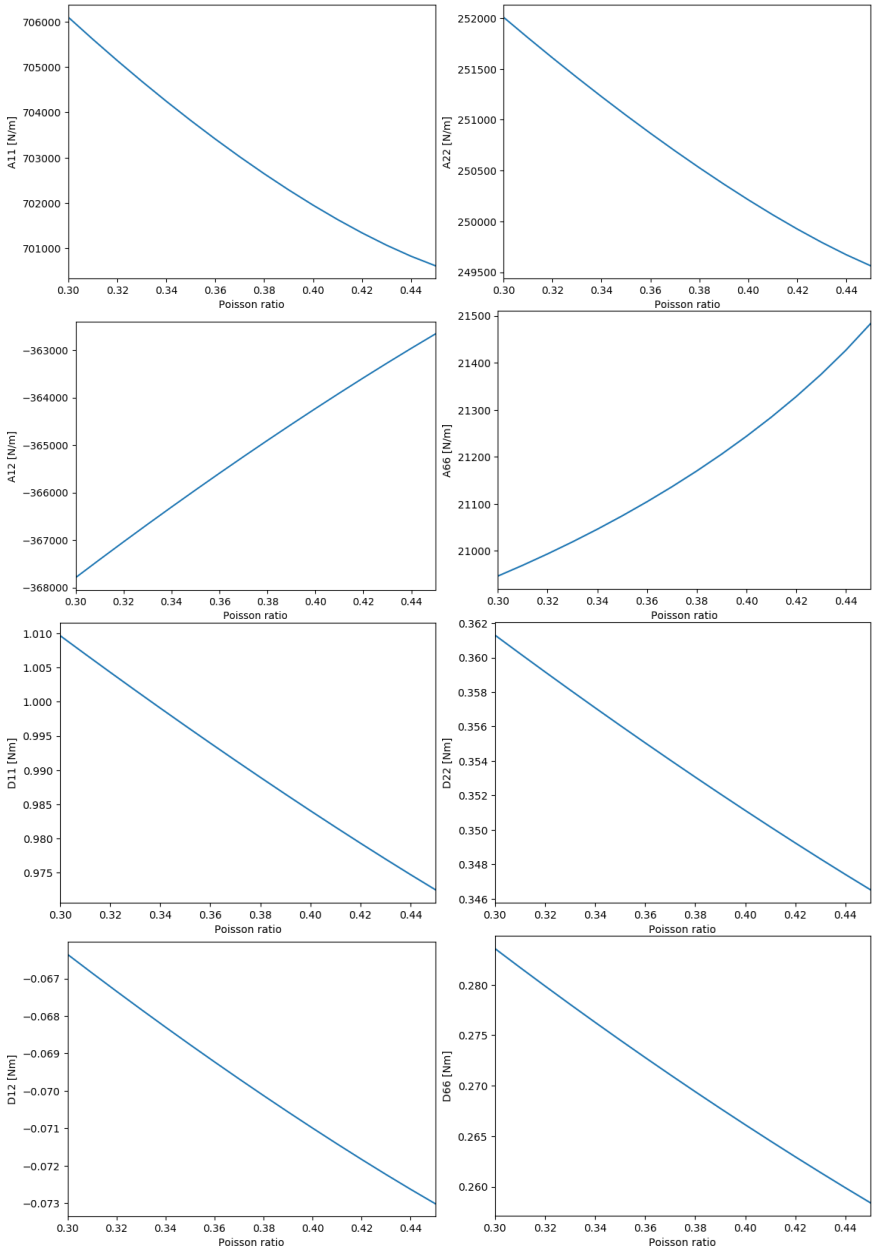

Figure 4.5: Stiffness coefficients with variable Poisson's ratio ν.

	ν				
	0.42	0.4		0.3	
	Value	Value	Percent change	Value	Percent change
A_{11} [N/mm]	701.338	701.950	0.09 %	706.100	0.68 %
A_{22} [N/mm]	249.924	250.212	0.12 %	252.008	0.83 %
A_{12} [N/mm]	−363 586	−364 233	0.18 %	−367 792	1.16 %
A_{66} [N/mm]	21.328	21.244	−0.40 %	20.947	−1.79 %
D_{11} [N mm]	979.327	984.074	0.48 %	1009.675	3.10 %
D_{22} [N mm]	349.237	351.123	0.54 %	361.302	3.45 %
D_{12} [N mm]	−71.833	−70.997	−1.16 %	−66.352	−7.63 %
D_{66} [N mm]	262.957	262.957	1.21 %	283.578	7.84 %

Table 4.2: Difference in stiffness coefficients with different Poisson's ratio ν.

Poisson's ratio found in section 4.1 are approximately correct, while there still might be some uncertainty around the density due to the poor resolution of the scale.

4.2 Measurements from experiments

The values were measured at the middle of each unit cell, for a total of 391 data points. These measured values were taken to be in the z direction, with positive direction upwards. The translation of each point in the x and y directions is assumed to be negligible. The value at the suspension points was subtracted from all data points to obtain the relative displacement in the z direction.

4.2.1 Interpolation of data

For load case 1 and 2, the loads suspended from the plate blocked the laser distance measurer, leading to inability to measure points around those loads. Numpy was used to interpolate values for those points.

4.2.2 Load case 1

In load case 1, the plates were only subjected to gravitational body forces. Figures 4.6 and 4.7 show visualizations of the data points collected from load case 1 on plate 1 and plate 2, respectively.

4.2.3 Load case 2

In load case 2, the plate was subjected to a single load in the middle of the plate. Figure 4.8 shows a visualization of the data points collected from load case 2 on plate 1.

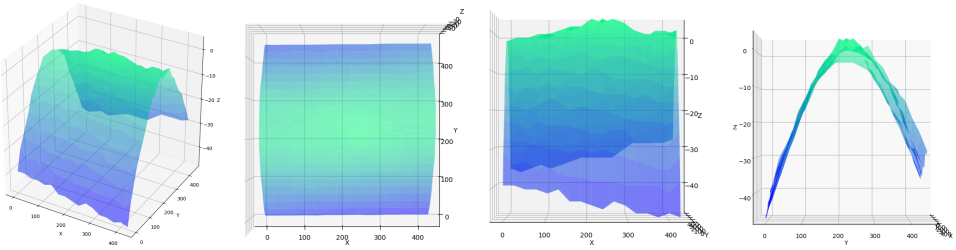

(a) Isometric view. **(b)** XY view. **(c)** XZ view. **(d)** YZ view.

Figure 4.6: Load case 1 on plate 1.

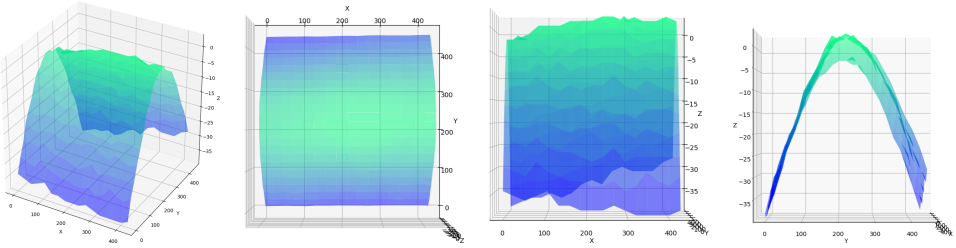

(a) Isometric view. **(b)** XY view. **(c)** XZ view. **(d)** YZ view.

Figure 4.7: Load case 1 on plate 2.

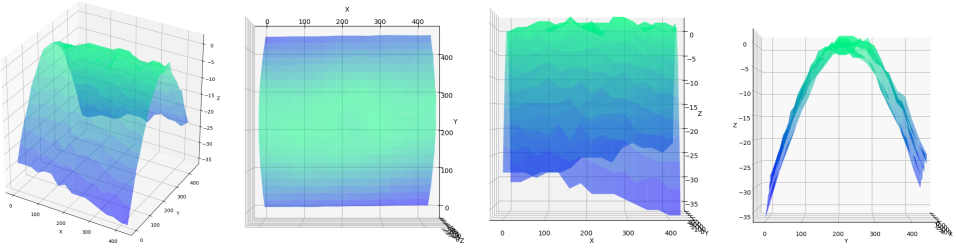

(a) Isometric view. **(b)** XY view. **(c)** XZ view. **(d)** YZ view.

Figure 4.8: Load case 2 on plate 1.

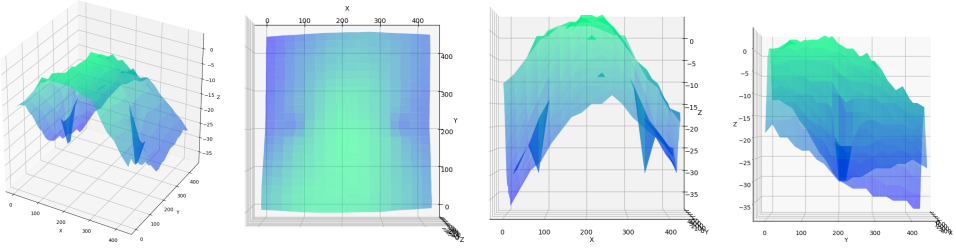

(a) Isometric view. **(b)** XY view. **(c)** XZ view. **(d)** YZ view.

Figure 4.9: Load case 2 on plate 1.

4.2.4 Load case 3

In load case 3, the plate was subjected to two symmetrical loads on the left and right sides in the x direction, and the middle in the y direction, of the plate. Figure 4.9 shows a visualization of the data points collected from load case 3 on plate 2. Here, the interpolated points around the loads have an unrealistically low value, as shown by the two downwards spikes.

4.2.5 Surface fitting

The visualizations of the data points show a quite rugged surface. This can be attributed to inaccuracy in measuring – as mentioned in section 3.3.1, the device used to measure the data points had an accuracy of $\pm 3\,\mathrm{mm}$. In order to smoothen out the surface, Matlab was used for regression analysis. Matlab has multiple surface fitting models, listed in table 4.3. In the case of polynomial models, for `i` and `j`, integers from 1 to 5 are inserted, denoting the degree of x and y in the polynomial, respectively.

Model type	Name in Matlab	Description
Polynomial	`polyij`	Up to 5th degree polynomial
Interpolant	`linearinterp`	Linear interpolation
	`nearestinterp`	Nearest neighbor interpolation
	`cubicinterp`	Cubic spline interpolation
	`biharmonicinterp`	Biharmonic interpolation
	`thinplateinterp`	Thin-plate spline interpolation
Loess	`lowess`	Local linear regression
	`loess`	Local quadratic regression

Table 4.3: Matlab models for surface fitting.

After visual inspection, the loess model using local quadratic regression was deemed to give the best fit. Figures 4.10-4.13 show visualizations of the fitted surfaces, with the measured data points as blue dots. The visualizations were done in Matplotlib, and the deformation in the z direction is exaggerated in the visualizations to better show the shape of the deformed plate – this is the case in all visualizations in this chapter. Load case 3 had the most complex shape and most extreme outliers, and was thus the most interesting specimen for visualization of each model, see appendix A. Here, one can see that polynomial models are too inaccurate, as is the local linear lowess model. Interpolant models are not intended for this type of surface fitting, but visualizations of them are included for completeness.

4.2.6 Discussion

The measured data points are not symmetrical about the middle in the yz plane, contrary to expectations. This can be attributed to device inaccuracy, as well as resolution, the device having a resolution of $1\,\mathrm{mm}$. The points from which the plates were suspended were measured to be at the same height, but due to this inaccuracy they likely were slightly offset from each other, leading to some rigid body motion.

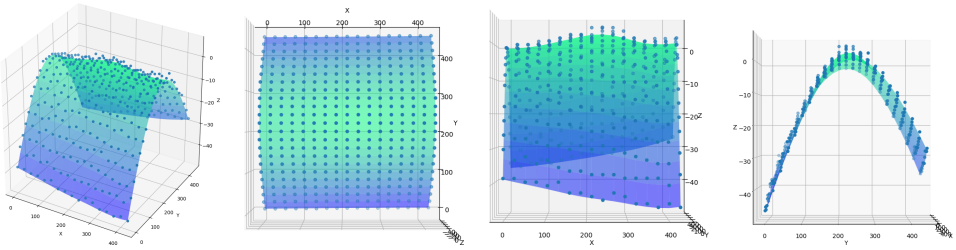

(a) Isometric view. **(b)** XY view. **(c)** XZ view. **(d)** YZ view.

Figure 4.10: Load case 1 on plate 1 fitted with the loess model.

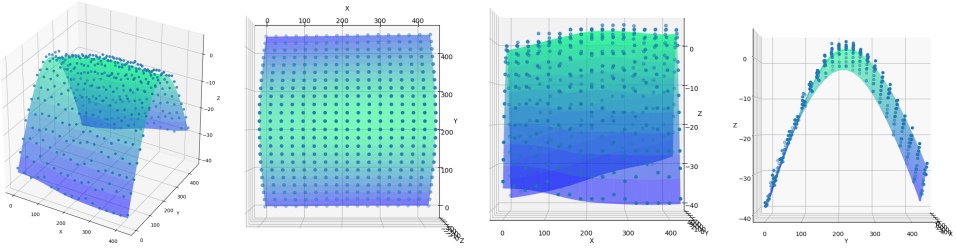

(a) Isometric view. **(b)** XY view. **(c)** XZ view. **(d)** YZ view.

Figure 4.11: Load case 1 on plate 2 fitted with the loess model.

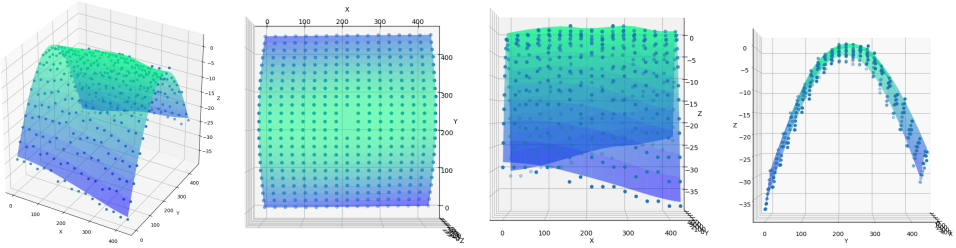

(a) Isometric view. **(b)** XY view. **(c)** XZ view. **(d)** YZ view.

Figure 4.12: Load case 2 on plate 1 fitted with the loess model.

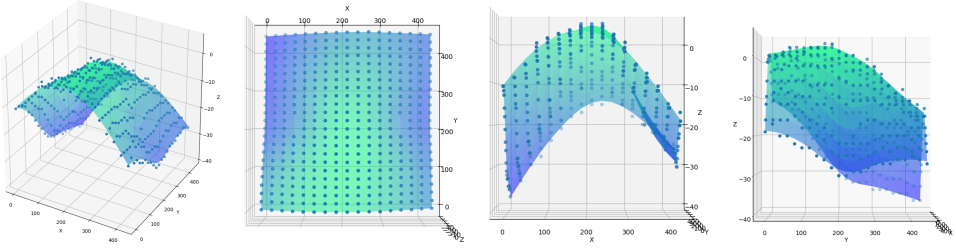

(a) Isometric view. **(b)** XY view. **(c)** XZ view. **(d)** YZ view.

Figure 4.13: Load case 3 on plate 2 fitted with the loess model.

4.3 Simulation

A simulation of the unit cell using the material properties found in section 4.1 yielded the following stiffness matrix components:

$$\begin{aligned}
\mathbf{A} &= \begin{bmatrix} 701.621 & -363.801 & 0 \\ -363.801 & 250.094 & 0 \\ 0 & 0 & 21.345 \end{bmatrix} \mathrm{N/mm} \\
\mathbf{B} &= \mathbf{0} \\
\mathbf{D} &= \begin{bmatrix} 979.335 & -71.898 & 0 \\ -71.898 & 349.458 & 0 \\ 0 & 0 & 263.027 \end{bmatrix} \mathrm{N\,mm}
\end{aligned} \tag{4.5}$$

This was then used to simulate the load cases on a shell model of the same size as the plates. The translation in the z direction was gathered from nodes at the middle of each unit cell. The simulations were then visualized using Matplotlib using those gathered translational values.

4.3.1 Load case 1

Figure 4.14 shows a visualization of the simulated plate. Figure 4.15 shows a comparison between fitted data points on plate 2 in blue-to-green, and the simulation in red-to-yellow.

4.3.2 Load case 2

Figure 4.16 shows a visualization of the simulated plate. Figure 4.17 shows a comparison between fitted data points on the real-life plate in blue-to-green, and the simulation in red-to-yellow.

4.3.3 Load case 3

Figure 4.18 shows a visualization of the simulated plate. Figure 4.19 shows a comparison between fitted data points on the real-life plate in blue-to-green, and the simulation in red-to-yellow.

4.3.4 The effect of NLGEOM

Figure 4.20 shows a comparison between simulations with NLGEOM toggled off in cyan-to-magenta, and with NLGEOM toggled on in red-to-yellow, of load case 3. All other parameters are equal. There is a clear difference between the two, showing the importance of taking geometric nonlinearity into account during calculations with large deformations.

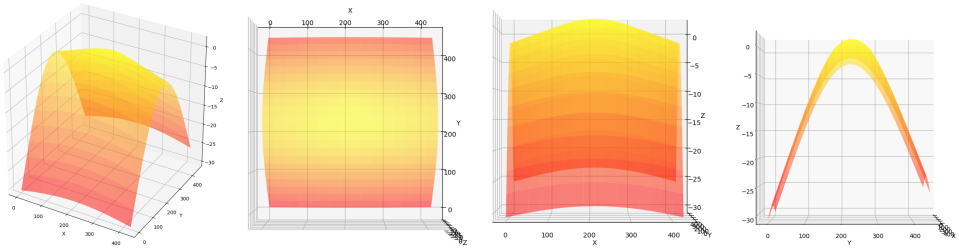

(a) Isometric view. **(b)** XY view. **(c)** XZ view. **(d)** YZ view.

Figure 4.14: Load case 1 simulated.

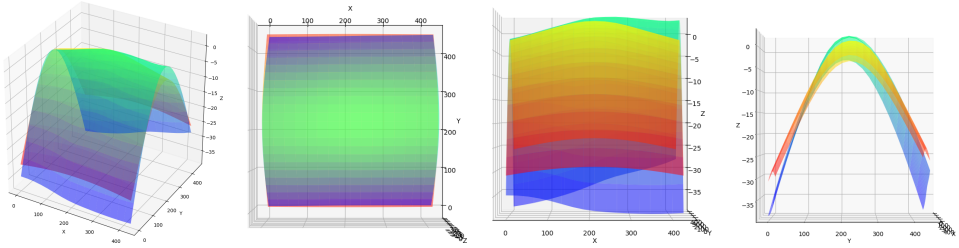

(a) Isometric view. **(b)** XY view. **(c)** XZ view. **(d)** YZ view.

Figure 4.15: Load case 1 comparison between measured data points and simulation.

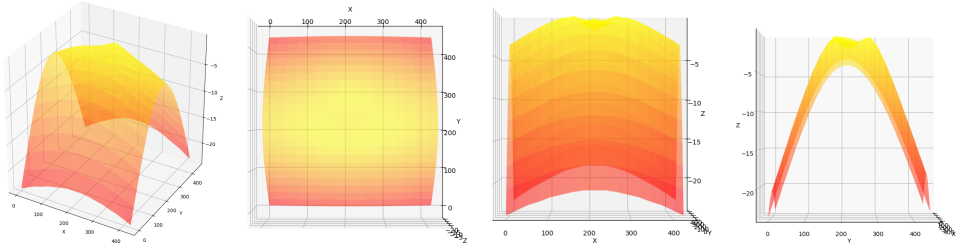

(a) Isometric view. **(b)** XY view. **(c)** XZ view. **(d)** YZ view.

Figure 4.16: Load case 2 simulated.

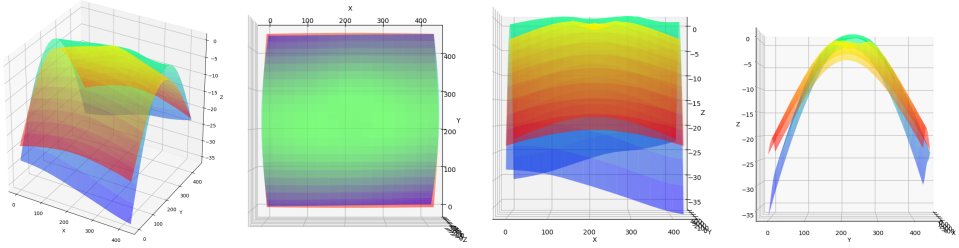

(a) Isometric view. **(b)** XY view. **(c)** XZ view. **(d)** YZ view.

Figure 4.17: Load case 2 comparison between measured data points and simulation.

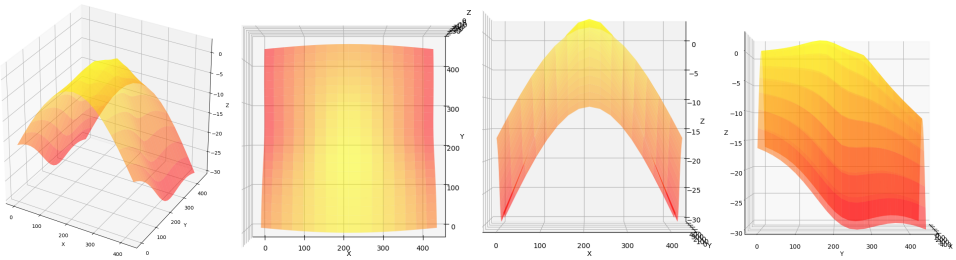

(a) Isometric view. **(b)** XY view. **(c)** XZ view. **(d)** YZ view.

Figure 4.18: Load case 3 simulated.

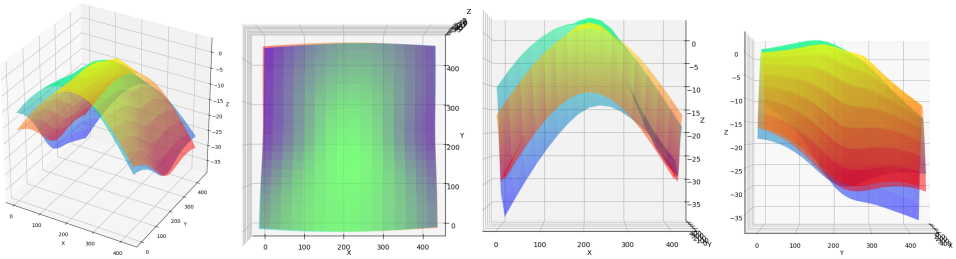

(a) Isometric view. **(b)** XY view. **(c)** XZ view. **(d)** YZ view.

Figure 4.19: Load case 3 comparison between measured data points and simulation.

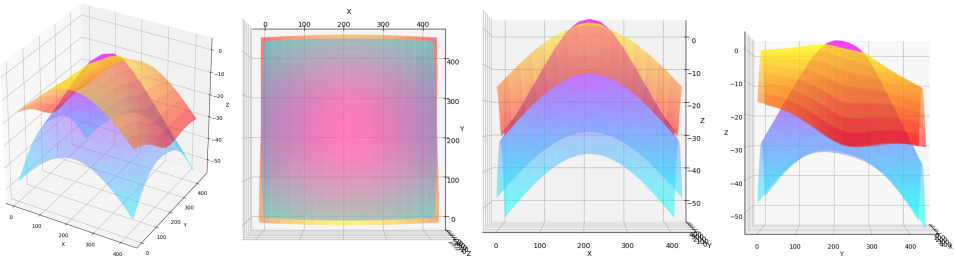

(a) Isometric view. **(b)** XY view. **(c)** XZ view. **(d)** YZ view.

Figure 4.20: Comparison between simulations with and without NLGEOM.

4.3.5 Discussion

When examining the comparisons between the data points and the simulations, their shapes are very similar in every load case, despite the asymmetry of the data points. This shows that the shell deformation method is fairly accurate for analyzing patterned plates. The measured data points do display more deformation in the z direction overall, however. A possible cause of this is inaccuracy in measuring the weight of the plate, so that the density input in the simulation suggests a lighter weight than what the plate actually has. Another cause might lie in the production of the plates. The pattern was cut into the plates using a laser cutter. Due to the heat-intensive nature of the laser, this gives a heat-affected zone, or HAZ, around the cuts. The machine's laser is very concentrated, giving a small HAZ which is insignificant on larger-width cuts. The specimens used for material testing, for example, have a minimum width of $13\,\mathrm{mm}$, see figure 4.1. A HAZ width of $0.5\,\mathrm{mm}$ would amount to $3.8\,\%$ of the width of the specimen, which is likely not significant. The HAZ then would not have a significant effect on the results of material testing. However, the patterned plate's flexures have a narrower width of $3\,\mathrm{mm}$. A HAZ width of $0.5\,\mathrm{mm}$ would then amount to $16.7\,\%$ of the flexure's width. A change in material properties in the HAZ would then have a greater effect on the flexure, and in turn, the patterned plate. The size of the HAZ in the case of this experiment is unknown, but when laser cutting, the HAZ increases with decreased speed of the carriage, as this means heat exposure over a longer amount of time. The effect of the HAZ on the elastic properties of the flexures is also unknown, but might very well give reduced stiffness, leading to the increased deformation in the measured data points in the experiment compared to the simulation of the same plate.

4.4 Comparison of patterns

Simulations were run with different patterns with approximately the same dimensions as the YdX pattern, all with the material properties found for PETG. The cuts were all $0.2\,\mathrm{mm}$ wide, reflecting the kerf of the laser cutter. In addition, a solid plate without a pattern was simulated. The visualizations demonstrate how the differences in the stiffness matrices affect the deformation of the plates.

4.4.1 Solid

Stiffness matrix components

The stiffness matrix components found through simulation were as follows:

$$\begin{aligned}
\mathbf{A} &= \begin{bmatrix} 7576.493 & 3182.127 & 0 \\ 3182.127 & 7576.493 & 0 \\ 0 & 0 & 2197.183 \end{bmatrix} \mathrm{N/mm} \\
\mathbf{B} &= \mathbf{0} \\
\mathbf{D} &= \begin{bmatrix} 5682.370 & 2386.595 & 0 \\ 2386.595 & 5682.370 & 0 \\ 0 & 0 & 1647.887 \end{bmatrix} \mathrm{N\,mm}
\end{aligned} \tag{4.6}$$

Seeing as this is an isotropic solid, these can be verified by putting the found material properties into equation 2.73, which gives the exact same results.

Load case 1

Figure 4.21 shows a visualization of a simulation of load case 1 on a solid plate. Figure 4.22 shows a comparison between the solid plate in cyan-to-magenta, and the YdX cmm plate in red-to-yellow, for load case 1.

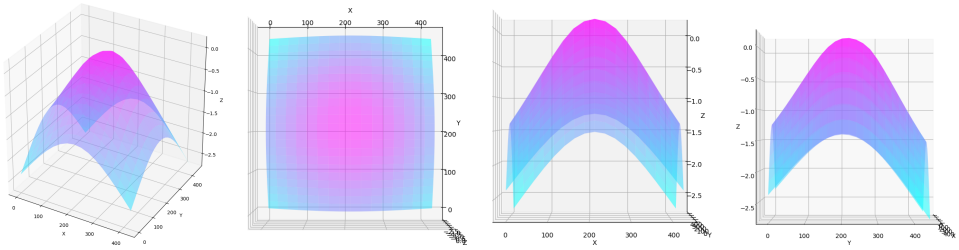

(a) Isometric view. **(b)** XY view. **(c)** XZ view. **(d)** YZ view.

Figure 4.21: Load case 1 on a solid plate.

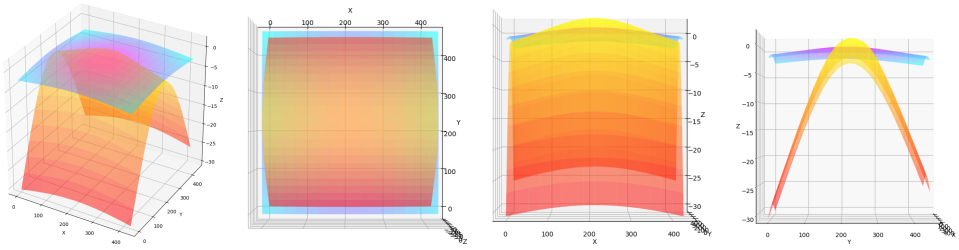

(a) Isometric view. **(b)** XY view. **(c)** XZ view. **(d)** YZ view.

Figure 4.22: Load case 1 comparison between a solid plate and a YdX cmm plate.

Load case 2

Figure 4.23 shows a visualization of a simulation of load case 2 on a solid plate. Figure 4.24 shows a comparison between the solid plate in cyan-to-magenta, and the YdX cmm plate in red-to-yellow, for load case 2.

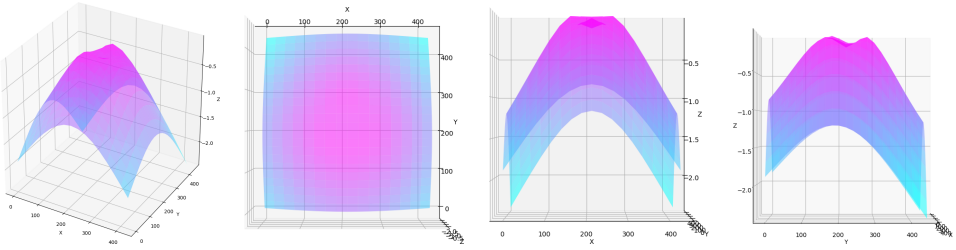

(a) Isometric view. **(b)** XY view. **(c)** XZ view. **(d)** YZ view.

Figure 4.23: Load case 2 on a solid plate.

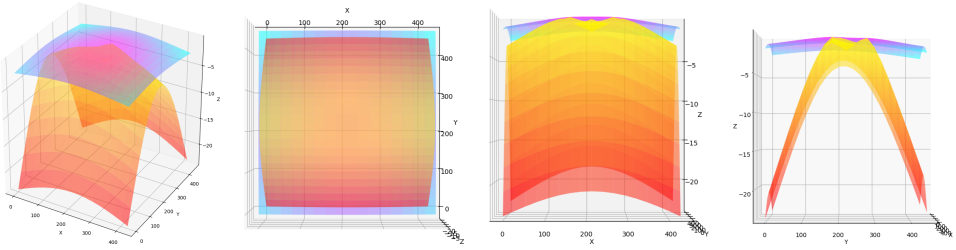

(a) Isometric view. **(b)** XY view. **(c)** XZ view. **(d)** YZ view.

Figure 4.24: Load case 2 comparison between a solid plate and a YdX cmm plate.

Load case 3

Figure 4.25 shows a visualization of a simulation of load case 3 on a solid plate. Figure 4.26 shows a comparison between the solid plate in cyan-to-magenta, and the YdX cmm plate in red-to-yellow, for load case 3.

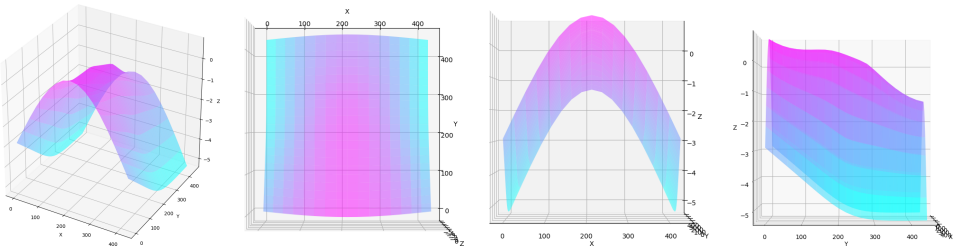

(a) Isometric view. **(b)** XY view. **(c)** XZ view. **(d)** YZ view.

Figure 4.25: Load case 3 on a solid plate.

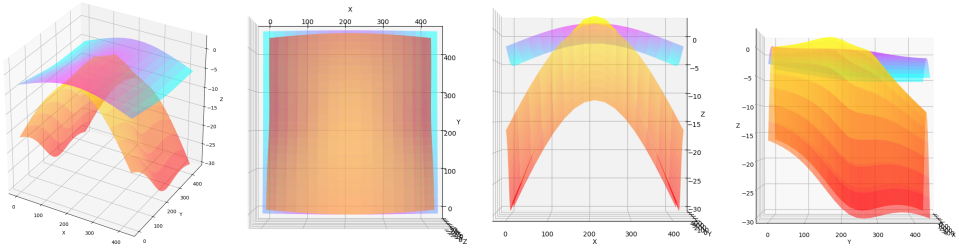

(a) Isometric view. **(b)** XY view. **(c)** XZ view. **(d)** YZ view.

Figure 4.26: Load case 3 comparison between a solid plate and a YdX cmm plate.

Discussion

As suggested by the stiffness matrix, having quite large values, the unpatterned plate is much more stiff than the YdX cmm plate.

The simulated solid plate under load case 1, as seen in figure 4.21, is very similar to the YdX cmm plate under load case 3 simulated with NLGEOM toggled off, as seen in figure 4.20. Deformations must be small in order to not have to take nonlinear geometry into account, which is the case with the former, but not the latter. The similarity in shape thus shows that a simulation with large deformations that does not take nonlinear geometry into account behaves in the same way as a simulation with small deformations.

4.4.2 LET cmm

Dimensions

Figure 4.27 shows an illustration of the simulated LET cmm unit, and table 4.4 shows the measurements of each colored part.

Figure 4.27: LET cmm unit.

Color	Direction	Measurement
Blue	Horizontal	10 mm
Blue	Vertical	3 mm
Red	Horizontal	3 mm

Table 4.4: Measurements for LET cmm unit.

Stiffness matrix components

$$\mathbf{A} = \begin{bmatrix} 5900.134 & 8.917 & 0 \\ 8.917 & 10.323 & 0 \\ 0 & 0 & 166.372 \end{bmatrix} \text{N/mm}$$
$$\mathbf{B} = \mathbf{0} \tag{4.7}$$
$$\mathbf{D} = \begin{bmatrix} 4441.377 & 46.743 & 0 \\ 46.743 & 110.540 & 0 \\ 0 & 0 & 743.221 \end{bmatrix} \text{N mm}$$

Simulation

When attempting to simulate the LET cmm plate, the program returned errors related to the program dividing the simulations into too short time increments. This could be because of difficulty calculating excessive deformation in the simulated plate. Another reason could be the high degree of anisotropy.

4.4.3 LET p4m

Dimensions

Figure 4.28 shows an illustration of the simulated LET p4m unit, and table 4.5 shows the measurements of each colored part.

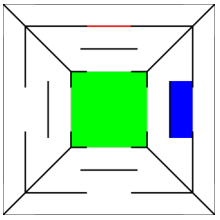

Figure 4.28: LET p4m unit.

Color	Direction	Measurement
Blue	Horizontal	3 mm
Red	Horizontal	6 mm
Green	Horizontal	10 mm

Table 4.5: Measurements for LET p4m unit.

Stiffness matrix components

$$\begin{aligned}
\mathbf{A} &= \begin{bmatrix} 96.941 & 0.556 & 0 \\ 0.556 & 96.727 & 0 \\ 0 & 0 & 37.792 \end{bmatrix} \text{N/mm} \\
\mathbf{B} &= \mathbf{0} \\
\mathbf{D} &= \begin{bmatrix} 412.311 & 15.060 & 0 \\ 15.060 & 412.059 & 0 \\ 0 & 0 & 537.483 \end{bmatrix} \text{N mm}
\end{aligned} \tag{4.8}$$

Load case 1

Figure 4.29 shows a visualization of a simulation of load case 1 on a LET p4m plate. Figure 4.30 shows a comparison between the LET p4m plate in cyan-to-magenta, and the YdX cmm plate in red-to-yellow, for load case 1.

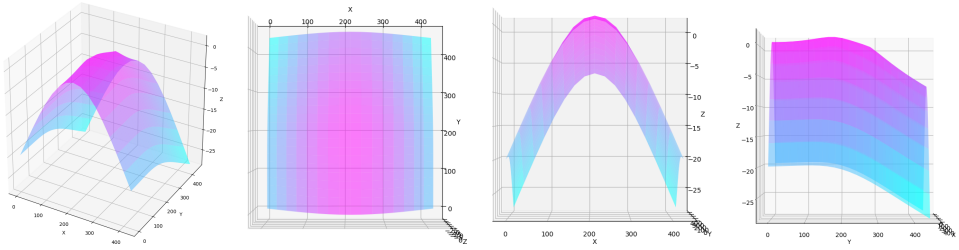

(a) Isometric view. **(b)** XY view. **(c)** XZ view. **(d)** YZ view.

Figure 4.29: Load case 1 on a LET p4m plate.

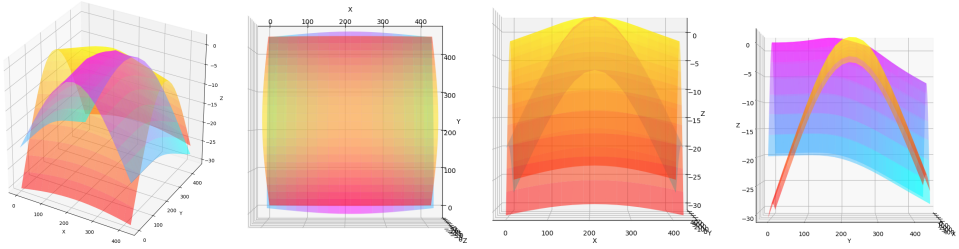

(a) Isometric view. **(b)** XY view. **(c)** XZ view. **(d)** YZ view.

Figure 4.30: Load case 1 comparison between a LET p4m plate and a YdX cmm plate.

Load case 2

Figure 4.31 shows a visualization of a simulation of load case 2 on a LET p4m plate. Figure 4.32 shows a comparison between the LET p4m plate in cyan-to-magenta, and the YdX cmm plate in red-to-yellow, for load case 2.

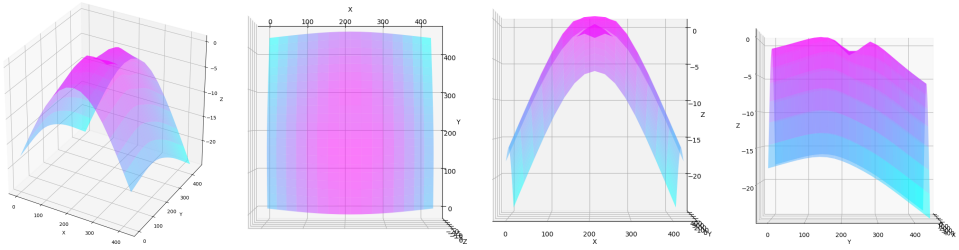

(a) Isometric view. **(b)** XY view. **(c)** XZ view. **(d)** YZ view.

Figure 4.31: Load case 2 on a LET p4m plate.

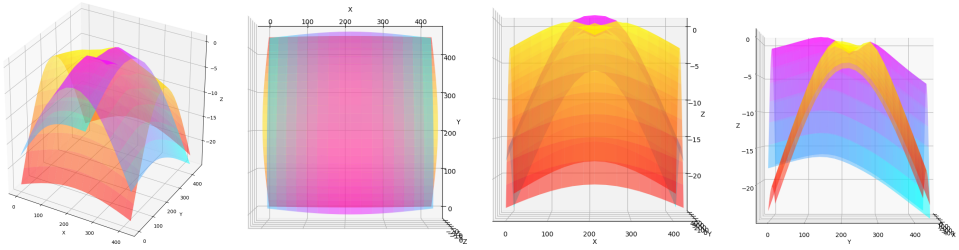

(a) Isometric view. **(b)** XY view. **(c)** XZ view. **(d)** YZ view.

Figure 4.32: Load case 2 comparison between a LET p4m plate and a YdX cmm plate.

Load case 3

Figure 4.33 shows a visualization of a simulation of load case 3 on a LET p4m plate. Figure 4.34 shows a comparison between the LET p4m plate in cyan-to-magenta, and the YdX cmm plate in red-to-yellow, for load case 3.

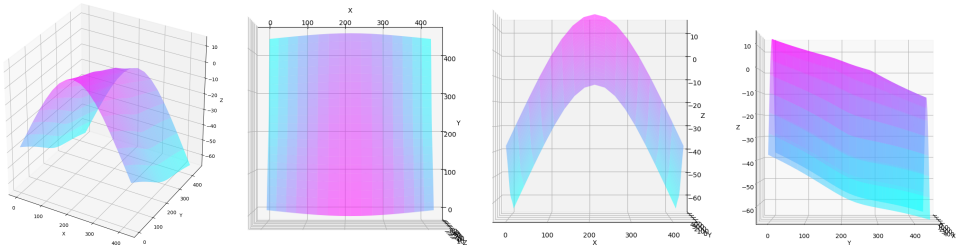

(a) Isometric view. **(b)** XY view. **(c)** XZ view. **(d)** YZ view.

Figure 4.33: Load case 3 on a LET p4m plate.

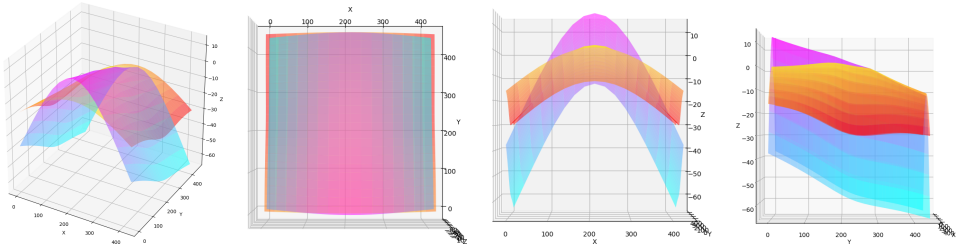

(a) Isometric view. **(b)** XY view. **(c)** XZ view. **(d)** YZ view.

Figure 4.34: Load case 3 comparison between a LET p4m plate and a YdX cmm plate.

4.4.4 Coil cmm

Dimensions

Figure 4.35 shows an illustration of the simulated coil cmm unit, and table 4.6 shows the measurements of each colored part.

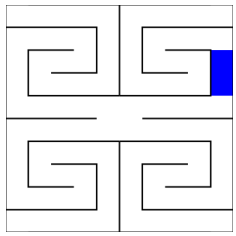

Figure 4.35: Coil cmm unit.

Color	Direction	Measurement
Blue	Vertical	3 mm

Table 4.6: Measurements for coil cmm unit.

Stiffness matrix components

$$\begin{aligned}
\mathbf{A} &= \begin{bmatrix} 9.794 & -0.343 & 0 \\ -0.343 & 10.792 & 0 \\ 0 & 0 & 4.951 \end{bmatrix} \text{N/mm} \\
\mathbf{B} &= \mathbf{0} \\
\mathbf{D} &= \begin{bmatrix} 167.371 & 2.191 & 0 \\ 2.191 & 138.226 & 0 \\ 0 & 0 & 76.039 \end{bmatrix} \text{N mm}
\end{aligned} \tag{4.9}$$

Load case 1

Figure 4.36 shows a visualization of a simulation of load case 1 on a coil cmm plate. Figure 4.37 shows a comparison between the coil cmm plate in cyan-to-magenta, and the YdX cmm plate in red-to-yellow, for load case 1.

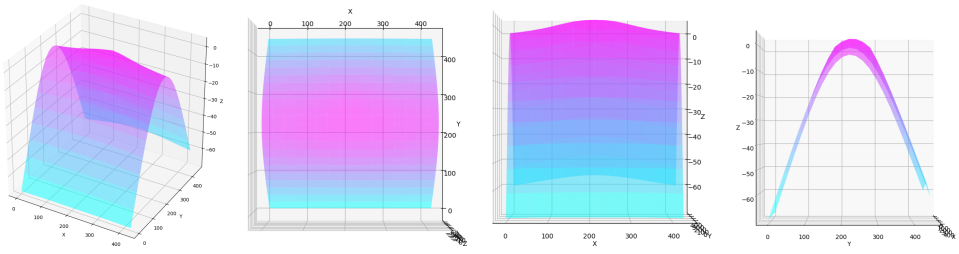

(a) Isometric view. **(b)** XY view. **(c)** XZ view. **(d)** YZ view.

Figure 4.36: Load case 1 on a coil cmm plate.

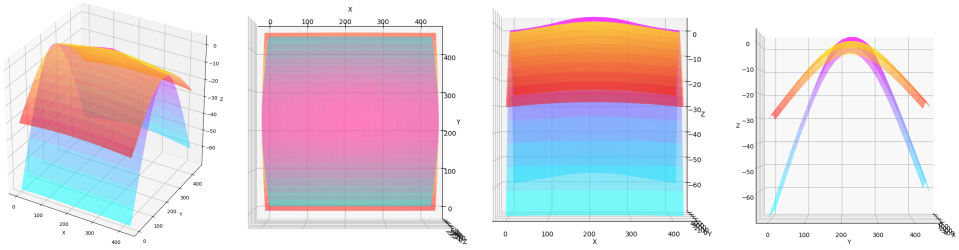

(a) Isometric view. **(b)** XY view. **(c)** XZ view. **(d)** YZ view.

Figure 4.37: Load case 1 comparison between a coil cmm plate and a YdX cmm plate.

Load case 2

Figure 4.38 shows a visualization of a simulation of load case 2 on a coil cmm plate. Figure 4.39 shows a comparison between the coil cmm plate in cyan-to-magenta, and the YdX cmm plate in red-to-yellow, for load case 2.

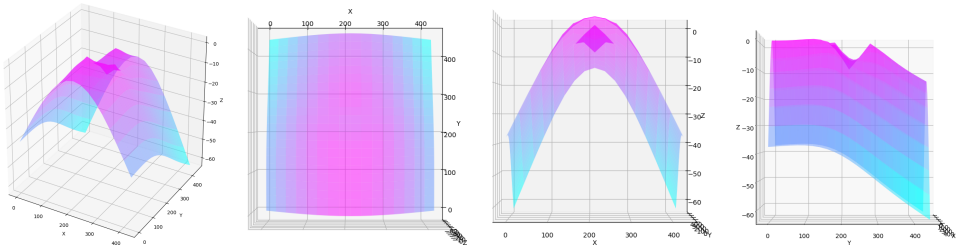

(a) Isometric view. **(b)** XY view. **(c)** XZ view. **(d)** YZ view.

Figure 4.38: Load case 2 on a coil cmm plate.

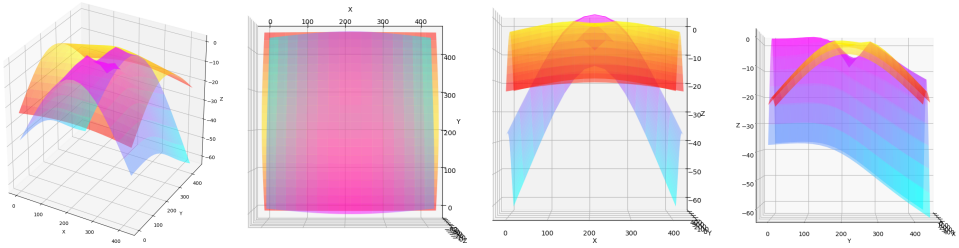

(a) Isometric view. **(b)** XY view. **(c)** XZ view. **(d)** YZ view.

Figure 4.39: Load case 2 comparison between a coil cmm plate and a YdX cmm plate.

Load case 3

Figure 4.40 shows a visualization of a simulation of load case 3 on a coil cmm plate. Figure 4.41 shows a comparison between the coil cmm plate in cyan-to-magenta, and the

YdX cmm plate in red-to-yellow, for load case 3.

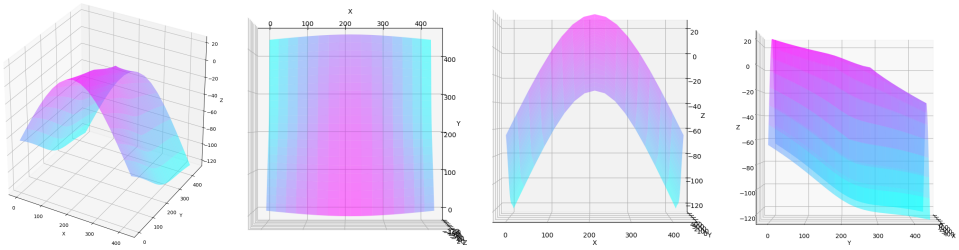

(a) Isometric view. **(b)** XY view. **(c)** XZ view. **(d)** YZ view.

Figure 4.40: Load case 3 on a coil cmm plate.

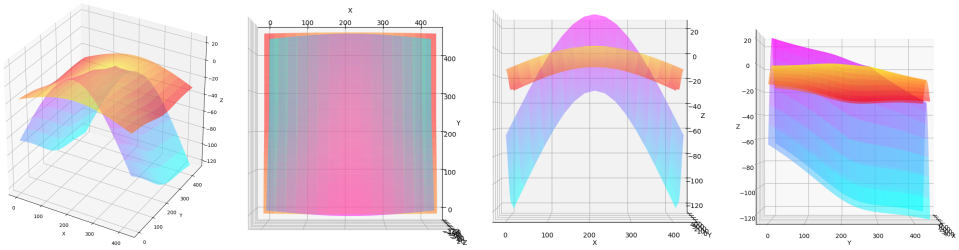

(a) Isometric view. **(b)** XY view. **(c)** XZ view. **(d)** YZ view.

Figure 4.41: Load case 3 comparison between a LET p4m plate and a YdX cmm plate.

4.4.5 Coil p4

Dimensions

Figure 4.42 shows an illustration of the simulated coil p4 unit, and table 4.7 shows the measurements of each colored part.

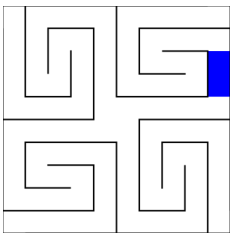

Figure 4.42: Coil p4 unit.

Color	Direction	Measurement
Blue	Vertical	3 mm

Table 4.7: Measurements for coil p4 unit.

Stiffness matrix components

$$\begin{aligned}
\mathbf{A} &= \begin{bmatrix} 10.315 & -0.394 & 0 \\ -0.394 & 10.320 & 0 \\ 0 & 0 & 4.949 \end{bmatrix} \mathrm{N/mm} \\
\mathbf{B} &= \mathbf{0} \\
\mathbf{D} &= \begin{bmatrix} 153.051 & 2.423 & 0 \\ 2.423 & 153.051 & 0 \\ 0 & 0 & 75.679 \end{bmatrix} \mathrm{N\,mm}
\end{aligned} \tag{4.10}$$

Load case 1

Figure 4.43 shows a visualization of a simulation of load case 1 on a coil p4 plate. Figure 4.44 shows a comparison between the coil p4 plate in cyan-to-magenta, and the YdX cmm plate in red-to-yellow, for load case 1.

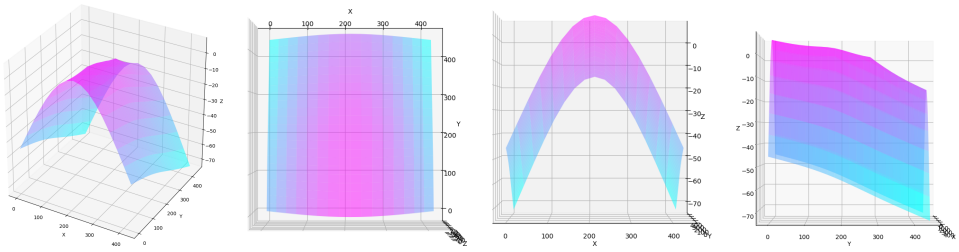

(a) Isometric view. **(b)** XY view. **(c)** XZ view. **(d)** YZ view.

Figure 4.43: Load case 1 on a coil p4 plate.

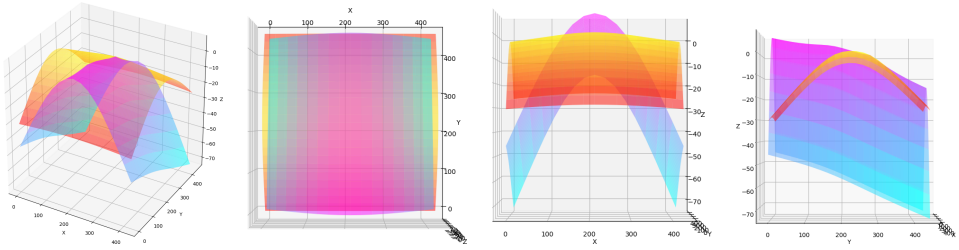

(a) Isometric view. **(b)** XY view. **(c)** XZ view. **(d)** YZ view.

Figure 4.44: Load case 1 comparison between a coil p4 plate and a YdX cmm plate.

Load case 2

Figure 4.45 shows a visualization of a simulation of load case 2 on a coil p4 plate. Figure 4.46 shows a comparison between the coil p4 plate in cyan-to-magenta, and the YdX cmm plate in red-to-yellow, for load case 2.

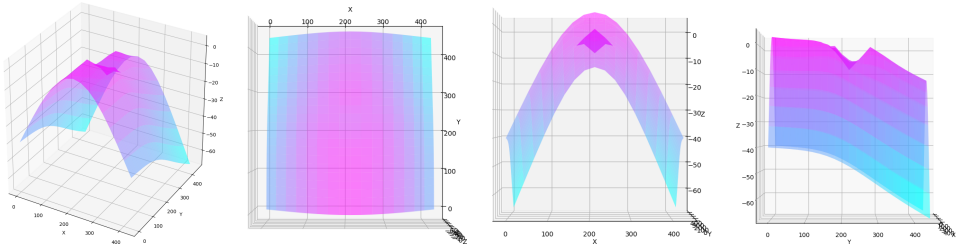

(a) Isometric view. **(b)** XY view. **(c)** XZ view. **(d)** YZ view.

Figure 4.45: Load case 2 on a coil p4 plate.

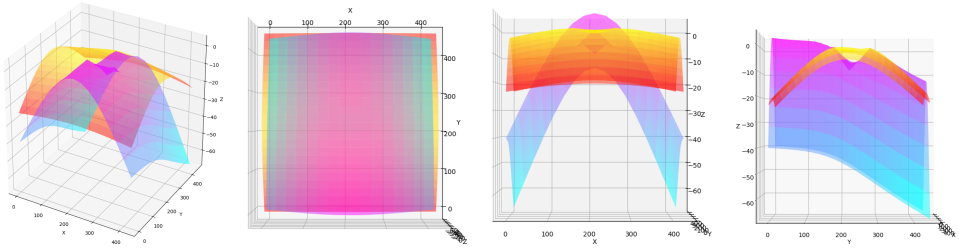

(a) Isometric view. **(b)** XY view. **(c)** XZ view. **(d)** YZ view.

Figure 4.46: Load case 2 comparison between a coil p4 plate and a YdX cmm plate.

Load case 3

Figure 4.47 shows a visualization of a simulation of load case 3 on a coil p4 plate. Figure 4.48 shows a comparison between the coil p4 plate in cyan-to-magenta, and the YdX cmm plate in red-to-yellow, for load case 3.

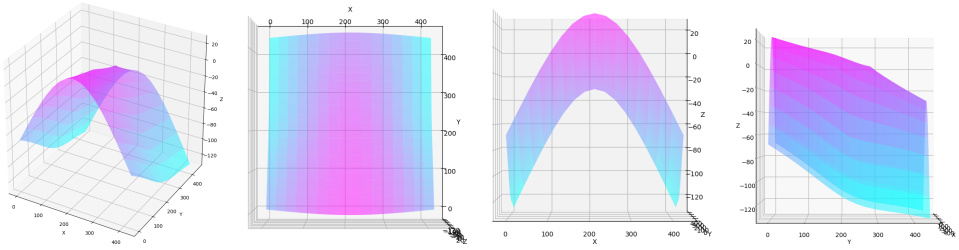

(a) Isometric view. **(b)** XY view. **(c)** XZ view. **(d)** YZ view.

Figure 4.47: Load case 3 on a coil p4 plate.

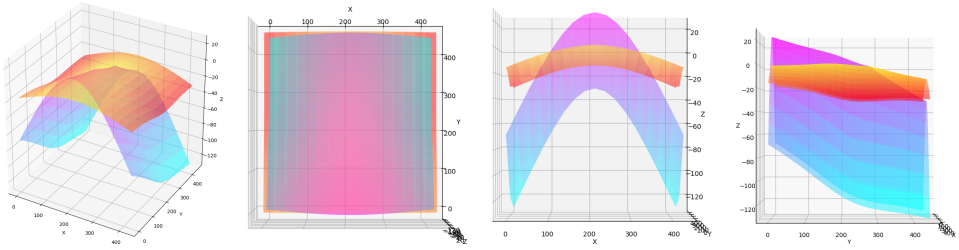

(a) Isometric view. **(b)** XY view. **(c)** XZ view. **(d)** YZ view.

Figure 4.48: Load case 3 comparison between a coil p4 plate and a YdX cmm plate.

4.4.6 Switchback cmm

Dimensions

Figure 4.49 shows an illustration of the simulated switchback cmm unit, and table 4.8 shows the measurements of each colored part.

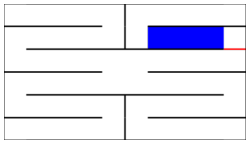

Figure 4.49: Switchback cmm unit.

Color	Direction	Measurement
Blue	Horizontal	10 mm
Blue	Vertical	3 mm
Red	Horizontal	3 mm

Table 4.8: Measurements for switchback cmm unit.

Stiffness matrix components

$$\mathbf{A} = \begin{bmatrix} 76.915 & -1.302 & 0 \\ -1.302 & 10.113 & 0 \\ 0 & 0 & 13.209 \end{bmatrix} \text{N/mm}$$
$$\mathbf{B} = \mathbf{0} \tag{4.11}$$
$$\mathbf{D} = \begin{bmatrix} 526.455 & 5.874 & 0 \\ 5.874 & 115.293 & 0 \\ 0 & 0 & 127.953 \end{bmatrix} \text{N mm}$$

Load case 1

Figure 4.50 shows a visualization of a simulation of load case 1 on a switchback cmm plate. Figure 4.51 shows a comparison between the switchback cmm plate in cyan-to-magenta, and the YdX cmm plate in red-to-yellow, for load case 1.

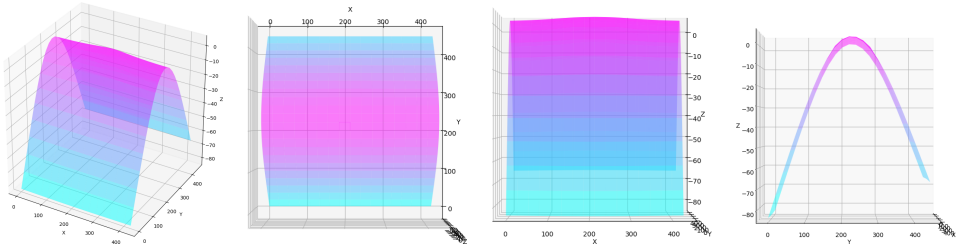

(a) Isometric view. **(b)** XY view. **(c)** XZ view. **(d)** YZ view.

Figure 4.50: Load case 1 on a switchback cmm plate.

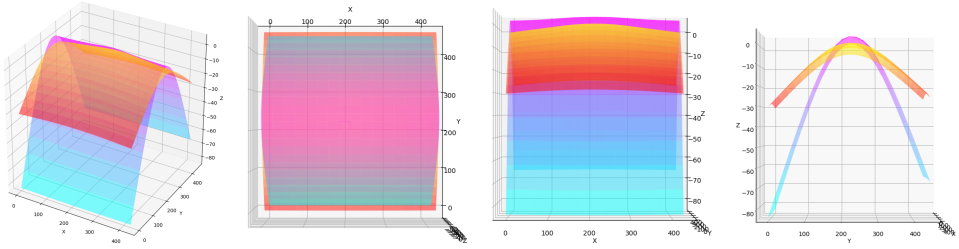

(a) Isometric view. **(b)** XY view. **(c)** XZ view. **(d)** YZ view.

Figure 4.51: Load case 1 comparison between a switchback cmm plate and a YdX cmm plate.

Load case 2

Figure 4.52 shows a visualization of a simulation of load case 2 on a switchback cmm plate. Figure 4.53 shows a comparison between the switchback cmm plate in cyan-to-magenta, and the YdX cmm plate in red-to-yellow, for load case 2.

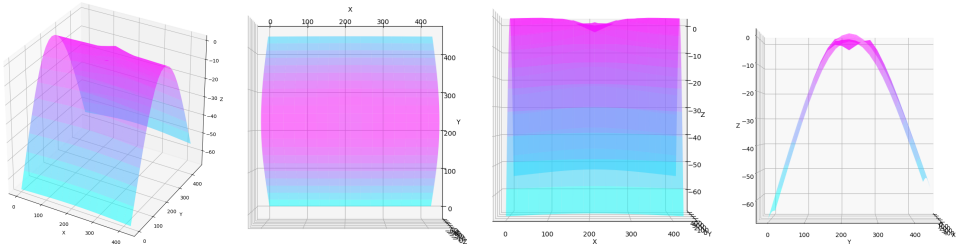

(a) Isometric view. **(b)** XY view. **(c)** XZ view. **(d)** YZ view.

Figure 4.52: Load case 2 on a switchback cmm plate.

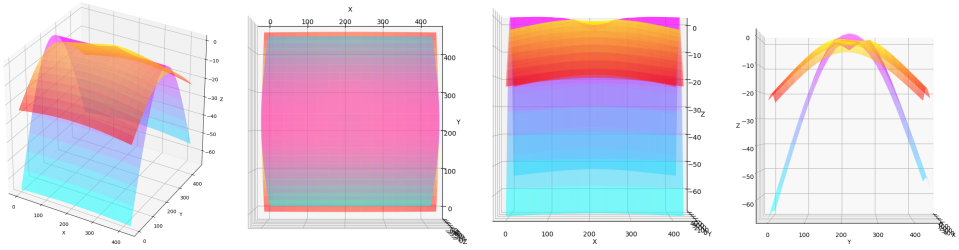

(a) Isometric view. **(b)** XY view. **(c)** XZ view. **(d)** YZ view.

Figure 4.53: Load case 2 comparison between a switchback cmm plate and a YdX cmm plate.

Load case 3

Figure 4.54 shows a visualization of a simulation of load case 3 on a switchback cmm plate. Figure 4.55 shows a comparison between the switchback cmm plate in cyan-to-magenta, and the YdX cmm plate in red-to-yellow, for load case 3.

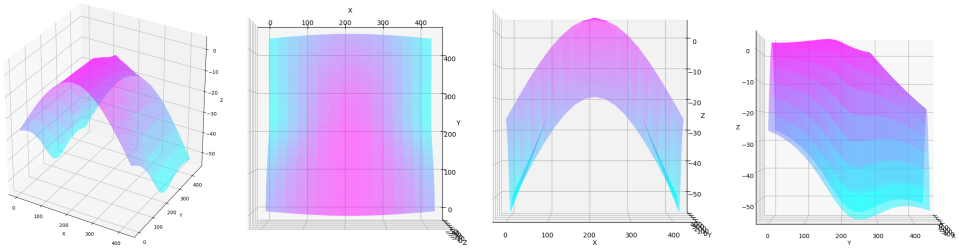

(a) Isometric view. **(b)** XY view. **(c)** XZ view. **(d)** YZ view.

Figure 4.54: Load case 3 on a switchback cmm plate.

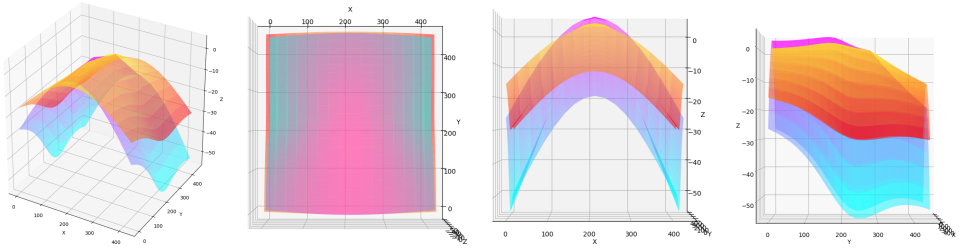

(a) Isometric view. **(b)** XY view. **(c)** XZ view. **(d)** YZ view.

Figure 4.55: Load case 3 comparison between a switchback cmm plate and a YdX cmm plate.

4.4.7 Switchback p4g

Dimensions

Figure 4.56 shows an illustration of the simulated switchback p4g unit, and table 4.9 shows the measurements of each colored part.

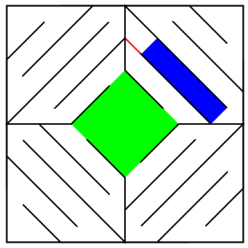

Figure 4.56: Switchback p4g unit.

Color	Direction	Measurement
Blue	Short side	3 mm
Red	Long side	3 mm
Green	Diagonal	10 mm

Table 4.9: Measurements for switchback p4g unit.

Stiffness matrix components

$$\begin{aligned}
\mathbf{A} &= \begin{bmatrix} 11.063 & -4.129 & 0 \\ -4.129 & 11.051 & 0 \\ 0 & 0 & 3.447 \end{bmatrix} \text{N/mm} \\
\mathbf{B} &= \mathbf{0} \\
\mathbf{D} &= \begin{bmatrix} 164.200 & -31.147 & 0 \\ -31.147 & 164.203 & 0 \\ 0 & 0 & 64.996 \end{bmatrix} \text{N mm}
\end{aligned} \tag{4.12}$$

Load case 1

Figure 4.57 shows a visualization of a simulation of load case 1 on a switchback p4g plate. Figure 4.58 shows a comparison between the switchback p4g plate in cyan-to-magenta, and the YdX cmm plate in red-to-yellow, for load case 1.

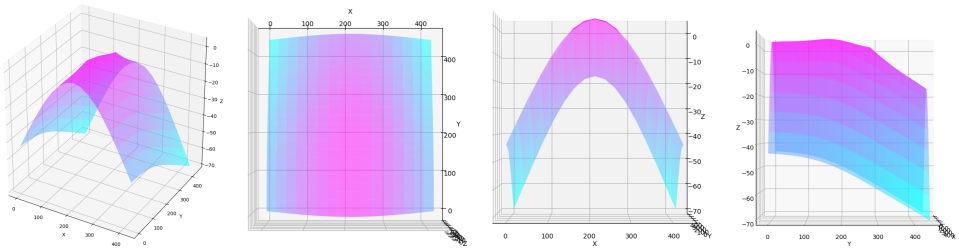

(a) Isometric view. **(b)** XY view. **(c)** XZ view. **(d)** YZ view.

Figure 4.57: Load case 1 on a switchback p4g plate.

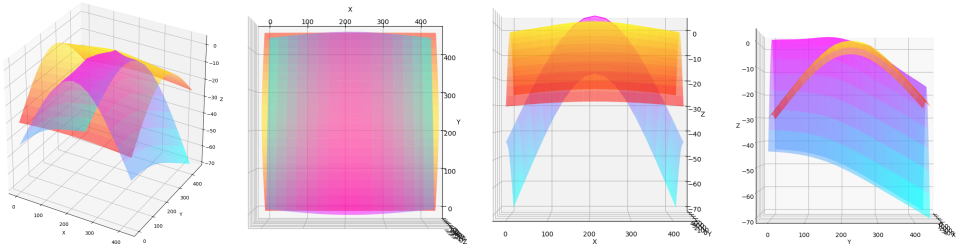

(a) Isometric view. **(b)** XY view. **(c)** XZ view. **(d)** YZ view.

Figure 4.58: Load case 1 comparison between a switchback p4g plate and a YdX cmm plate.

Load case 2

Figure 4.59 shows a visualization of a simulation of load case 2 on a switchback p4g plate. Figure 4.60 shows a comparison between the switchback p4g plate in cyan-to-magenta, and the YdX cmm plate in red-to-yellow, for load case 2.

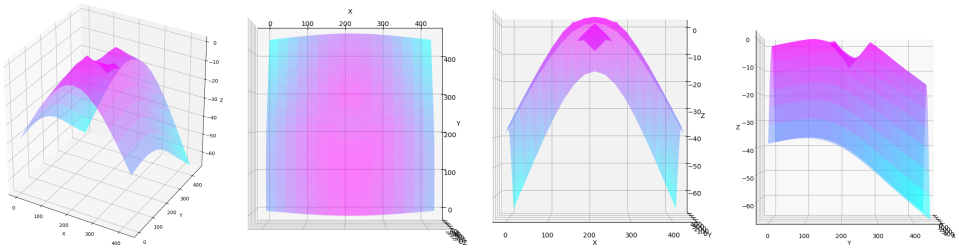

(a) Isometric view. **(b)** XY view. **(c)** XZ view. **(d)** YZ view.

Figure 4.59: Load case 2 on a switchback p4g plate.

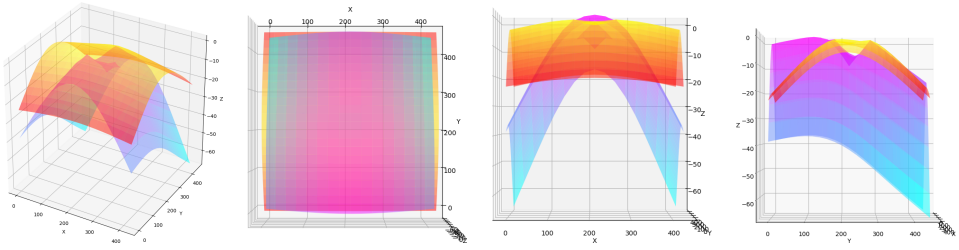

(a) Isometric view. **(b)** XY view. **(c)** XZ view. **(d)** YZ view.

Figure 4.60: Load case 2 comparison between a switchback p4g plate and a YdX cmm plate.

Load case 3

Figure 4.61 shows a visualization of a simulation of load case 3 on a switchback p4g plate. Figure 4.62 shows a comparison between the switchback p4g plate in cyan-to-magenta,

and the YdX cmm plate in red-to-yellow, for load case 3.

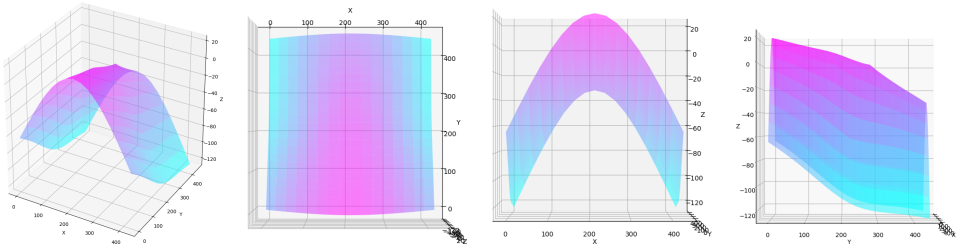

(a) Isometric view. **(b)** XY view. **(c)** XZ view. **(d)** YZ view.

Figure 4.61: Load case 3 on a switchback p4g plate.

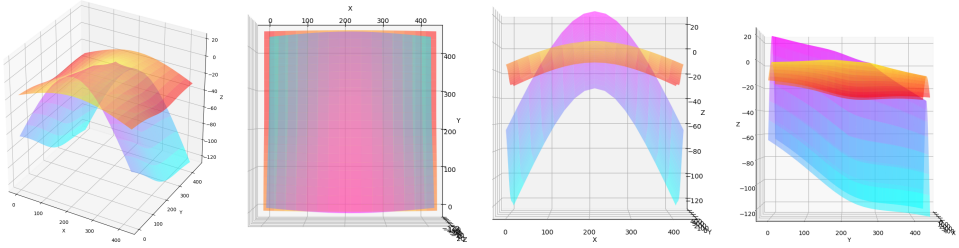

(a) Isometric view. **(b)** XY view. **(c)** XZ view. **(d)** YZ view.

Figure 4.62: Load case 3 comparison between a switchback p4g plate and a YdX cmm plate.

4.4.8 Discussion

Overall, the results in this section shows that different patterns can give very different elastic properties to a plate, even with similar parameters.

4.5 Impact of material properties

As mentioned in section 4.1, the stiffness matrix has a linear relationship with Young's modulus for the material, but not with its Poisson's ratio. The stiffness matrices found earlier in this chapter were all for a Poisson's ratio of $\nu = 0.42$. A Poisson's ratio of $\nu = 0.378$ then represents a $10\,\%$ decrease, and $\nu = 0.462$ a $10\,\%$ increase in Poisson's ratio. Table 4.10 shows the percent change in each stiffness coefficient for the simulated patterns, as well as the sign of the coefficient.

Pattern	ν		Sign
	0.378	0.462	
Solid	$-3.91\,\%$	$4.71\,\%$	+
LET p4m	$-0.73\,\%$	$0.94\,\%$	+
Coil cmm	$-0.21\,\%$	$0.28\,\%$	+
Coil p4	$-0.28\,\%$	$0.37\,\%$	+
SB cmm	$-0.21\,\%$	$0.26\,\%$	+
SB p4g	$-0.63\,\%$	$0.83\,\%$	+
YdX cmm	$0.19\,\%$	$-0.12\,\%$	+

(a) A_{11}

Pattern	ν		Sign
	0.378	0.462	
Solid	$-3.91\,\%$	$4.71\,\%$	+
LET p4m	$-0.71\,\%$	$0.90\,\%$	+
Coil cmm	$-0.36\,\%$	$0.48\,\%$	+
Coil p4	$-0.28\,\%$	$0.38\,\%$	+
SB cmm	$-0.55\,\%$	$0.68\,\%$	+
SB p4g	$-0.62\,\%$	$0.80\,\%$	+
YdX cmm	$0.25\,\%$	$-0.17\,\%$	+

(b) A_{22}

Pattern	ν		Sign
	0.378	0.462	
Solid	$-13.52\,\%$	$15.18\,\%$	+
LET p4m	$-12.15\,\%$	$12.71\,\%$	+
Coil cmm	$0.28\,\%$	$-0.53\,\%$	-
Coil p4	$-0.10\,\%$	$0.32\,\%$	-
SB cmm	$1.28\,\%$	$-1.51\,\%$	-
SB p4g	$-0.24\,\%$	$0.32\,\%$	-
YdX cmm	$0.37\,\%$	$-0.33\,\%$	-

(c) A_{12}

Pattern	ν		Sign
	0.378	0.462	
Solid	$3.05\,\%$	$-2.87\,\%$	+
LET p4m	$-0.69\,\%$	$0.93\,\%$	+
Coil cmm	$-0.29\,\%$	$0.39\,\%$	+
Coil p4	$-0.27\,\%$	$0.36\,\%$	+
SB cmm	$-0.41\,\%$	$0.51\,\%$	+
SB p4g	$-0.84\,\%$	$1.09\,\%$	+
YdX cmm	$-0.78\,\%$	$1.11\,\%$	+

(d) A_{66}

Pattern	ν		Sign
	0.378	0.462	
Solid	$-3.91\,\%$	$4.71\,\%$	+
LET p4m	$1.65\,\%$	$-1.50\,\%$	+
Coil cmm	$1.06\,\%$	$-1.01\,\%$	+
Coil p4	$1.52\,\%$	$-1.43\,\%$	+
SB cmm	$0.21\,\%$	$-0.18\,\%$	+
SB p4g	$1.25\,\%$	$-1.16\,\%$	+
YdX cmm	$1.04\,\%$	$-0.96\,\%$	+

(e) D_{11}

Pattern	ν		Sign
	0.378	0.462	
Solid	$-3.91\,\%$	$4.71\,\%$	+
LET p4m	$1.66\,\%$	$-1.51\,\%$	+
Coil cmm	$2.07\,\%$	$-1.94\,\%$	+
Coil p4	$1.52\,\%$	$-1.43\,\%$	+
SB cmm	$2.52\,\%$	$-2.36\,\%$	+
SB p4g	$1.25\,\%$	$-1.17\,\%$	+
YdX cmm	$1.14\,\%$	$-1.06\,\%$	+

(f) D_{22}

Pattern	ν		Sign
	0.378	0.462	
Solid	$-13.52\,\%$	$13.18\,\%$	+
LET p4m	$-6.74\,\%$	$6.44\,\%$	+
Coil cmm	$-6.83\,\%$	$6.44\,\%$	+
Coil p4	$-6.51\,\%$	$6.24\,\%$	+
SB cmm	$-7.28\,\%$	$7.10\,\%$	+
SB p4g	$-3.12\,\%$	$2.94\,\%$	-
YdX cmm	$-2.52\,\%$	$2.29\,\%$	-

(g) D_{12}

Pattern	ν		Sign
	0.378	0.462	
Solid	$3.05\,\%$	$-2.87\,\%$	+
LET p4m	$2.10\,\%$	$-1.98\,\%$	+
Coil cmm	$1.59\,\%$	$-1.50\,\%$	+
Coil p4	$1.60\,\%$	$-1.51\,\%$	+
SB cmm	$1.83\,\%$	$-1.71\,\%$	+
SB p4g	$2.46\,\%$	$-2.30\,\%$	+
YdX cmm	$2.58\,\%$	$-2.40\,\%$	+

(h) D_{66}

Table 4.10: Change in stiffness coefficient with change in Poisson's ratio.

4.5.1 Discussion

Observations

- For the solid plate, all coefficients increase with increasing ν, apart from A_{66} and D_{66}, which decrease.
- A_{11} and A_{22} increase with increasing ν for all tested patterns except YdX cmm, for which they decrease.
- A_{12} decreases with increasing ν for all tested cmm patterns and increases for all other tested patterns.
- A_{66} decreased with increasing ν for all tested patterns, which is directly opposite to the behavior of a solid plate.
- D_{11} and D_{22} decrease with increasing ν for all tested patterns, which is directly opposite to the behavior of a solid plate.
- D_{12} increases and D_{66} decreases with increasing ν for all tested patterns, which is the same behavior as that of a solid plate.
- There does not seem to be a correlation between the sign of the coefficient and whether it increases or decreases with increasing ν.

Verification

The results can be verified by checking the formulae for the stiffness coefficients of an isotropic material (see equation 2.73) against the solid plate. The equation for percent change is:

$$\frac{\text{new value}}{\text{old value}} - 1 \tag{4.13}$$

For A_{11} and A_{22}, when $\nu_1 = 1.1\nu_0$ (i.e. a $10\,\%$ increase):

$$\begin{aligned} \frac{A_{11,1}}{A_{11,0}} - 1 &= \frac{\frac{Eh}{1-(1.1\nu_0)^2}}{\frac{Eh}{1-\nu_0^2}} - 1 = \frac{1-\nu_0^2}{1-1.21\nu_0^2} - 1 \\ &= \frac{1-0.42^2}{1-1.21(0.42^2)} - 1 = 4.71\,\% \end{aligned} \tag{4.14}$$

For A_{12}:

$$\begin{aligned} \frac{A_{12,1}}{A_{12,0}} - 1 &= \frac{\frac{E(1.1\nu_0)h}{1-(1.1\nu_0)^2}}{\frac{E\nu_0 h}{1-\nu_0^2}} - 1 = \frac{1.1(1-\nu_0^2)}{1-1.21\nu_0^2} - 1 \\ &= \frac{1.1(1-0.42^2)}{1-1.21(0.42^2)} - 1 = 15.18\,\% \end{aligned} \tag{4.15}$$

For A_{66}:

$$\begin{aligned}\frac{A_{66,1}}{A_{66,0}} - 1 &= \frac{\frac{E(1-1.1\nu_0)h}{2(1-(1.1\nu_0)^2)}}{\frac{E(1-\nu_0)h}{2(1-\nu_0^2)}} - 1 = \frac{(1-1.1\nu_0)(1-\nu_0^2)}{(1-\nu_0)(1-1.21\nu_0^2)} - 1 \\ &= \frac{(1-1.1(0.42))(1-0.42^2)}{(1-0.42)(1-1.21(0.42^2))} - 1 = -2.87\,\%\end{aligned} \tag{4.16}$$

The same calculations apply to the coefficients of $\mathbf{D}$. All calculated values match those found through simulation.

4.6 Web application

The code for the web application is available from the author upon request, or can be downloaded in a zip file from:
`https://drive.google.com/open?id=1Gf9ARYHm1kwVSKfZmTMuHQT25o-5qcJS`
Tutorials for running a Flask web application are available on the Flask website:
`http://flask.pocoo.org/`

4.6.1 Front-end

The web application consists of four pages, see figure 4.63.

index.html

The front page of the application, see figure 4.63a. The user can press the ”Begin” button to go to the ”pattern” page and begin the process of creating the pattern.

pattern.html

The pattern selection page of the application, see figure 4.63b. The user can select the flexure type and wallpaper group. The ”Back” button leads to the ”index” page, while the ”Next” button leads to the ”option” page. If the flexure type and wallpaper group combination is invalid (i.e. not yet added to the application), an error is raised upon pressing ”next”, prompting the user to select a valid combination.

option.html

The option selection page of the application, see figure 4.63c. Under ”Mode”, the user can select if they want the output to be a sample pattern, a full SVG, or an Abaqus script, the former two being vector graphics files. The checkboxes indicate that the user can select multiple modes; not selecting a mode raises an error prompting the user to select at least one mode. Similarly under ”Part”, the user can select if they want to output a generating region, unit cell or flexure pattern, or any combination thereof, but must select at least one. Under ”Unit”, the user must select the unit for the measurements. As Abaqus is unitless,

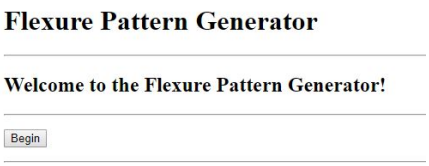

(a) The index page.

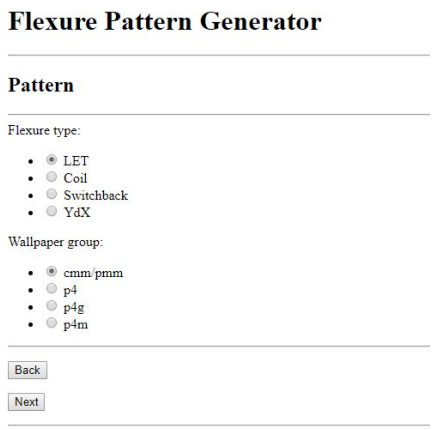

(b) The pattern page.

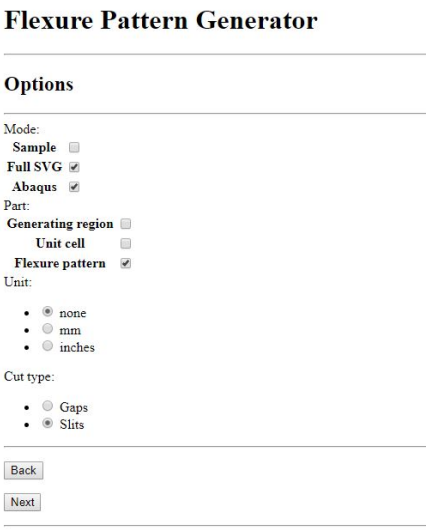

(c) The option page.

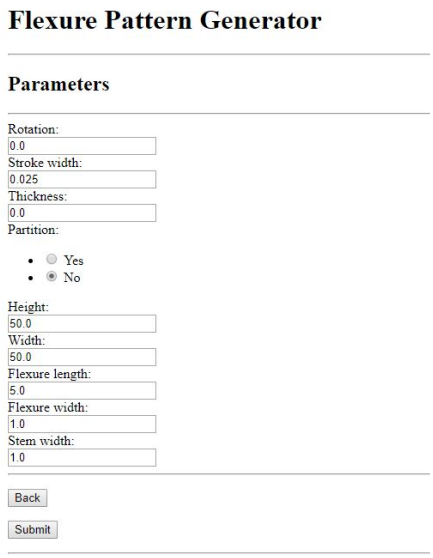

(d) The parameter page.

Figure 4.63: The pages of the web application.

this is irrelevant for the Abaqus script output; however, for the vector graphics file outputs, this selects the unit of the file. Under ”Cut”, the user must select whether they want the cuts to be gaps or slits. The ”Back” button leads to the ”pattern” page, while the ”Next” button leads to the ”parameter” page.

parameter.html

The parameter input page of the application, see figure 4.63d. This page displays the relevant parameters for the flexure pattern and output types, which the user can fill in. The fields are pre-filled with default values. Pressing the ”Back” button leads to the ”option” page. Pressing the ”Submit” button, on the other hand, sends the parameters to the flexure pattern generating program, which creates the relevant files (as specified on the ”option” page). These files are then compressed into a zip file that the user is prompted to download.

4.6.2 Back-end

The logic of the web application is kept in Python programs.

__init__.py

Initializes an instance of the web application.

forms.py

Creates forms to be rendered on the website from which parameters can be gathered. Includes validation logic for the forms.

routes.py

Contains the logic of what happens upon performing actions, including redirecting to different pages and rendering these. This is where the parameters are gathered and sent to patternGeneratorsClass.py for generating the files, after which the files sent to the user for download.

patternGeneratorsClass.py

Originally created by Østmo and expanded upon by the author, this is where the geometry of the flexure pattern and its parts is defined using parameters sent from the web application. The program then sends the geometry to makeSVG.py and makeAbaqus.py for generation of vector graphics files and Abaqus script, respectively.

makeSVG.py

Originally created by Østmo and adapted by the author, this is where the vector graphics files are generated from the part geometry.

makeAbaqus.py

This is where the Abaqus script is generated from the part geometry.

4.6.3 Discussion

In its current form, the web application is not appealing to look at. In order to attract users, CSS should be added. In addition, an explanation of each of the parameters should be added. The application also does not automatically delete files after they have been downloaded – this will cause bloating over time. Finally, more error handling should be added to detect invalid input. Otherwise, the application is fully functional, creating files as it should depending on the given parameters.

Chapter 5

Conclusion

The flexure pattern generating web application was created in the hopes of bridging the gap between theory and application. The web application provides an interface that lets the end user easily create patterns using their own parameters. This could open up new possiblities for discovering applications of flexure patterns.

Simulations were confirmed to closely match results of experiments with real life patterned plates. While further real-life testing is recommended, this brings confidence to the use of simulations for flexure patterns – as long as one is careful to take into account the nonlinear effects due to large deformations.

When creating plates with flexure patterns, the user must keep in mind that the production of the patterned plate might have an unforeseen impact on its properties in addition to the pattern itself. In using a laser cutter, a pattern with small unit cells and/or narrow flexures might not cut properly, or have its properties affected by the heat-affected zone around the cut.

The goal of the thesis was to provide tools and present information that might be useful for real-life application of flexure patterns by the end user, and the author sincerely hopes that she has accomplished this task.

Bibliography

[1] Arla Plast. Griphen, 2017. URL http://www.arlaplast.com/wp-content/uploads/2015/08/GRIPHEN.pdf.

[2] ASTM International. ASTM d638-14 standard test method for tensile properties of plastics, 2014.

[3] S. Barone, A. Paoli, A. V. Razionale, and R. Savignano. Modelling strategies for the advanced design of polymeric orthodontic aligners. In A. Fred and H. Gamboa, editors, *Biomedical Engineering Systems and Technologies*. 2017. ISBN 9783319547176.

[4] K. Bates-Green and T. Howie. Materials for laser cutter machines, 2019. URL http://www.materialseducation.org/educators/matedu-modules/docs/Laser_Cutter_Materials.pdf. Materials Education (MatEdU).

[5] K. Bell. *Finite Element Analysis*. Fagbokforlaget, 2014. ISBN 978-82-321-0268-6.

[6] William D. Callister and David G. Rethwisch. *Materials Science and Engineering*. John Wiley & Sons, Inc., 8th edition, 2011. ISBN 978-0-470-50586-1.

[7] W. S. Cleveland and S. J. Devlin. Locally weighted regression: An approach to regression analysis by local fitting. *Journal of the American Statistical Association*, 83(403), 1988. doi: 10.2307/2289282.

[8] N. E. Dowling. *Mechanical Behavior of Materials*. Pearson, 4th edition, 2013. ISBN 978-0-273-76455-7.

[9] R. B. Dupaix. Temperature and rate dependent finite strain behavior of poly(ethylene terephthalate) and poly(ethylene terephthalate)-glycol above the glass transition temperature, 2003.

[10] Epilog Laser. Fusion m2 32/40 laser system manual model 13000/14000, 2019.

[11] Filaments.directory. PETG filament for your 3D printer, 2019. URL https://www.filaments.directory/en/plastics/petg.

[12] R. C. Hibbeler. *Mechanics of Materials*. Pearson, 8th edition, 2011. ISBN 978-981-06-8509-6.

[13] MakeItFrom.com. Glycol-modified polyethylene terephthalate (PETG, PET-G), 2019. URL https://www.makeitfrom.com/material-properties/Glycol-Modified-Polyethylene-Terephthalate-PETG-PET-G.

[14] MatWeb. Overview of materials for petg copolyester, 2019. URL http://www.matweb.com/search/datasheet_print.aspx?matguid=4de1c85bb946406a86c52b688e3810d0.

[15] Douglas C. Montgomery, Elizabeth A. Peck, and G. Geoffrey Vining. *Introduction to Linear Regression Analysis*. John Wiley & Sons, Inc., 5th edition, 2012. ISBN 978-0-470-54281-1.

[16] D. Schattschneider. The plane symmetry groups: Their recognition and notation. *The American Mathematical Monthly*, 85(6), 1978. doi: 10.2307/2320063.

[17] O. A. Østmo. Elastic properties of flexure patterns, 2018.

[18] S. Timoshenko and S. Woinowsky-Krieger. *Theory of Plates and Shells*. Engineering Societies Monographs. McGraw-Hill Book Company, 2nd edition, 1959.

[19] U.S. National Library of Medicine. PubChem, 2019. URL https://pubchem.ncbi.nlm.nih.gov/.

Appendix

A Surface fitting

This section shows visualizations of results of surface fitting on data points from load case 3 on plate 2 using various surface fitting models in Matlab.

A.1 Polynomial models

Figures A.1–A.4 visualize the polynomial models. The original data points are shown as blue dots.

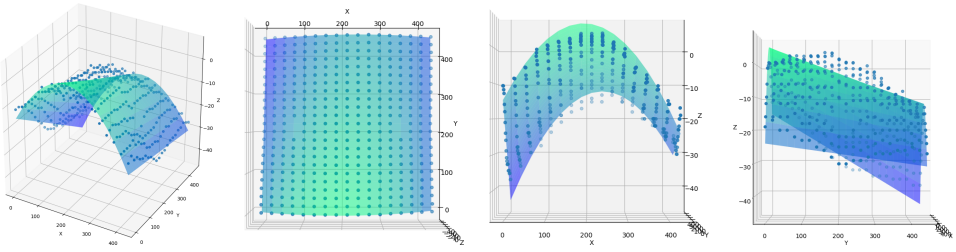

(a) Isometric view. **(b)** XY view. **(c)** XZ view. **(d)** YZ view.

Figure A.1: Load case 3 on plate 2 fitted with the 2nd degree polynomial model.

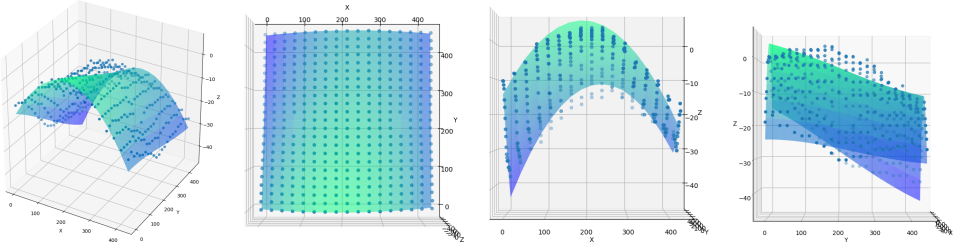

(a) Isometric view. **(b)** XY view. **(c)** XZ view. **(d)** YZ view.

Figure A.2: Load case 3 on plate 2 fitted with the 3rd degree polynomial model.

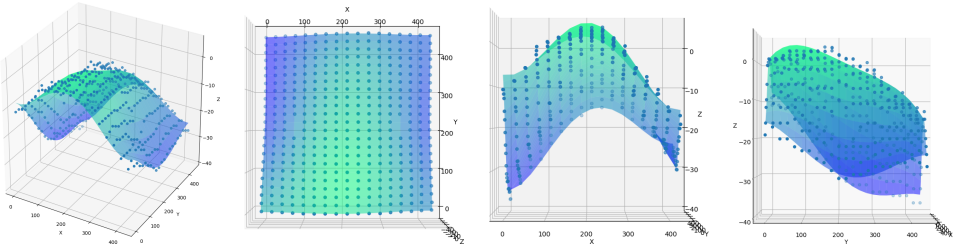

(a) Isometric view. **(b)** XY view. **(c)** XZ view. **(d)** YZ view.

Figure A.3: Load case 3 on plate 2 fitted with the 4th degree polynomial model.

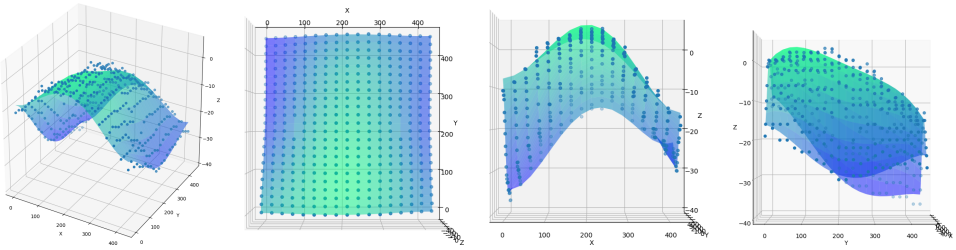

(a) Isometric view. **(b)** XY view. **(c)** XZ view. **(d)** YZ view.

Figure A.4: Load case 3 on plate 2 fitted with the 5th degree polynomial model.

A.2 Interpolant models

Figures A.5–A.9 visualize the interpolant models. The original data points are shown as blue dots.

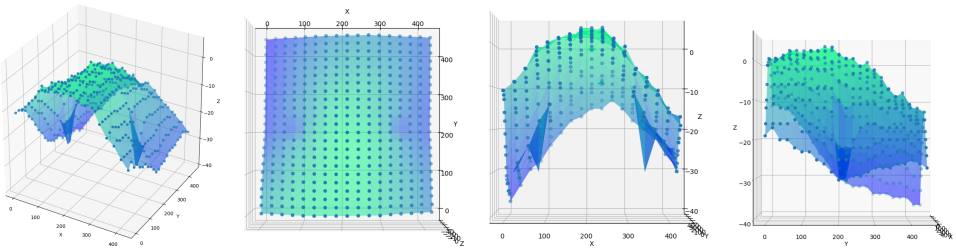

(a) Isometric view. **(b)** XY view. **(c)** XZ view. **(d)** YZ view.

Figure A.5: Load case 3 on plate 2 fitted with the linear interpolation model.

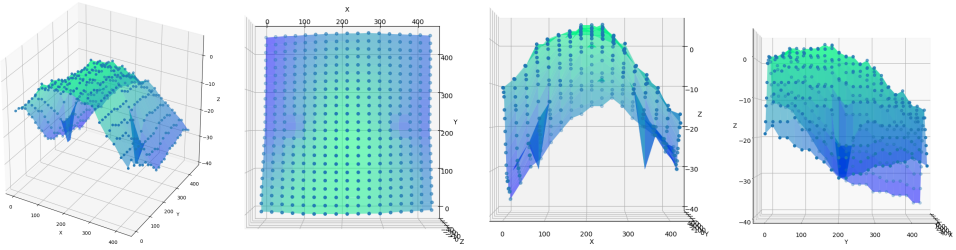

(a) Isometric view. **(b)** XY view. **(c)** XZ view. **(d)** YZ view.

Figure A.6: Load case 3 on plate 2 fitted with the nearest neighbor interpolation model.

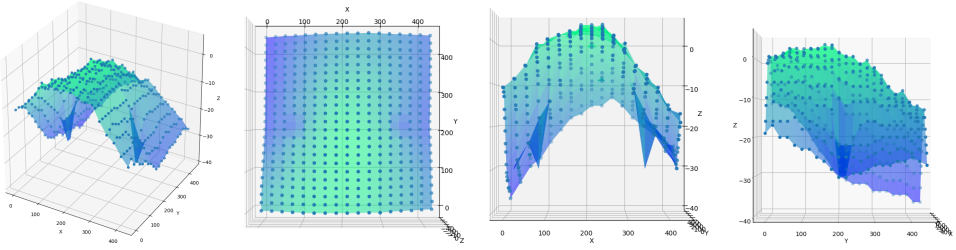

(a) Isometric view. **(b)** XY view. **(c)** XZ view. **(d)** YZ view.

Figure A.7: Load case 3 on plate 2 fitted with the cubic spline interpolation model.

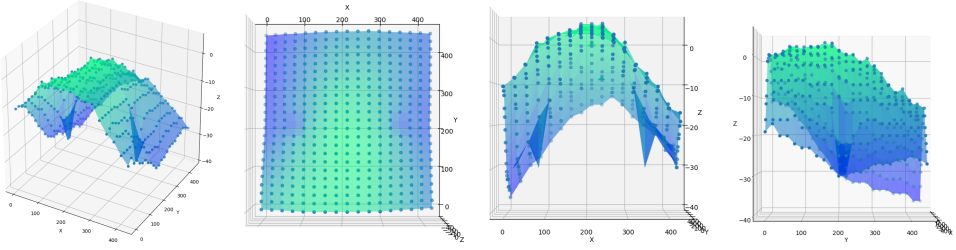

(a) Isometric view. **(b)** XY view. **(c)** XZ view. **(d)** YZ view.

Figure A.8: Load case 3 on plate 2 fitted with the biharmonic interpolation model.

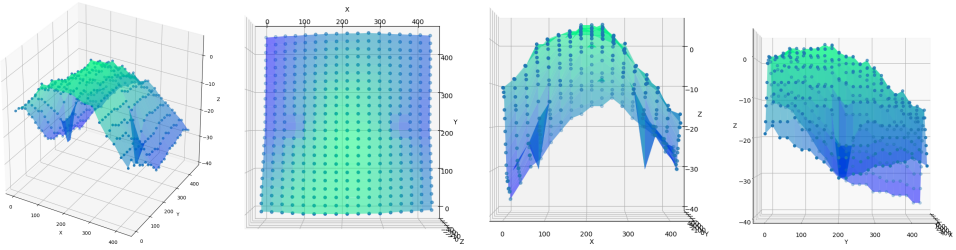

(a) Isometric view. **(b)** XY view. **(c)** XZ view. **(d)** YZ view.

Figure A.9: Load case 3 on plate 2 fitted with the thin-plate spline interpolation model.

A.3 Loess models

Figures A.10 and A.11 visualize the lowess and loess models, respectively. The original data points are shown as blue dots.

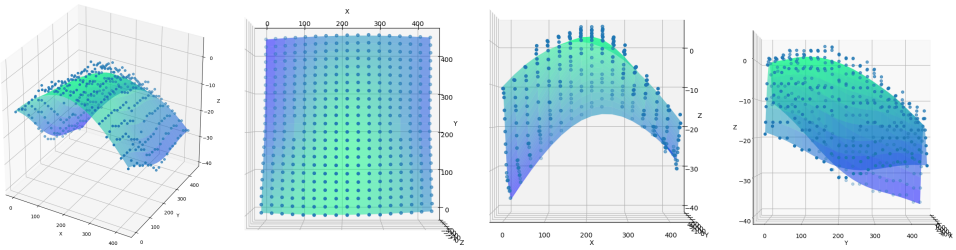

(a) Isometric view. **(b)** XY view. **(c)** XZ view. **(d)** YZ view.

Figure A.10: Load case 3 on plate 2 fitted with the local linear regression model.

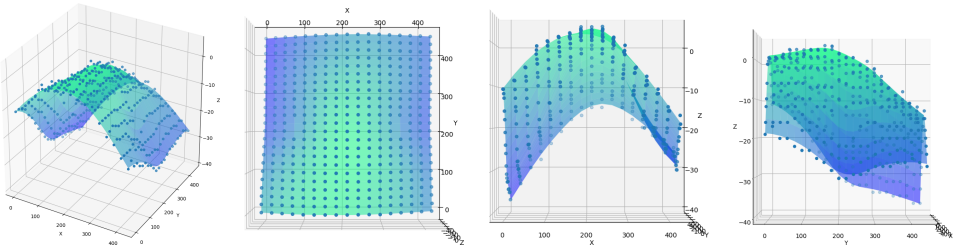

(a) Isometric view. **(b)** XY view. **(c)** XZ view. **(d)** YZ view.

Figure A.11: Load case 3 on plate 2 fitted with the local quadratic regression model.

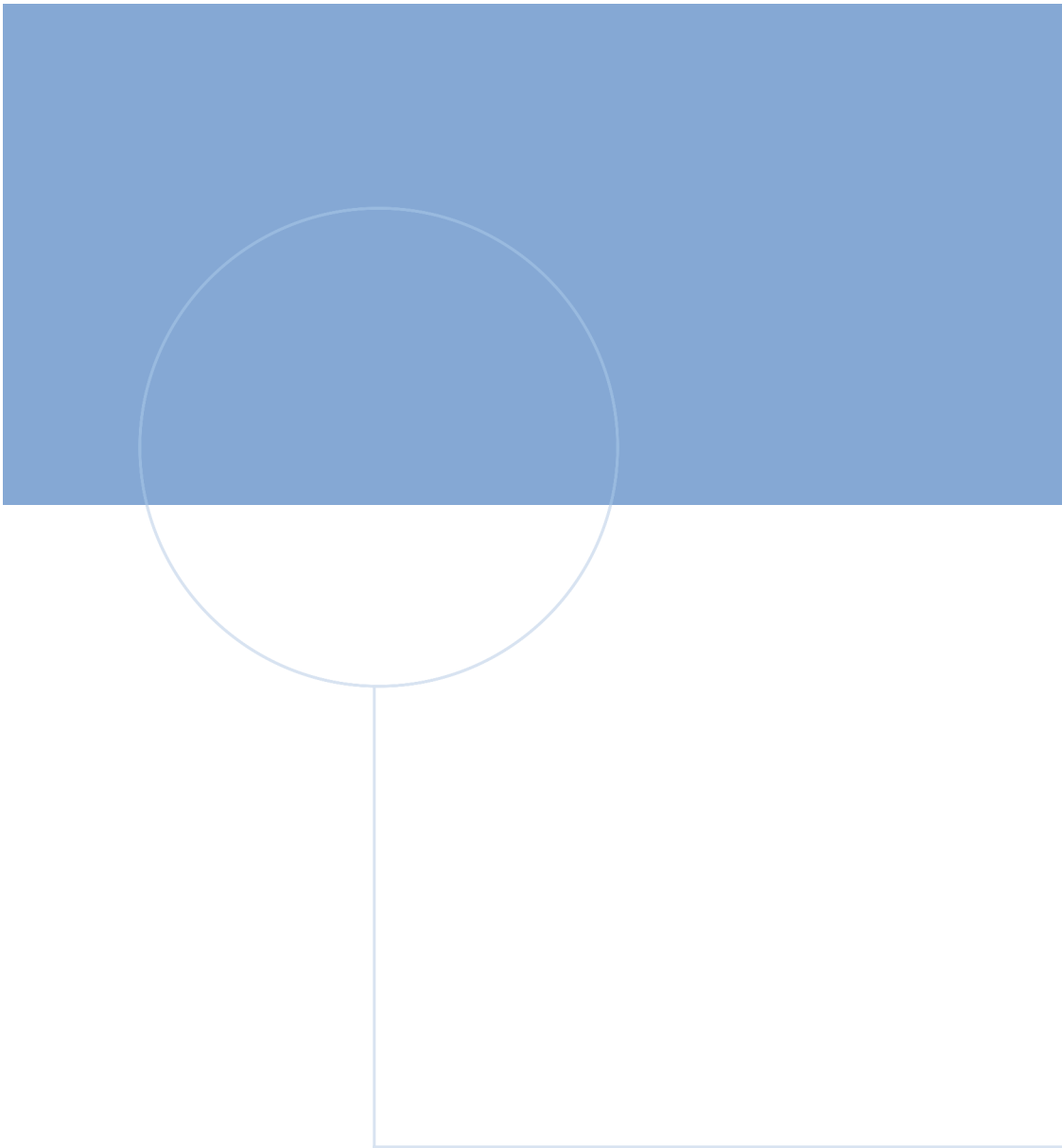

NTNU
Norwegian University of
Science and Technology